# ULTRAFAST LASER FABRICATION OF 3-D PHOTONIC COMPONENTS AND PHOTONIC TOPOLOGICAL INSULATORS

by

**Sheng Huang**

B.S. in Applied Physics, University of Science and Technology of China, 2009

M. S. in Physics, University of Pittsburgh, 2012

Submitted to the Graduate Faculty of

Swanson School of Engineering in partial fulfillment

of the requirements for the degree of

Doctor of Philosophy

University of Pittsburgh

2018

UNIVERSITY OF PITTSBURGH

SWANSON SCHOOL OF ENGINEERING

This dissertation was presented

by

Sheng Huang

It was defended on

November 30, 2018

and approved by

Kevin P. Chen, Ph.D., Professor
Department of Electrical and Computer Engineering
Zhi-Hong Mao, Ph.D., Professor
Department of Electrical and Computer Engineering
Susheng Tan, Ph.D., Associate Professor
Department of Electrical and Computer Engineering
Feng Xiong, Ph.D., Assistant Professor
Department of Electrical and Computer Engineering
Paul Ohodnicki, Ph.D.
National Energy Technology Laboratory

**ULTRAFAST LASER FABRICATION OF 3-D PHOTONIC COMPONENTS AND PHOTONIC TOPOLOGIC INSULATORS**

Sheng Huang, PhD

University of Pittsburgh, 2018

Optical waveguide interconnect has been considered as a key enabling technology to address bandwidth bottleneck limited by electrical wire at board levels. Current waveguide technology for optical interconnect were realized based on 2D waveguide technology based on layer-by-layer lithography schemes built on silicon or polymer substrates. As data rate explodes at chip and board levels, the optical routing complexity and high laser power required to support high data bandwidth demand a new waveguide interconnect topology.

In this dissertation, we study and explore ultrafast laser fabrication technology to build highly complex 3D waveguide lightwave circuits in glass substrates to support demand for high bandwidth optical interconnect. This dissertation first explores 3D waveguide structure fabrication in flexible glass substrates. Characteristics and performances of various waveguide devices inscribed in flexible glasses are compared with those built on polymer substrates. This work is then followed by development of an integrated laser manufacturing solution, using the same platform, to manufacture board-level optical interconnect waveguides and 45° total internal reflection (TIR) micromirror for vertical coupling. To expand 3D waveguide technology in optical fiber devices, 3D waveguide couplers and WDM components, two key components for fiber lasers, were directly fabricated on multi-core optical fibers, turning the silica fiber from a 1-D optical channel to a 3-D integrated system. Based on paraxial approximation, 3D coupled photonic waveguide array were designed, fabricated, and characterized to study photonic graphene under Gauge field. Results and efforts described in this dissertation demonstrated that, through the optimization of laser matter interaction, high-density 3D waveguide consists of more than 15 layer can be fabricated for a wide array of photonic applications.

## TABLE OF CONTENTS

## ABBREVIATIONS

| | |
|---|---|
| BWG | Bragg Waveguide Grating |
| MFD | Mode-Field Diameter |
| OSA | Optical spectrum analyzer |
| OFDR | Optical Frequency Domain Reflectometry |
| SMF | Single Mode Fiber |
| NA | Numerical Aperture |
| CW | Continuous Wave |
| OBR | Optical Backscatter Reflectometer |
| ND | Neutral Density |
| HWP | Half Wave Plate |
| RT | Room Temperature |

## LIST OF TABLES

## LIST OF FIGURES

## PREFACE

I am grateful for the tremendous help and financial support from Professor Kevin P. Chen. And many thanks to Dr. Ming-Jun Li, Dr. Sean M. Garner and Dr. Rechtsman for their suggestions and help.

I would also like to thank Dr. Ohodnicki from National Energy Technology Laboratory (NETL), Dr. Zhi-Hong Mao, Dr. Susheng Tan, Dr. Feng Xiong from our ECE department for serving as my PhD dissertation committees.

The projects could not have been possible without the help of Dr. Mingshan Li, Dr. Rongzhang Chen, Dr. Aidong Yan, Dr. Qingqing Wang, Dr. Botao Zhang. And I would like to express my gratitude to my colleagues in the lab for all the helpful discussions: Mohan Wang, Ran Zou, Shuo Li, Ya-Wen Huang.

Last but not least, my work could not have been possible without the love, care, support and encouragement from my family.

# 1.0 INTRODUCTION

Since the discovery of high-quality organic optical materials in the 1990s, polymer photonics has evolved into a dynamic field of engineering research and industrialization. The distinct advantages of polymer photonic devices, compared to inorganic photonic devices, are their low device/material costs and remarkable mechanical flexibility [1, 2]. These unique traits have instigated worldwide R&D efforts on polymer photonics at both device and system levels. The mechanical flexibility and low material cost of polymer photonics opens up a number of tangible possibilities for diverse photonic applications. Some prominent applications include board-level and rack-level optical interconnects [3-8], "the last mile problem" associated with Fiber-To-The-Home (FTTH) applications [9-11], all-optical data processing [12-14], integrated sensor systems [15-17], and other short-haul communication applications.

Over the last decade, a majority of R&D efforts in flexible photonics have been invested in the development of a wide range of optical polymer systems with characteristics that meet requirements in many photonic applications [18]. These material characteristics include refractive index, optical loss, birefringence, mechanical properties, and material stability [19]. While the development of high-quality polymer optical materials has achieved some successes, it still incurs relatively high optical loss especially at telecom wavelength of 1.5 μm. As data rates dramatically increase in short-haul communication systems driven by the digital revolution, the optical power required to support high data bandwidth in optical waveguides also increases significantly. The relatively poor polymer thermal stability coupled with high optical loss of polymer photonic devices pose significant limitations of polymer photonic devices for high data bandwidth applications.

Over the last several years a brand new class of flexible glass materials has been produced by major material companies for commercial electronics. By reducing the thickness of the glass substrate to less than 100 μm, remarkable mechanical flexibilities have been realized [32]. The dramatic reduction of glass thickness, resulting lower stiffness, and lower bend stress permit roll-to-roll processes to produce high-quality glass substrates on a manufacturing scale that support pervasive consumer electronics applications. In addition to electronic device applications such as displays and photovoltaics, these flexible glasses enable new opportunities for flexible optical substrates.

These flexible glass substrates possess the same superior optical, mechanical, surface, thermal, and dimensional stability properties as the conventional thicker, rigid glass materials. Thus, these new, glass-based flexible optical substrates are inherently more stable and have better optical properties than the typical polymer optical substrates. The advent of flexible glass substrates provides an alternative to designing flexible lightwave circuits besides polymeric options. This dissertation explores the opportunity of using flexible glass substrates to enable new flexible photonic applications, device designs, performance levels, and fabrication techniques. It should be noted that all glass substrates can be made flexible when their thickness is reduced since the stiffness is related to (thickness) 3. The glass substrates used in this dissertation are an alkali-free borosilicate glass that is compatible with both flexible photonic as well as flexible electronic applications. It is known that high-quality waveguides can be produced in this glass family using the ultrafast laser direct writing process [36, 37].

In section 1 to section 3 of this dissertation, we report on the fabrication of waveguides in flexible glass substrates using the ultrafast laser direct writing technique [21]. Single-mode waveguides at 1550 nm with propagation loss as low as 0.11 dB/cm have been successfully produced in flexible glass with thickness of 25 µm, 35 µm, 50 µm, and 100 µm. Waveguide bend losses and thermal stability of fabricated waveguides and waveguide grating devices were also studied in this dissertation. In section 4 of this dissertation, we go beyond a single waveguide device in order to fabricate complex photonic structures using the enhanced laser writing platform.

# 2.0 FLEXIBLE GUIDED-WAVE PHOTONICS

Since the discovery of high-quality organic optical materials in 1990s, guided-wave polymer photonics has evolved into a dynamic field of engineering research and industrialization. The distinct advantages of polymer optical waveguide devices and circuits, compared to inorganic guided-wave photonic devices, are their low material costs and remarkable mechanic flexibility. These unique traits have instigated worldwide research and development efforts on polymer photonics at both device and system levels.

When guided-wave photonic devices are fabricated on flexible material substrates, these devices manage to maintain their optical performance under mechanical deformations such as bending, stretching, compression, etc. Such mechanical flexibility has enabled a diverse range of photonic functionalities. Some prominent applications include optical interconnects at board levels and rack levels, “the last mile problem” associated with Fiber-to-the-home (FTTH) applications, all-optical data processing, integrated sensor systems, and other short-haul communications applications.

Over the last two decades, flexible photonic circuits, by default, have been built using polymer materials or on polymer substrates. The advancement of flexible glass materials, however, have the potential to transform the landscape of the flexible waveguide photonic technology. In this section, we discuss potentials of flexible photonics based on flexible glass materials. To put these discussions in perspective, this section first reviews current state-of-the-art flexible photonic technology based on polymer materials. This is followed by brief review of optical and mechanical properties of flexible glass and their implications for photonic applications. Based on these background discussions, this section describes our recent efforts on the fabrication of photonic devices in flexible glass using ultrafast laser direct writing techniques. Characteristics and performance of various waveguide devices inscribed in flexible glass are compared with those built on polymer substrates.

## 2.1 FLEXIBLE POLYMER PASSIVE WAVEGUIDE PHOTONICE

The flourish of flexible guided-wave photonic devices started from the discovery of high-quality optical polymer materials in 1990s [1-7]. Since then, a significant portion of research and development efforts in flexible photonics have been invested. Topics include a wide range of optical polymer systems with characteristics that meet application requirements in photonics. These material characteristics include refractive index, optical loss, birefringence, mechanical properties, and thermal stability. These efforts have yielded a large number of optical polymer systems with excellent optical properties optimized for guided-wave applications.

One of the most important developments of polymer photonics in the last decade is the development of polymer waveguides with exceptionally low optical propagation losses below 0.05 dB/cm [8-10] for near infra-red (NIR) wavelength around 800 nm. Hence, polymer waveguides have become excellent candidates as optical links for board-level interconnects. Most of the polymer optical waveguides have been fabricated using conventional lithography-based methods. Direct photo-patterning, micro-molding, and imprint/embossing have also been used to produce polymer waveguides. This versatility in device fabrication is another advantage of polymer photonics. Table 1 summarizes some current state-of-the-art polymer optical materials and processing techniques used for polymer waveguide development and waveguide performance at various wavelengths.

**Table 1:** Key Properties of Optical Polymers for Waveguide Fabrications [6]

| Manufacturer | Polymer Type | Patterning Techniques | Loss, dB/cm [ λ, nm] | Birefringence [λ, nm] |
|---|---|---|---|---|
| Allied Signal | Acrylate | Photo exposure / wet etch, RIE, laser ablation | 0.02 [840]<br>0.2 [1300]<br>0.5 [1550] | $<2.0\times10^{-4}$[1550] |
| | Halogenated Acrylate | Photo Exposure / wet etch, RIE, laser ablation | <0.01 [840]<br>0.3 [1300]<br>0.7 [1550] | $<10^{6}$ [1550] |
| Amoco | Fluorinated Polyimide | Photo exposure / wet etch | 0.4 [1300]<br>1.0 [1550] | 0.025 |
| Dow Chemical | Benzocyclobutene | RIE | 0.4 [1300]<br>1.0 [1550] | |
| | Pefluorocyclobutene | Photo Exposure / wet etch | 0.25 [1300]<br>0.25 [1550] | |
| DuPont | Acrylate | Photolocking | 0.18 [800]<br>0.2 [1300]<br>0.6 [1550] | |
| General Electric | Polyetherimide | RIE, laser ablation | 0.24 [830] | |
| Hoechst Celanese | PMMA copolymer | Photobleaching | 1.0 [1300] | |
| JDSU Photonics | [BeamBox™] | RIE | 0.6 [1550] | |
| NTT | Halogenated Acrylate | RIE | 0.02 [830]<br>0.07 [1310]<br>1.7 [1550] | $5.0\times10^{-6}$ [1310] |
| | Deuterated Polysiloxane | RIE | 0.17 [1310]<br>0.43 [1550] | |
| | Fluorinated Polyimide | RIE | TE:0.3<br>TM: 0.7 [1310] | |

Today, signals on a printed circuit board are routed using copper wires. As these electrical interconnects approach their physical limits on data rate and power dissipation, the advent of low-loss polymer waveguide technology provides a feasible optical solution for high-speed interconnects at the board level. Polymer waveguide interconnect technology provides a number of advantages over those of copper wires including high bandwidth, low power consumption, and free of electromagnetic interference. Given that the bandwidth of optical waveguides is far higher than that of electric interconnect, the design (e.g. size, shape, length) and implementation (e.g. connectors) of optical interconnects is independent from signal channel data rate.

Using either UV laser lithography or direct UV laser writing technique, multi-layer polymer waveguide arrays have been successfully fabricated on PCB boards with exceptionally low loss (<0.05 dB/cm [9]). A common polymer waveguide fabrication process developed by IBM [9] is illustrated in Figure 2.1.1. It typically involves four steps including: (1) the deposition and UV curing of the photosensitive lower cladding layer; (2) the deposition of the photosensitive core polymer layers; (3) the waveguides could be defined by either a UV laser direct writing (photo-polymerization) or UV laser lithography and wet etching process; and (4) deposition and UV curing of the upper cladding.

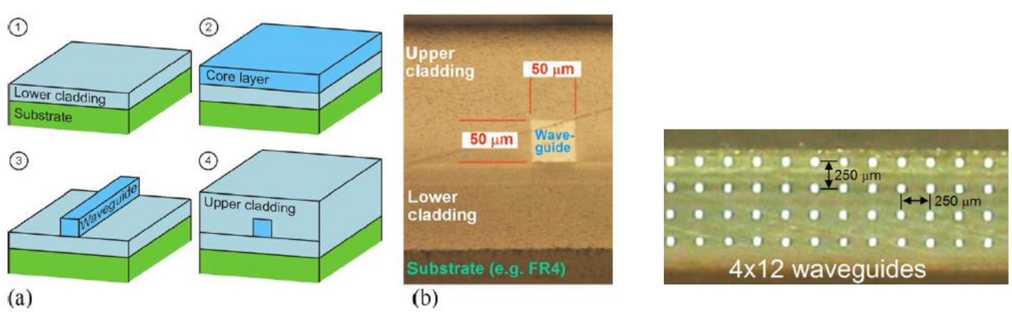


**Figure 2.1.1:** (a) Schematic of a polymer waveguide fabrication process, (b) Microscopic cross-section view of a 50×50 μm2 waveguide, and (c) a 4×12 waveguide array [9]

Repeating the waveguide fabrication process mentioned above, it is also possible to produce multi-layer waveguide structures. An example of a 4×12 waveguide array with pitch of 250-μm is shown in Figure 2.1.1(c). These waveguide devices were developed by IBM [9]. The waveguide cross-section is 50×50 $\mu m^2$. Based on the low-loss polymer waveguide technology, various optical building blocks needed for board-level optical interconnects have been developed. Figure 2.1.2 shows the schematic and photograph of a 12 channels board-to-board optical interconnect link using polymer waveguides as on-board channels for 10 Gb/s per channel data rate transmission.

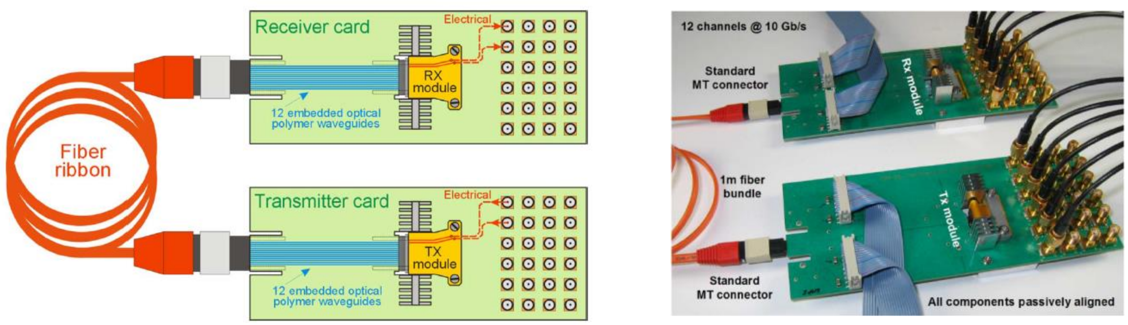


**Figure 2.1.2:** Schematic of a 10-channel board-to-board optical link developed by IBM, and photograph [9]

Despite significant successes of the low-loss polymer waveguide development over the last decade, challenges remain. Waveguides built entirely using polymer materials have relatively low refractive index contrast $\Delta n$ between the waveguide core $n_1$ and cladding $n_2$ (i.e. $\Delta n$=$n_2$-$n_1$). A large index contrast is necessary for strong optical confinements and tight bending radius.

To address this challenge, a hybrid approach has been studied to develop high refractive index contrast waveguides by deposited very thin (< 3 μm) inorganic optical materials on flexible polymer substrates. Using a transfer printing approach [10-11], high-quality crystalline silicon waveguides fabricated on very thin silicon substrates can be integrated on flexible polymer substrates. However, multiple pattern transfer steps are required to accomplish this work.

An alternative approach is direct material deposition and patterning on the flexible substrates. Recently, amorphous silicon and silicon nitride have been directly deposited on polymer substrates using a chemical vapor deposition technique [12-15]. However, the low melting point of polymer materials severely limit the deposition temperatures. This compromises optical quality of waveguides deposited and fabricated on polymer substrates.

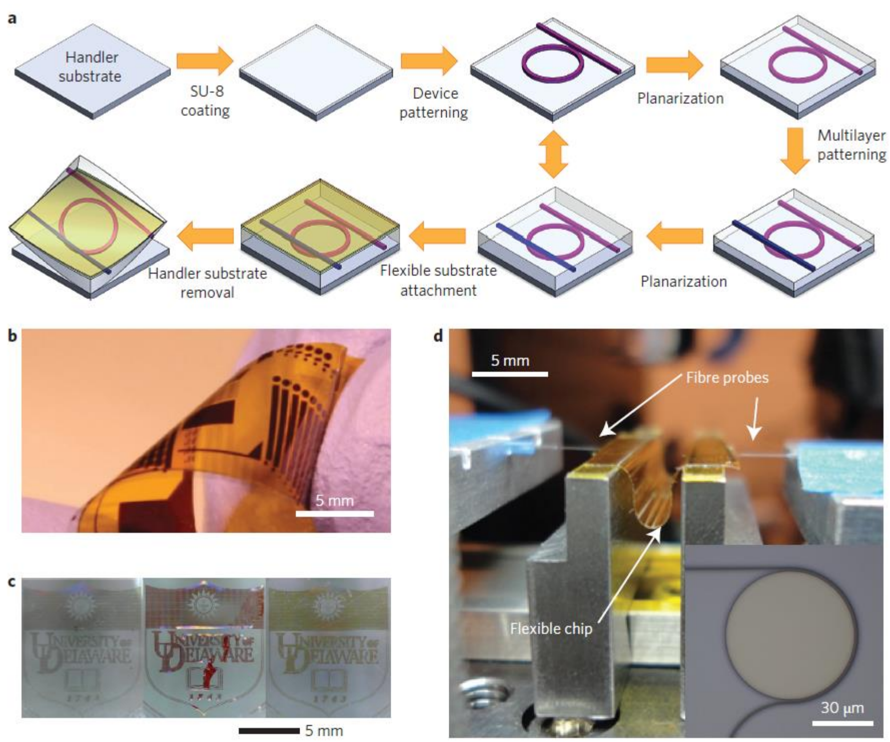


**Figure 2.1.3:** (a) Schematic view of flexible waveguide fabrication process, (b) photograph of waveguide after the handler substrate removal, (c) example of ChG glass with different composition, and (d) flexible waveguide bending test (after [12]).

A relatively successful work of direct material deposition and patterning for waveguide fabrication on polymer substrates was achieved using high index chalcogenide glass (ChG) materials as shown in Figure 2.1.3 [12]. This work takes advantages of high-refractive-index chalcogenide glass materials that are deposited at relatively low temperatures. The large glass composition selection of ChG materials also provides wide tunability of refractive index (*n*~ 2 to 3). The fabrication process is schematically illustrated in Figure 2.1.3. The process begins with a spin-coating of SU-8 epoxy on an oxide coated Si wafer. This is followed by ChG material deposition using a sputter coating process at low temperatures. Using UV contact lithography, optical waveguide circuits can be fabricated on the top of the SU-8. Another layer of SU-8 was used to cover the ChG waveguide devices and to serve as waveguide cladding. After the UV cross-linking and planarization of the SU-8, this fabrication process can be repeated to produce multi-layer waveguide structures. Finally, the flexible structures (ChG waveguides embedded in SU-8) were delaminated from the rigid Si wafers to complete the fabrication process. Using high refractive index ChG glass, waveguide structures with a bending radius as small as 30-μm can be readily produced by this approach.

Although the hybrid approach shown in Figure 2.1.3 increases the device design for flexible waveguide photonics, ChG materials produced by the low-temperature sputtering process nevertheless incur high losses of 1.6 dB/cm. This is much higher than those fabricated in pure polymer waveguides presented in Figure 2.1.1.

## 2.2 FLEXIBLE POLYMER ACTIVE WAVEGUIDE PHOTONICS

One of the unique traits for polymer optical materials is their capability for doping. This makes polymer materials an interesting alternative to inorganic substrates in applications of active waveguide lasers and amplifiers. A number of research works have been working to develop polymer optical materials with optical gains from ultraviolet to near infrared wavelength ranges. The realization of high-quality active polymer materials with optical gains are inherently challenging, especially at λ=1.5μm, for their potential applications in optical communications. This is due to the absorption from the C-H bonds from polymer matrix [16]. However, several activities have shown that it is possible to achieve significant optical gain via optimization in material compositions and waveguide fabrication. At present, most of the active polymer waveguide efforts attempt to dope or modify well-studied optical polymer materials such as SU-8 or PMMA. Two approaches have been used to incorporate active species into optical polymers to achieved significant gain.

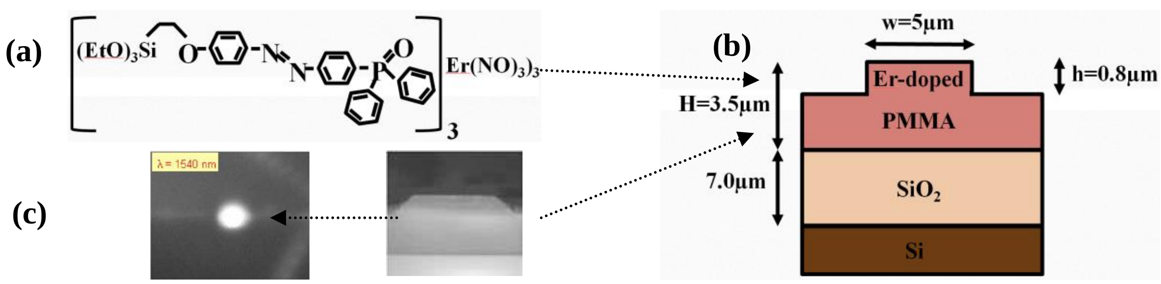


**Figure 2.2.1:** (a) chemical structure of QB-Er complex ligand, (b) schematic sketch of PMMA active waveguide structures. The SEM photograph and guided mode profile at 1540 nm is shown in (c).

The first approach is to attach rare-earth atoms such as erbium (Er) to organic ligands. For example, an erbium complex ligand, trisnitrato-tris-[4-(2-triethoxysily-propoxy)-phenylazo-oxide]-phenyl-diphenyl-phosphin] erbium (III) (QB-Er) (Figure 2.2.1(a)), has been incorporated into PMMA. Incorporation of Er-containing polymer ligand into a polymer host (e.g. PMMA) can result in a few percent of Er concentration by weight. This leads to significant optical gain. Using spin coating, Er-complex-doped PMMA was coated onto thermally oxidized silicon wafers. The 7μm thick oxide layer serves as a lower cladding layer. Using a standard photolithography and etching process, a ridge optical waveguide was formed as a single-mode optical amplifier. The polymer optical waveguide amplifier demonstrated in Figure 2.2.1 [16] reports 1.35 dB/cm loss and a net gain (gain-loss) of 0.9 dB/cm under 90-mW optical pumping at $\lambda$=980nm.

To further improve the optical gain of polymer optical materials, rare-earth doped nano-crystals have been incorporated into the polymer hosts. It is known that $NaYF_4$ is one of the most efficient nano-crystalline hosts for $Er^{3+}$ ions. Through $Yb^{3+}$ and $Ce^{3+}$ co-doping, emission efficiency of $Er^{3+}$-$NaYF_4$ nano-crystal can be optimized through the suppression of the up-conversion process.The uniform dispersion of nanocrystals in PMMA or SU8 matrix can be achieved by coating nanocrystal $NaYF_4$:$Er^{3+}$, $Yb^{3+}$, $Ce^{3+}$ oleic acid. Zhao *et. al* [17] has development polymer optical waveguide amplifiers by dissolving both SU8 and nanocrystals in toluene. The solution was then spin-coated on thermally oxidized silicon wafer similar to those used in Figure 2.2.1.

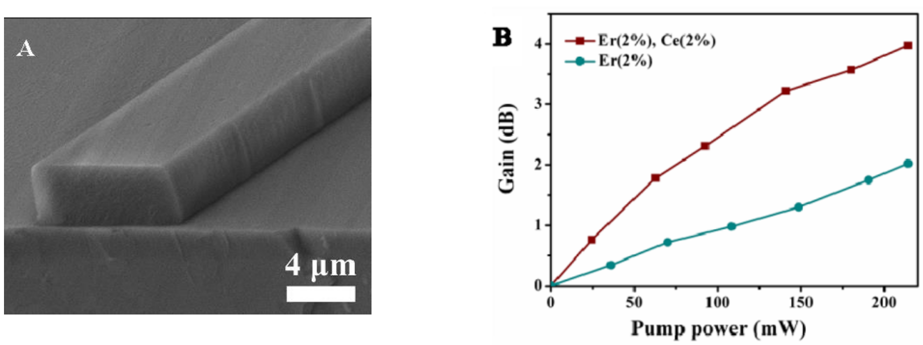


**Figure 2.2.2:** (a) SEM photograph of polymer waveguides (SU8+ nanocrystals) on the top of oxidized silicon wafers, (b) the gain of polymer waveguide with different $Er^3$+ and $Ce^{3+}$ concentration.

Figure 2.2.2(a) shows an SEM image of the SU-8 polymer waveguide on top of an oxidized silicon wafer. The dimension of single-mode polymer waveguide is 4×8 $\mu m^2$. Pumped by a 980-nm diode laser, the gain spectra of the 1.3cm long active waveguides with different Er- and Ce-ion concentrations is shown in Figure 2.2.2(b). With Ce-dopant in nano-crystals, a maximized gain of 3.08 dB/cm has been achieved. This is very close to the gain of state-of-the-art of Er-doped glass waveguides (4-5 dB/cm).

In addition to the development of active polymer materials and waveguides, optical amplifier and laser technology could also benefit by exploiting the flexible optomechanical properties of polymer waveguide devices. Extreme broadband photonic tuning is possible using polymer waveguide devices where the wavelength tuning rage far exceeds what can possibly be achieved using conventional electro-optic or thermo-optic tuning. Flexible Bragg reflectors on highly elastic polymer are usually incorporated into a superluminescent laser diode (SLD) in order to demonstrate a widely tunable compact laser [15]. Both compressive and tensile strains can be applied so as to accomplish the continuous tuning of the Bragg reflection wavelength over a range of up to 100 nm. In addition, wavelength tuning from a polymer-based laser could also be achieved through thermo-optic effects. With a polymeric Bragg reflector as optical feedback, and a semiconductor optical amplifier [5] and SLD [6] to provide optical gain, the external-cavity laser is tunable through the thermo-optic (TO) refractive index tuning of polymer waveguide Bragg reflectors. The polymer material could be engineered to have superior TO efficiency and substantially change the refractive index. This enables direct tuning of the Bragg reflection wavelength over a wide range up to 30 nm.

## 2.3 FLEXIBLE POLYMER WAVEGUIDES FOR ELECTRO-OPTIC APPLICATIONS

Another major development of flexible polymer waveguide technology is electro-optic (EO) waveguide modulators enabled by polymer optical materials with very high EO tensor element

$d_{33}$. Compared with inorganic EO materials such as $LiNbO_3$, polymers offer advantages such as large bandwidth, ease of processing, and relatively low cost.

Similar to rare-earth ions or nanocrystal doping schemes for waveguide polymer optical amplifiers or lasers discussed in the previous section, EO polymer waveguides are normally made with a classic mixture of a guest nonlinear optical polymer and host polymer. A very successful polymer system is shown in Figure 2.3.1 [11]. This was prepared by mixing the EO polymer chromophore AJC146 (30% by weight), the crosslinker bismaleimide (BMI), and the host PMMA in distilled 1, 1, 2-trichloroethane (8 wt%). The EO polymers can be spin-coated on a rigid surface such as indium tin oxide (ITO) coated silicon wafers. The film was then coated, poled, and cross-linked at elevated temperatures (e.g. 135$^{o}$C). Using this approach, optical polymers with the EO coefficient as high as $d_{33}$= 220 pm/V at 1310 nm can be achieved. This is significantly higher than the EO coefficient of $LiNbO_3$ ($d_{33}$= 34 pm/V).

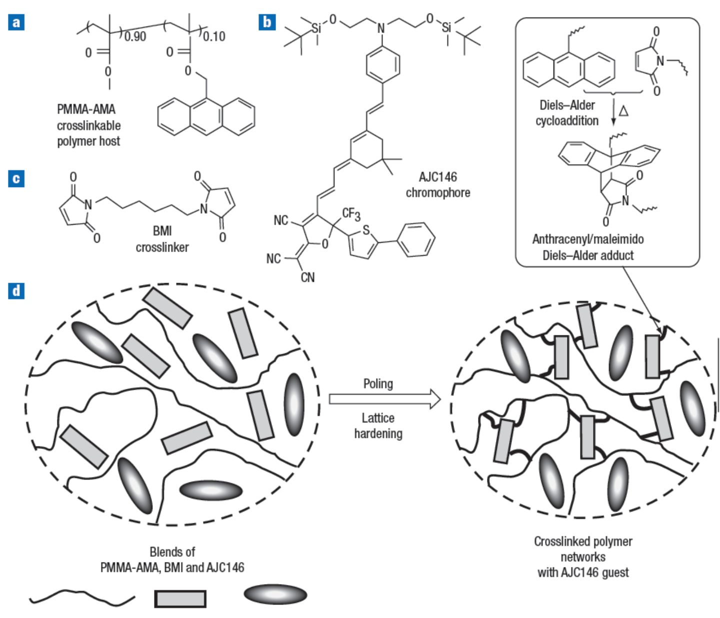


**Figure 2.3.1:** Chemical structures of EO polymer mixtures including (a) PMMA host, (b) AJC146 chromophore, and (c) BMI cross-linker. (d) schematic illustration of blends of three chemicals before and after thermal poling and lattice hardening [11].

Combining strong optical confinement abilities of silicon with superior EO modulation efficiency of polymers, photonic devices based on silicon/EO polymer hybrid material system could enable ultra-efficient EO modulation. This hybrid approach requires no polymer cladding layers, and it should lead to higher poling efficiency and lower driving voltage with fabrication simplicity. Additionally, for nanometer scale silicon slot waveguides infiltrated with EO polymers, the poling process could be minimized to further improve the poling efficiency and realize an effective in-device $d_{33}$ of 735 pm/V.

## 2.4 FLEXIBLE GLASS OPTICAL SUBSTRATE

The previous sections provided an overview of flexible waveguide technology based on polymer materials. Based on these discussions, it is quite clear that flexible photonics currently are largely polymer material engineering problems. While the development of high-quality polymer optical materials have achieved some successes, they still incur relatively high optical loss at a telecom wavelength of $\lambda$=1.5μm. In addition, polymer photonic technology is also met with challenges associated with fundamental limitations of polymer optical materials: poor material stability, environmental durability, and short lifetime span.

As data rates explode in short-haul communication systems driven by the digital revolution, the optical power required to support high data bandwidth in optical waveguides also increases dramatically. The poor polymer stability coupled with high loss of polymer photonic devices pose severe threats to the practical use of polymer photonic devices for high data bandwidth applications. For example, the highest stable temperature for two commonly used polymer optical materials, silsesquioxane and SU-8, measured at 5% wt loss during the heating, are 244$^{o}$C and 315°C, respectively. The prolonged use of polymer waveguides under intense optical field or in hostile environments might significantly reduce life-span of devices. As polymer scientists are working hard to address these fundamental material challenges, it is worthwhile to think transformative outside the box. Does mechanical flexibility and low-cost only mean plastic materials?

The answer is not necessarily. In solid mechanics, the material stiffness is related to the Young's Module ***E*** and the thickness $t$ of the object to the cube (i.e. $\textit{Stiffness} \propto E \times t^3$) [20]. Figure 2.4.1 shows the stiffness vs. thickness for polymer (polyimide), silica glass, and aluminum. Although the Young's module for polymer materials is much smaller than those of glass and metal materials, the substrate stiffness for glass and metal can be reduced significantly for thin substrates. Indeed, flexible aluminum foils (thickness 5-50μm) have been widely used since early 1970s.

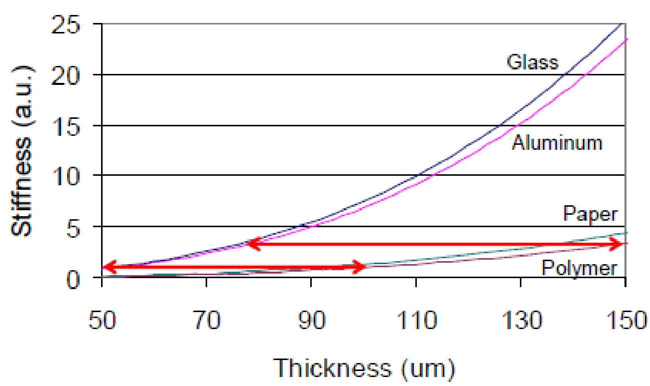


**Figure 2.4.1:** Material stiffness vs. thickness [20].

Since 2011 a brand new class of **flexible glass materials** has been produced by major material companies for commercial electronics. A famous example is Willow glass made by Corning Inc. (Figure 2.4.2(a)). By reducing thickness of glass to be <100 μm, remarkable mechanic flexibilities have been realized in glasses [20-24]. The dramatic reduction of glass thickness permits a roll-to-roll process (Figure 2.4.2(b)) to produce high-quality glass sheets in huge quantities to support pervasive consumer electronics applications. This low-cost manufacturing scheme and industrial-scale production yields another type of flexible and low-cost optical substrates. These flexible glass sheets possess the same superior optical and mechanic properties as those "conventional" inflexible glass materials with large thickness. Thus, these new, glass-based flexible optical substrates are inherently more stable and have better optical properties than those of polymer optical substrates.

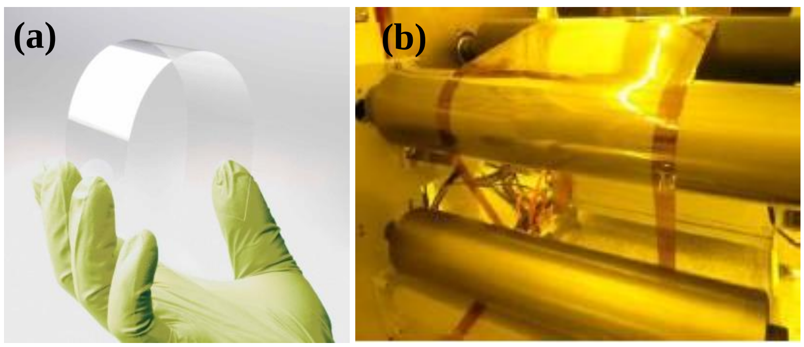


**Figure 2.4.2:** (a) Flexible glass from Corning Inc. (after [20]) and (b) Roll-to-roll glass manufacturing.

The mechanical, optical, and electrical properties achieved make flexible glass well suited for flexible photonic applications. Now the question becomes can we manufacture high-quality photonic devices with flexible glass and achieve similar or better performance than those with polymer substrates? This could be a paradigm shift for opportunities in flexible photonics. It turns long-standing material engineering challenges into a manufacturing innovations. This section explores this transformative topic. Before we describe the fabrication technology and performance of flexible waveguide devices, let's first review some key optical characteristics of flexible glass substrates.

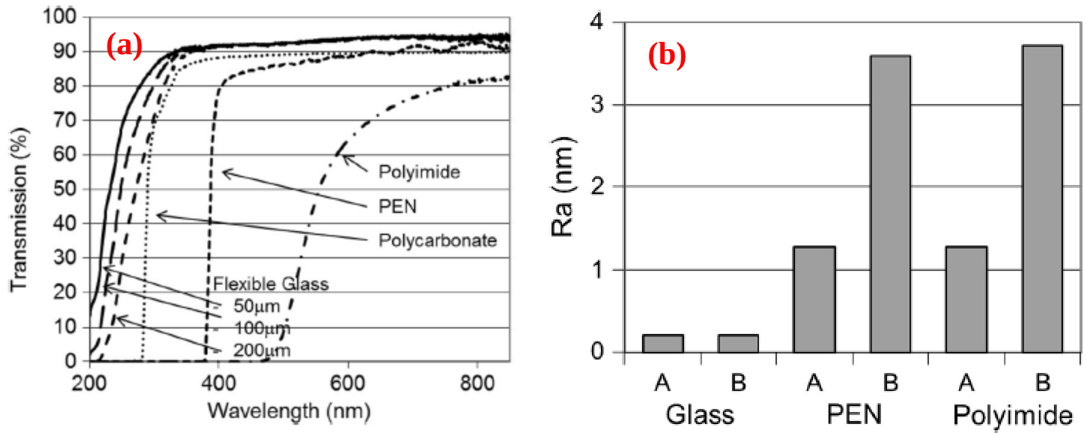


**Figure 2.4.3:** (a) Optical transmission of flexible glass and other polymeric materials [20] and (b) Surface roughness of flexible glass, PEN, and Polyimide.

In general glass enables improved performance and efficiency of opto-electronic devices. Flexible glass substrates possess interesting mechanical, electrical, and optical properties that could be utilized for flexible waveguide technology. For example, surface roughness of flexible glasses are usually below 1 nm on both glass surfaces, while polymeric materials usually have worse surface quality on the bottom surface (Figure 2.4.3(b)); flexible glass also show excellent barrier properties with a water vapor transmission rate (WVTR) beyond the detection limit of state-of-the-art measurement systems; and the thermal stability and dimensional stability of flexible glass enables high resolution devices [16-20].

The superior optical transmission and surface qualities of flexible glass compared to polymer optical materials suggest that it is possible to build optical waveguides with very low loss. This is due to lower material absorption and surface scattering losses. Being silica-based materials, flexible glasses are thermally stable, which enable them to handle high optical fields for high data rate applications. Flexible glass technology could also leverage rare-earth doped optical fibers and glass waveguide fabrication technology. This could enable flexible active waveguide and laser device developments. However, unlike many polymer composites, amorphous silica glasses are poor candidates for nonlinear optical devices such as electro-optical switches. This is due to their inversion symmetry. Silica glasses do not exhibit intrinsic second-order nonlinearity. To break the inversion symmetry in silica glass, a number of poling techniques can be implemented. In following sections, we will explore flexible waveguide technology based on flexible glass substrates using the ultrafast laser direct writing technology as an example. Other methods such as ion exchange and photolithographic patterning are also possible but not discussed here.

## 3.0 ULTRAFAST-LASER FABRICATION OF EMBEDDED WAVEGUIDES

Unlike micro-electronic circuits that rely mostly on silicon, photonic applications involve a great variety of materials including various glasses (e.g. silica, chalcogenide, ZBLAN), crystalline materials ($LiNbO_3$, YAG, diamond, ZnSe, and etc), and polymers. The development of waveguide circuits in each of the substrate materials presents distinct processing challenges.

Similar to Si microelectronics, layer-by-layer lithography approaches have been used to produce multi-layer lightwave circuits as described in the previous section of this dissertation. It involves repeated processes of thin film evaporation, photolithography, and etching.

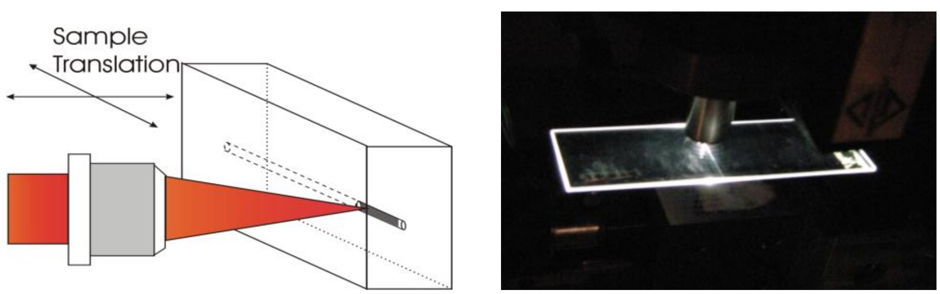


**Figure 3.0.1:** Schematic sketch and photograph of ultrafast laser direct writing technique.

However, unlike Si, the repeated deposition of many high-quality optical thin films with complex compositions are far from trivial, if not impossible. The poor film qualities are further compounded by high post-fabrication surface roughness. This severely limits performances of 3-D photonic circuits due to their poor optical characteristics. This problem exists for polymer optical waveguides.

The aforementioned material and processing challenges have motivated researchers to seek alternatives to building 3-D photonic circuits beyond the layer-by-layer approach. One of these efforts has led to the development of ultrafast laser direct writing techniques.

First demonstrated by Davis *et al.* in fused silica [21], femtosecond (fs)-lasers have been shown to be effective tools to induce refractive index changes in a wide variety of transparent materials for 3-D waveguide fabrication [22-29]. This is a simply technique where the ultrafast laser is tightly focused inside a transparent material (Figure 3.0.1). Localized index changes can be formed around the focal volume through multi-photon processes. 3-D lightwave circuits can thus be written by translating the samples along desired routes.

Since its inception, it has been widely recognized that the ultrafast laser fabrication technology *has potential* to become a game changer for 3-D lightwave circuit fabrication. It enables a simple and cross-platform laser manufacturing technique to build 3-D waveguides in a wide array of optical substrates. The advantages include:

- **No thin-film deposition:** The ultrafast laser writing technique can completely remove challenges associated with thin-film based device processing by directly fabricating lightwave circuits in bulk optical substrates with *proven optical qualities*. **This is an intrinsic advantage for flexible photonics using flexible glass materials over the polymer materials**.

- **Cross-Platform Processing Scheme:** The universal photosensitivity responses enable fabrication of 3-D photonic circuits in a wide array of optical substrates in both glasses and crystalline optical substrates.
- **True 3-D architecture:** The ultrafast laser direct writing can easily produce optical circuits at various depths below substrate surfaces, which will drastically increase device densities and routing flexibilities.

As promising as it presents, however, the transition from elegant designs to useful devices for photonic applications is far from trivial. **The success of the ultrafast laser fabrication technique really depends on the device quality and the fabrication control**. The devices traditionally produced by the ultrafast lasers are plagued by high optical loss, highly unsymmetrical guided mode profiles, and high birefringence. Figure 3.0.2 shows ultrafast laser written waveguides in optical substrates which highlight these challenges. These either only produce weak guiding (Figure 3.0.2(a) in sapphire), or highly un-symmetric guided structures (e.g. Figure 3.0.2(b) in $LiTaO_3$, Figure 3.0.2(c) in chalcogenide glasses).

Over the years, laser fabrication researchers have attempted to optimize and to perfect the “processing window” in hope of yielding better results. These approaches typically involve tuning of several processing parameters including laser repetition rate, wavelength, writing speed, and pulse energy of the processing laser. In many situations, however, tuning of these parameters is not sufficient to produce high-quality optical devices.

This is largely due to the inherent optical nonlinearity at high laser intensity and/or the anisotropic nature of optical materials. The propagation of intense laser pulses is determined by interplays between strong optical nonlinearity and laser-plasma interactions such as self-focusing, beam filamentation, and pre-focal depletion [30-33]. These coupled physical processes, which occur at *fs-ps* time scales, distort ultrafast laser pulse propagation and laser energy distribution around the focal volume. This together with subsequent thermal relaxation will lead to over-size, highly asymmetric features, and weak index changes ($\Delta n$).

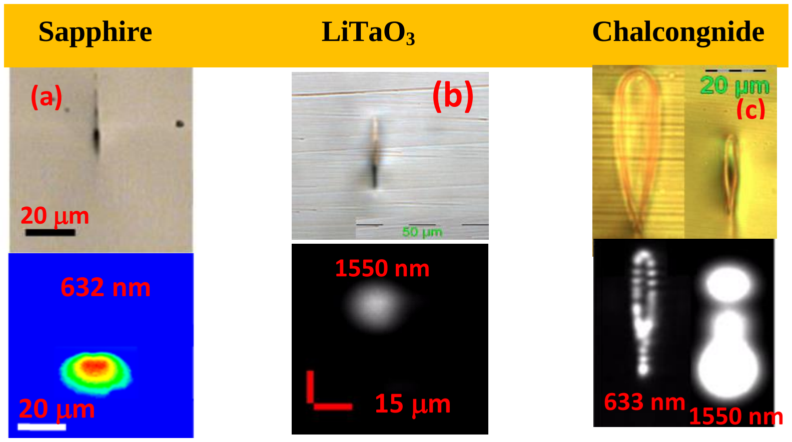


**Figure 3.0.2:** Microscope cross-section and near-field guided mode images of optical waveguides fabricated by the ultrafast laser in (a) sapphire, (b) $LiTaO_3$, and (c) Chalcogenide glass (Gallium Lanthanum Sulphide).

## 3.1 EMBEDDED WAVEGUIDES IN FLEXIBLE GLASS

As mentioned previously, flexible glass can be an effective media useful for laser and active photonic devices. This is enabled by the long history of active glass material developments using rare-earth dopants (i.e. Er, Yr, Tm, Pm-, and etc).

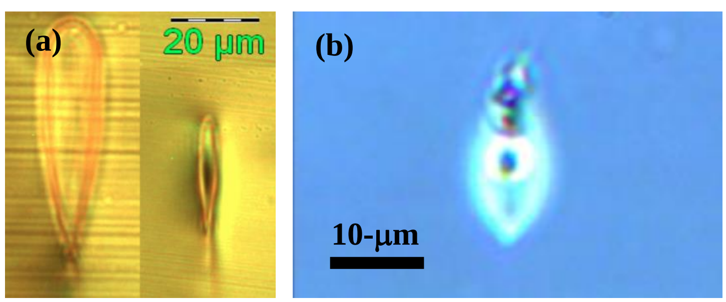


**Figure 3.1.1:** Optical Microscope photo of (a) Waveguides written in GLS glasses by 240-fs pulses at 400-nJ on the left and 200-nJ on the right, and (b) waveguide fabricated in flexible glasses using 300-nJ pulse.

However, the aforementioned laser fabrication challenges are also significant problems for flexible glass materials, especially due to nonlinear beam distortion. To test the quality of waveguides written by ultrafast lasers, we selected two glass materials with different 3rd-order optical nonlinearity $n_2$ to perform laser-matter interaction studies. These included silica-based flexible Corning® Willow® Glass and Gallium Lanthanum Sulphide glass (GLS). Figure 3.1.1 shows waveguides written by the ultrafast laser in an GLS glass (Figure 3.1.1(a)) and in 100µm thick Willow Glass (Figure 3.1.1(b)). The writing beam used a 40x objective to produce transform-limited chirp-free pulses at 180-fs from a Coherent Ti: Sapphire laser. The influences of strong nonlinearity in the laser processing are clearly evident. Strong nonlinear self-focusing and pre-focal depletion produced elongated damage sites in both glasses. They are particularly pronounced in the GLS glass due to its much stronger nonlinearity ($n_2=2.5\times10^{-13}$ cm$^2$/W) than that of silica glass ($n_2=3.4\times10^{-16}$ cm$^2$/W). The asymmetric laser-modified zone and strong material damage around focal points induce strong birefringence and high optical loss. The size of the visible laser modified region in the flexible glass (Figure 3.1.1(b)) is >20-µm. The poor control of laser energy distribution into the focal volume will lead to surface damage (no waveguide formation) in thinner glass substrate (e.g. <50-µm).

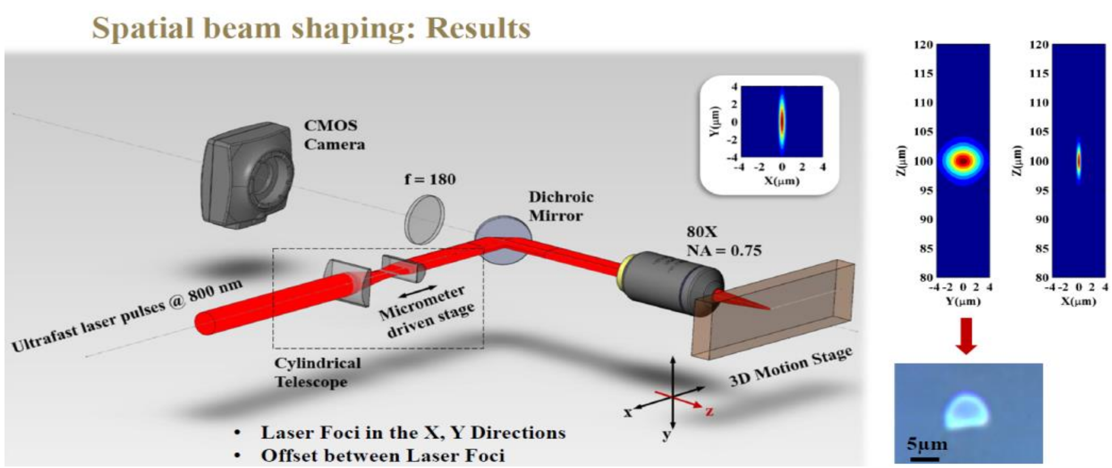


**Figure 3.1.2:** Schematic of ultrafast laser writing setup using a telescope laser beam shaping

To address the unique challenges of flexible glass (thickness < 50 μm) laser waveguide writing, laser spatial beam shaping techniques have been used. A pair of cylindrical lenses is used to introduce beam stigmatic distortion along the laser writing direction. A Coherent RegA 9000 laser system produces laser pulses (300 fs) at 800nm at a repetition rate of 250 kHz. The writing beam is then focused below the sample surface by an 80X aberration-corrected microscope objective (NA = 0.75). During the writing, the flexible glass samples are mounted on a three-axis motion stage (Aerotech ABL2002) and translated in the direction perpendicular to the writing beam and in parallel with the laser polarization. A range of pulse energies from 1000 to 1200 nJ and writing velocities from 2 to 50 mm/s are investigated to optimize the writing parameters for waveguide fabrication in the Willow Glass.

The laser beam shaping is equivalent to introducing a rectangular aperture into the laser beam path as depicted in Figure 3.1.2. If we focus a circular Gaussian laser beam into a transparent material, the energy distribution of the laser beam around the focus point can be expressed as:

$$I_c = \frac{1}{[1+(z/z_0)^2]}\exp[\frac{2(x^2+y^2)}{{w_0}^2(1+(z/z_0)^2)}] \tag{3.1.1}$$

Where $w_0$ is the size of the beam waist and $z_0 = k\, w_0^2/2$ is the depth of focus (Rayleigh range). The energy distribution of a perfect circular Gaussian beam is not symmetric since the depth of focus is much longer than the waist size. This is confirmed by a beam propagation simulation shown in Figure 3.1.3(b).

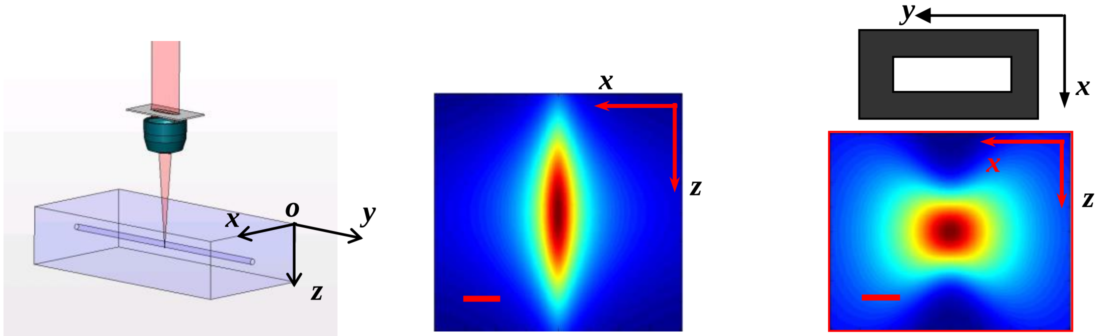

(a) (b) (c)

**Figure 3.1.3:** (a) Schematic diagram of waveguide writing using an amplitude mask. Computer simulations of energy distributions around the focal point produced by (a) a symmetric beam and (b) an aperture with aspect ratio of 6. The black scale bar is the laser wavelength (800 nm), *f* was set as *0.4* (20x objective), the aperture was set as *0.5 mm x 3* mm.

This asymmetric energy profile will produce an asymmetric index change profile for the buried waveguide. To produce an index profile of any desired shape in glass, we can place an aperture in the optical path shown in Figure 3.1.3(a) which will produce an astigmatic focused beam. Since the aperture along the y-direction is longer, the beam will be focused tighter along the y-direction than that along *x*-direction around the focus point. Therefore, the depth of focus (Rayleigh range) of the beam along *y*-direction is also shorter than that along *x*-direction. If we scan the laser beam along the *y*-direction to write a waveguide, the waveguide cross-section will be determined by the waist size along the less-focused *x*-direction and the depth of focus along the tight-focused *y*-direction. By choosing the proper aspect ratio of the aperture, we can create a symmetric waveguide. This is demonstrated in a simulation shown in Figure 3.1.3(c) where we use a 6:1 aspect ratio aperture. This creates an astigmatic beam and leads to a symmetric energy distribution along x-z direction (waveguide cross-section).

After the writing process, the waveguides are characterized by (1) observation of index change profile by optical microscopy; (2) observation of guiding mode profile; (3) measurement of insertion loss; and (4) measurement of propagation loss. For the observation of the guiding mode profile and measurement of propagation loss, the experimental setup shown in Figure 3.1.4 is used. CW laser at 1550nm is launched into the waveguide under test by butt-coupling to a single mode fiber (SMF-28). The output from the waveguide is collected and collimated with a microscope objective (NA = 0.55, f = 180 mm). The collected output is then sent to an integrating sphere to estimate the insertion loss or imaged by a lens on an IR camera to observe its guiding mode profile.

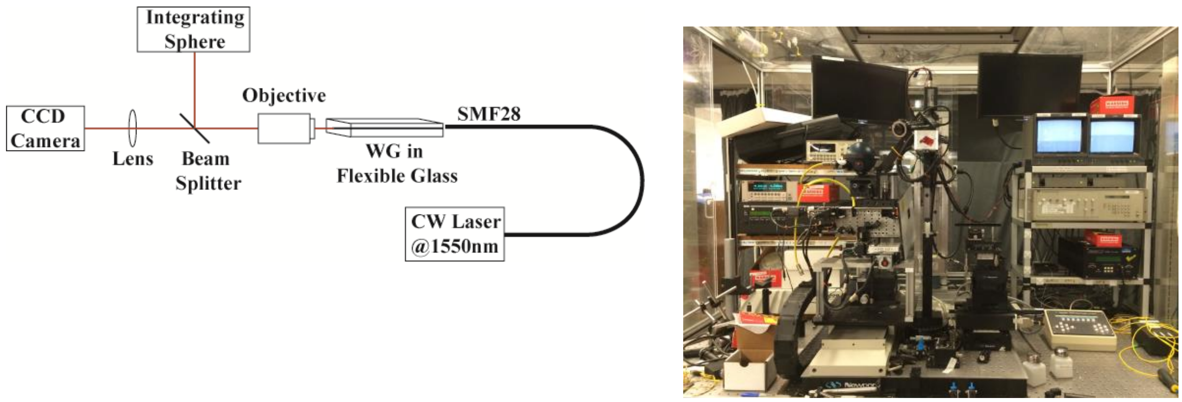


**Figure 3.1.4**: Schematic and photograph of the experiment setup for sample characterization.

## 3.2 EMBEDDED WAVEGUIDE MODE PROFILES

Figure 3.2.1(a) shows the cross-section of a waveguide written under the condition of “perfect focusing” by an 80× aberration-corrected microscope objective without the laser beam shaping. The focal volume is elongated inside the sample, thus the laser-induced plasma forms highly asymmetric stress regions. This results in an asymmetric guiding region. Laser-induced damage (dark region in Figure 3.2.1(a) [35, 36]) is also found in the vicinity of the guide region and leads to significant propagation loss. Furthermore, it is not possible to write waveguides inside thinner glass (thickness < 35 μm) when the elongated guiding region is more than 25 μm. Such an asymmetric waveguide profile is a major limitation of the ultrafast laser writing technique. Poor insertion loss with telecom fibers and high waveguide birefringence could arise from this asymmetry. In contrast, Figure 3.2.1(b) shows the cross-section of a waveguide using a spatially shaped ultrafast laser beam [34]. A much more symmetric guiding profile is generated, and the dark laser damage region has been completely eliminated. Under an optimized laser writing condition (i.e. temporal pulse shaping, spatial beam shaping, writing speed, and pulse energy), highly symmetric waveguides have been successfully inscribed in 25μm, 35μm, 50μm and 100μm flexible glass substrates (Figure 3.2.1(c)).

Writing parameters for ultrafast laser processing in the flexible glass are optimized with the beam shaping setup. The pulse width of the writing beam is fixed at 300 fs, the repetition rate is kept at 250 kHz, and various pulse energies and writing speeds are tested. Samples written using 1.8ps pulse width was also tested, however, the MFDs are 20% larger than those with 300fs pulse width.

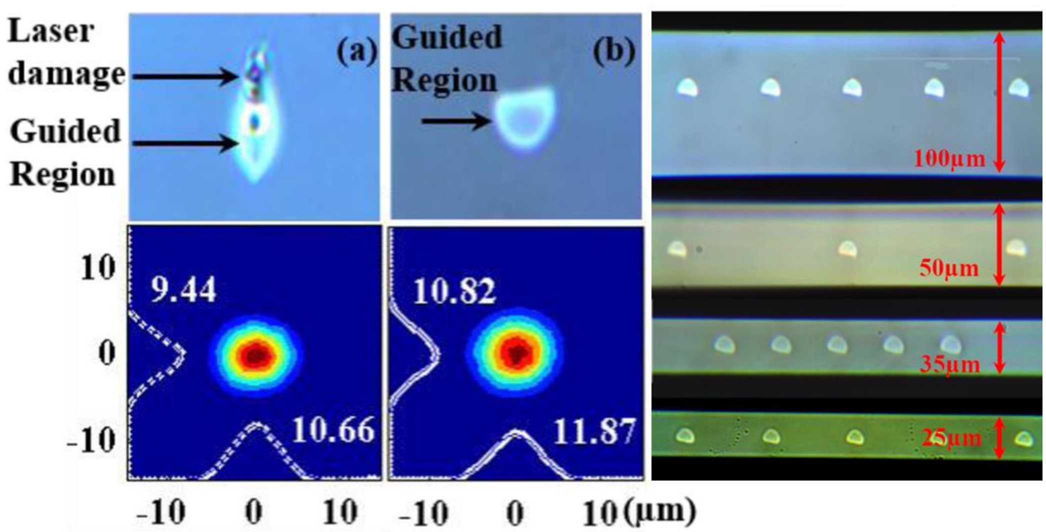


**Figure 3.2.1:** (a) Waveguide formed using an 80X aberration-corrected objective under ‘perfect focusing’ (Top: image of the waveguide cross section; Bottom: Guided mode profile at 1550nm); (b) Waveguide formed by spatially shaped laser beam to introduce strong astigmatism to control the focal volume (Top: image of the waveguide cross section; Bottom: Guided mode profile at 1550nm); (c) From top to bottom, waveguides formed in 100μm (top), 50μm, 35μm, and 25μm (bottom) flexible glass substrates.

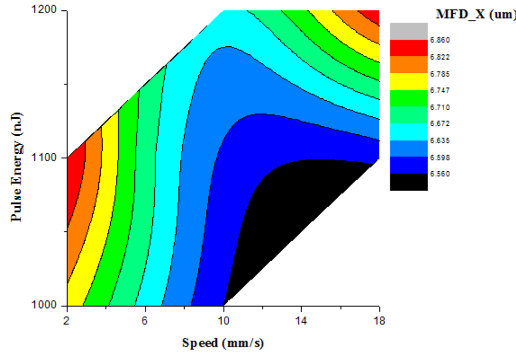


**Figure 3.2.2:** MFD as functions of pulse energy and laser writing speed in 100μm glass.

Using a 300-fs laser pulse, the laser processing window was explored in 100μm thick flexible glass. Waveguides were written with the pulse energy set at 1000, 1100, and 1200 nJ, and the writing speed set at 2 – 18 mm/s. A 2.0 cm long and 100 μm thick flexible glass substrate was used in the experiment. Mode field diameter (MFD) as a function of pulse energy and writing speed is shown in Figure 3.2.2. Within the entire processing window, MFD at 1550nm perpendicular to the laser beam writing direction (x-axis in Figure 3.2.1) is less than 7μm. This is similar to the size of the visible laser modified area shown in Figure 3.2.1(c). Comparing this with the MFD of standard telecommunication fiber (Corning® SMF-28®), we can estimate that the refractive index contrast induced by the ultrafast laser is ~$5\times10^{-3}$.

## 3.3 EMBEDDED WAVEGUIDE PROPAGATION LOSS

Measurements of the propagation loss are based on optical frequency domain reflectometry (OFDR), and are carried out on the ultrafast laser written waveguides by an optical backscatter reflectometer (OBR) (LUNA OBR4600). Either a Tunable laser output centered at 1550nm or a broadband source is butt-coupled to the waveguide under test via a single mode fiber (SMF-28) mounted on a 3-axis translation nanostage. Index matching gel was applied to both ends of the waveguide to reduce the impact of the reflection peaks from the two the substrate facets.

Figure 3.3.1(a) shows a measurement trace of a 11.4cm-long waveguide written in a 100um-thick flexible glass substrate with optimized writing conditions (i.e. 300fs pulse width, 1000nJ pulse energy, and 10mm/s translation speed). The peaks in the trace denote the front and back facets of the substrate, respectively. By linear fitting the trace between the two reflection peaks, the propagation loss of the waveguide is indicated by the slope of the fitted line. With the optimized writing parameters, the propagation loss of the waveguide written in the flexible glass is 0.11 dB/cm. The measurement is repeated on 10 different waveguides in the same sample with the same writing parameters. All waveguides yield similar guiding performances with low propagation loss ranging from 0.1 dB/cm to 0.25 dB/cm as shown in Figure 3.3.1(b). These results are among the best loss performances of waveguide structures made by ultrafast laser processing. The processing speed can be increased to 50 mm/s to form waveguides with the same low loss.

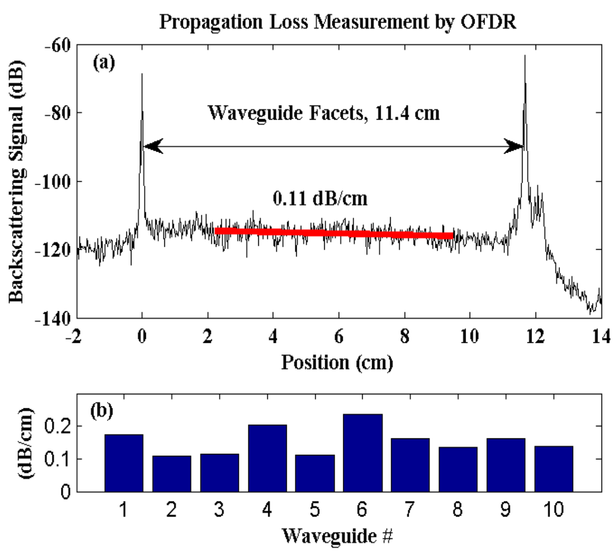


**Figure 3.3.1:** (a) Propagation loss measurement by OFDR. Propagation loss of a waveguide in an 11.4cm-long flexible glass substrate is indicated by the slope of the fitted data between the two facets. (b) Waveguide propagation losses measured on 10 waveguides (WG) written using the same processing conditions as in (a).

Although it is still in the very early experimental stages, waveguide performance in terms of optical loss (Figure 3.3.1) are already significantly better than state-of-the-art of flexible polymer waveguides of ≥0.3-DB/cm at $\lambda$=1550nm (Table 1). Both the optimized laser processing parameters and better bulk optical qualities shown in Figure 2.4.3(b) contribute to superior guiding properties. It is also important to note that glass materials used for our experiments are not significantly different from other existing glass substrates except being thinner. Thus, the flexible glass substrates retain superior optical/mechanical properties associated with glass materials.

## 3.4 EMBEDDED WAVEGUIDE BENDING LOSS

The ultrafast laser written waveguides in flexible glass are also characterized for bending losses. Figure 3.4.1 shows photographs of waveguides in 35µm, 50µm and 100µm thick flexible glass with bending radii of 13.5cm (Figure 3.4.1(a)), 2.1cm (Figure 3.4.1(b)), and 1cm (Figure 3.4.1(c)-(d)), respectively. As shown in Figure 3.4.1, guiding functionality is maintained for all cases, where 532nm Green laser coupled into the waveguides is used in the photographs for visualization purposes.

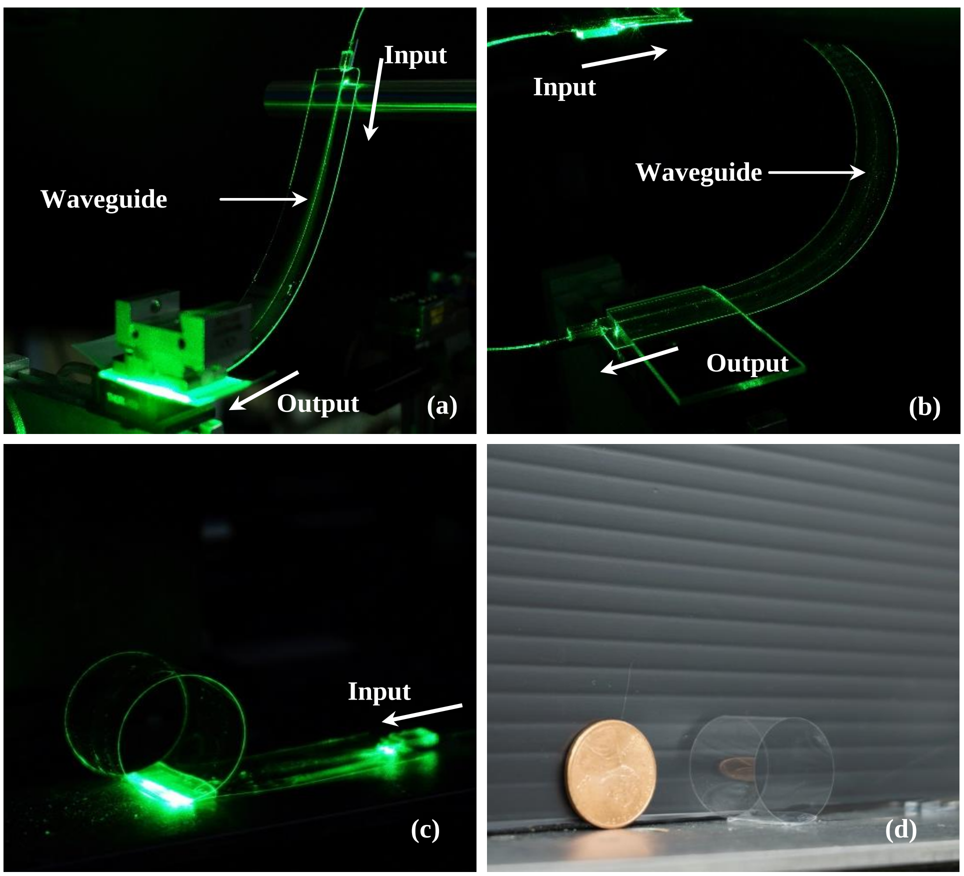


**Figure 3.4.1:** Flexible glass waveguides written in (a) 100 µm thick substrate with 13.5cm bending radius; (b) 50µm thick substrate with 2.1cm bending radius. (c) 35µm thick substrate with 1.0cm bending radius; (d) The same 35µm thick substrate with 1.0cm bending radius.

Waveguide bend loss inscribed in 25μm, 35μm, 50μm, and 100μm thick samples are measured at various bending radii and presented in Figure 3.4.2. The measurements show only a small fluctuation of additional insertion loss $\delta IL$ < 0.05 dB around the average insertion loss when the bending radius is larger than 6.7 cm for 100-μm samples. For glass samples with thickness between 25 and 50 μm, the insertion loss due to the bending is less than 0.3 dB for bending radius down to 2.0cm. This is similar to the bending performance of standard telecommunication fibers while significant bending loss occurs at a ~2-cm bending radius. This measurement data suggests that low-loss waveguides in flexible glasses have similar index contrast and waveguide profiles to those of optical fiber (i.e. $\Delta n \sim 5\times10^{-3}$). It is also possible to produce higher refractive index contrasts through multi-pass laser writing, however, this process might incur higher waveguide propagation loss. This index contrast is lower than other flexible waveguides, however, built using hybrid approaches as shown in Figure 3.1.2. It is nevertheless comparable to low loss waveguides built entirely by polymer materials.

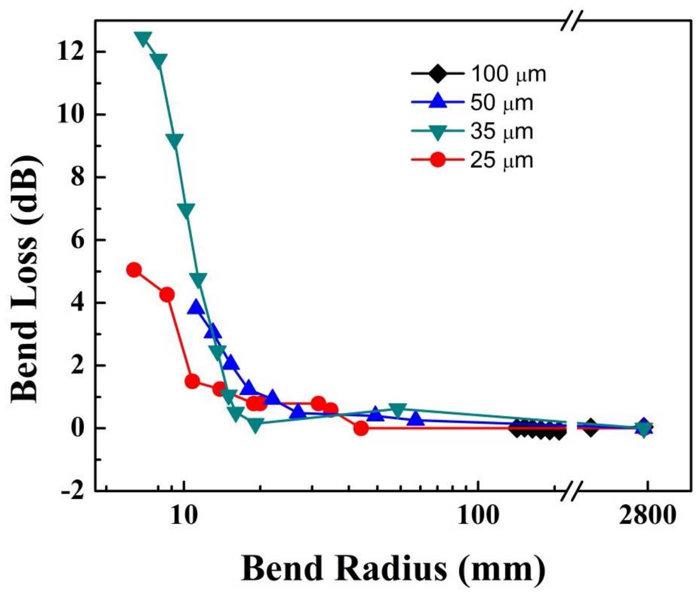


**Figure 3.4.2:** Insertion loss of the ultrafast-lase-written waveguide in 25μm, 35μm, 50μm, and 100μm thick flexible glass substrates with bending radius down to 0.67cm.

### 3.5 EMBEDDED WAVEGUIDE THERMAL STABILITY

To test thermal stabilities of waveguides inscribed by the ultrafast laser, thermal aging tests were performed on low loss waveguides written with 1000-nJ and 1160-nJ pulses with 300-fs duration, respectively. The thermal aging tests were performed using a box furnace by heating the glass waveguide samples to 250°C, 300°C, 350°C, 400°C, and 500°C. Glass waveguide samples were kept in a designated temperature for one hour and cooled down to the room temperature over a period of 24 hours. After each heating cycle, the size of waveguides were measured under an optical microscope and compared with that before the heating. The guiding mode profiles were also measured and compared shown in Figure 3.5.1.

The microscope images in Figure 3.5.1 show no change in the waveguide for 250°C, 300°C, 350°C, and 400°C heating cycles, but apparent fading is observed after the 500°C heating cycle. The mode profiles reveal that the mode field diameter for the waveguide increased by 21% from 12.84 µm at room temperature to 15.59 µm after heating at 500°C. The above result shows that, compared with flexible polymer waveguides which start to have weight loss and optical property changes starting at 100°C, the flexible glass has a much higher long term thermal stability up to 400°C enabling its practical use in high temperature.

Figure 3.5.1(a) shows the optical guided mode profile at 1550nm for a waveguide written by 1000-nJ pulse energy. No significant change in term of the size of guided mode profile was observed at 300$^{o}$C. However, the heating at 500$^{o}$C causes a noticeable increase of mode field diameter from ~12.8-µm to ~15.6-µm. This suggests that a thermal erasing of refractive index change occurs at 500$^{o}$C. In contrast, waveguides written at higher pulse energy of 1600-nJ show slightly improved thermal stability up to 350$^{o}$C as shown in Figure 3.5.1(b).

Figure 3.5.1(c)-(d) present changes of insertion loss of waveguides as functions of thermal annealing for waveguides written at 1000-nJ and 1600-nJ pulse energy, respectively. The increased insertion loss at >400$^{o}$C once again suggest thermal erasure of waveguides which increase the mode miss-match between fiber and waveguides. It is also interesting to note that waveguide insertion loss was reduced at slightly lower thermal annealing temperatures. This is probably due to that the thermal reflow process that might occur at these temperatures. This might lead to more uniform waveguide profiles and less scattering loss on waveguide core/cladding interfaces.

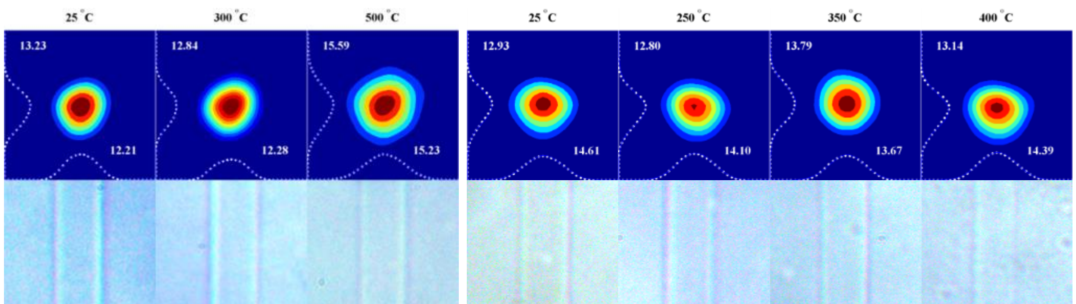


(a) (b)

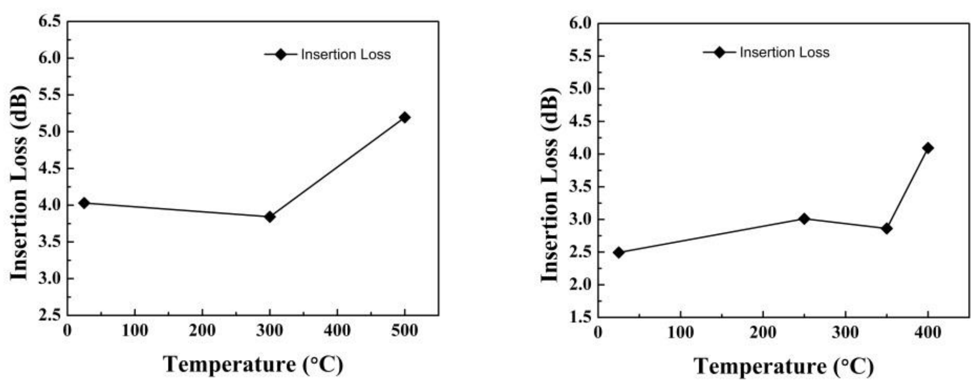


(c) (d)

**Figure 3.5.1:** Mode profiles (top) and microscope images (bottom) of waveguides written with (a) 1000-nJ and (b) 1160-nJ laser pulses, after 1 hour baking for each temperature. (c) Waveguide attenuation for each temperature, written with 1000-nJ pulses w. (d) Waveguide attenuation for each temperature, written with 1160-nJ pulses.

### 3.6 BRAGG-GRATING WAVEGUIDES (BGW) IN FLEXIBLE GLASS

Similar to the uniform waveguide writing, Bragg grating waveguides can also be fabricated by translating the substrate in relation to a fixed focal position using the three-axis motion stage. Through the periodic modulation of the acoustic-optic modulator in the regenerative laser amplifier during the waveguide writing process, both uniform and periodic waveguide sections can be formed in a single laser pass. The induced periodic index modulation form Bragg reflectors. The modulation frequency of the acoustic optical modulator in the laser amplifier is given by $f = \frac{2n_{eff}v}{m\lambda_B}$ [37], where $n_{eff}$ is the effective refractive index of the guided mode, $v$ is the translation speed of the sample, m is the grating order, and $\lambda_B$ is the Bragg resonance wavelength. To demonstrate the application in the telecom range, the BGWs in this work were designed for a central wavelength of $\lambda_B$ ~ 1550 nm and $n_{eff} = 1.496$ with a fixed writing speed $v = 1$ mm/s. The grating order is chosen to be $m$ =4, with a duty cycle of 25% and a writing beam pulse energy 1160 nJ. It is found that 25% duty cycle provides the best fringe visibility and leads to strongest resonant wavelength peaks [38]. It is noted that the optimized writing pulse energy for single mode waveguides in flexible glass is 1000 nJ. The pulse energy for Bragg grating waveguide formation to compensate for the lower average energy deposited for adequate DC index change due to the 25% modulation duty cycle. Figure 3.6.1 show both optical microscope topview and cross-section views of Bragg grating waveguide in 50μm thick flexible glass. The period of the 4th order grating at 1550nm is 2.082μm. The Bragg grating waveguide exhibits similar waveguide cross-section (Figure 3.6.1(b)) to those of uniform waveguide written by 1000nJ pulse energy.

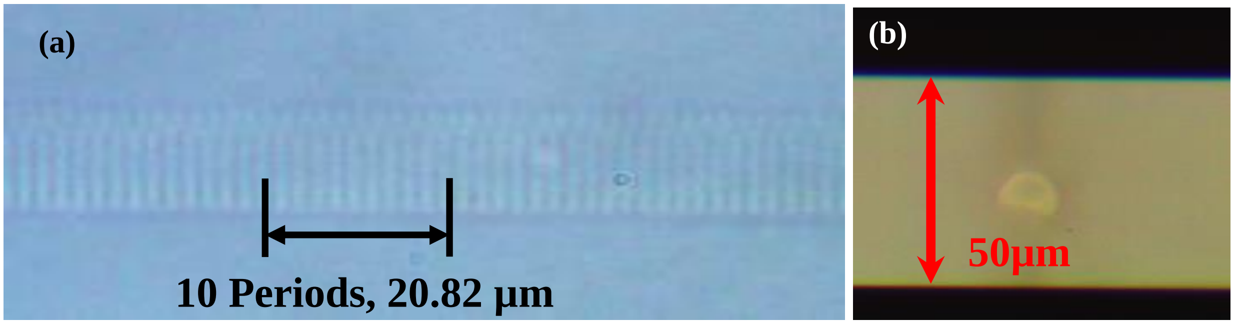


**Figure 3.6.1:** (a) Optical microscope photographs (a) topview of a 3rd-order Bragg grating waveguide and (b) end view of Bragg grating waveguide in 50µm thick glass.

The experimental setup for the Bragg grating waveguide characterization is shown in Figure 3.6.2(a). A broadband emission (MPB EBS-7210 $Er^{3+}$ broadband source) centered around 1550nm was coupled into BGWs using cleaved SM28+ fiber mounted on a V-groove chip. The launch fiber was connected with a circulator for collecting the reflection spectrum, are the transmission was collected with a second fiber coupled with the guided mode after the objective. The signals were recorded on an optical spectrum analyzer (OSA) for data analysis. Figure 3.6.2(b) shows the corresponding transmission and reflection spectra of a 3thorder ($m$ = 3) Bragg grating waveguide.

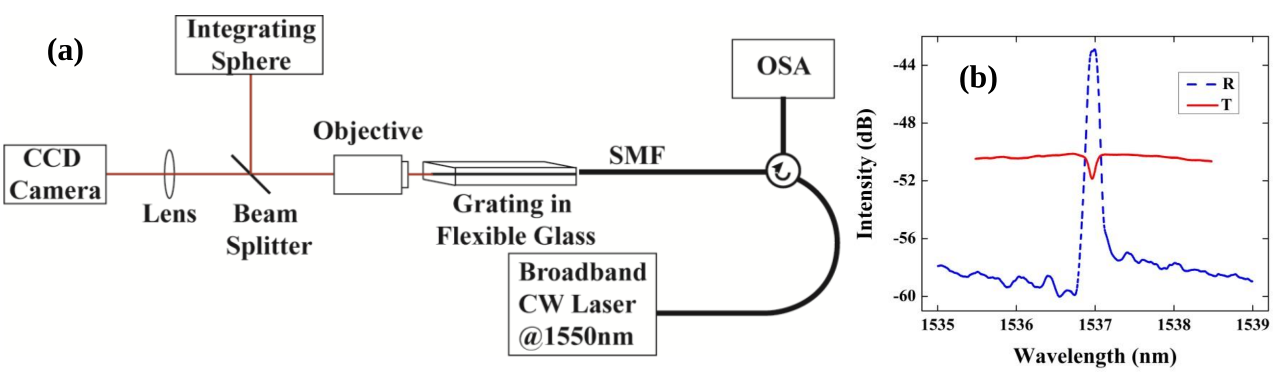


**Figure 3.6.2:** (a) Experimental setup for Bragg grating waveguide characterization, and (b) a typical reflection and transmission spectra of a 3rd order Bragg grating waveguide with 25% duty cycle.

Similar to the waveguide thermal stability test, Bragg grating waveguides written with 1160nJ pulses with 300fs duration were characterized in several heating cycles at 250°C and 350°C. Each of these were held for 1 hour. The samples were cooled down to room temperature after each cycle, observed using optical microscope, and characterized for Bragg resonance wavelength. Figure 3.6.3(a) shows a white light microscope image of the 3rd order Bragg grating waveguides were viewed from the direction of the incident beam. Similar to the waveguide thermal stability test, there is no change in the grating fringe visibility for all the heating cycles. Figure 3.6.3(b) shows that the grating strength remains stable up to 350°C, and this is consistent with the written uniform waveguides.

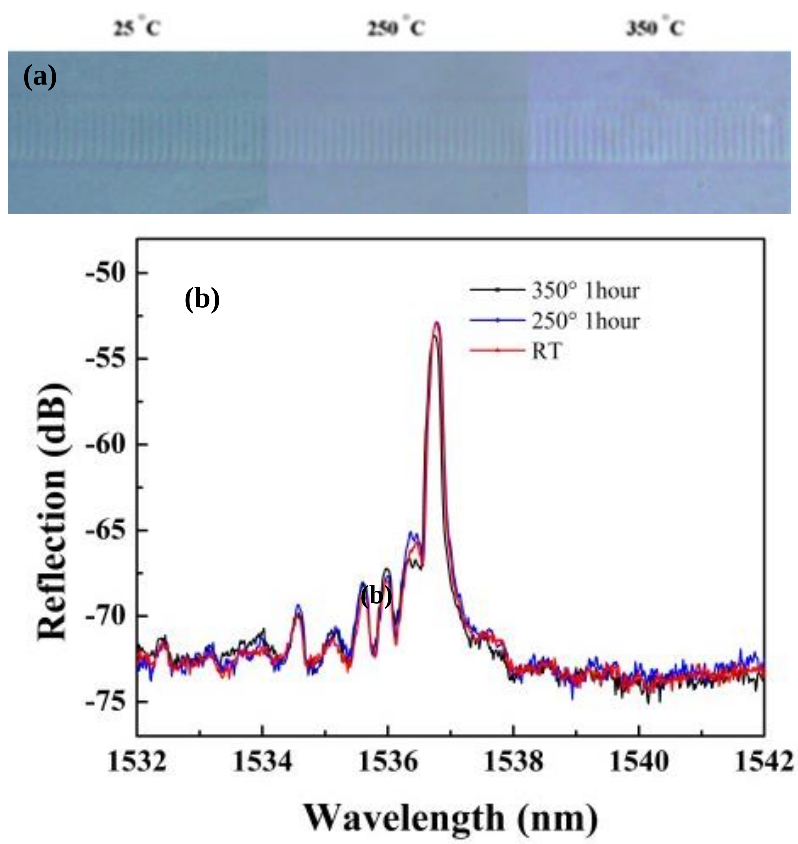


**Figure 3.6.3**: (a) Top view of ultrafast laser written Bragg grating waveguides in flexible glass using modulation with 25% duty cycle. (b) Bragg grating reflection spectra after two heating cycles.

## 3.7 EMBEDDED WAVEGUIDE BIREFRINGENCE

Using the rotating extinction method [39-41], the birefringence of uniform waveguides was measured. Under the laser writing condition optimized for the lowest propagation loss (writing speed = 10mm/s, pulse energy 1000nJ at 300fs), the birefringence of the waveguides was measured at $0.45\times10^{-5}$. This very low birefringence, which is similar to the birefringence in standard telecommunication fibers, is due to the highly symmetric waveguide profile optimized by the spatial laser beam shaping technique. The birefringence of Bragg grating waveguides can be measured by monitoring the Bragg wavelength shift under polarized guided mode (TE and TM). Figure 3.7.1(a) shows the setup for birefringence measurement of BGWs. Compared to the experimental setup shown in Figure 3.7.1, the launch fiber has been replaced by free space coupling using aspherical lens with NA =0.14, while the polarization of the launched laser beam is controlled by a polarizer and a half-wave plate (HWP). By measuring the maximum Bragg peak wavelength difference, the birefringence of the waveguide ($n_p$-$n_s$) can be simply calculated using the Bragg wavelength split $\lambda_p$-$\lambda_s$ as: $n_p - n_s = \frac{m}{2n_{eff}}\left(\lambda_p - \lambda_f\right)$, where $m$ is the order of Bragg grating and $n_{eff}$ is the effective index of the waveguide. Figure 3.7.1(b) shows a typical measurement result for 4th order Bragg grating waveguide, while 3pm Bragg wavelength shift was measured in reflection spectra. This corresponds to a waveguide birefringence of $0.58\times10^{-5}$, which is similar to the measurement results in uniform waveguides in flexible glass.

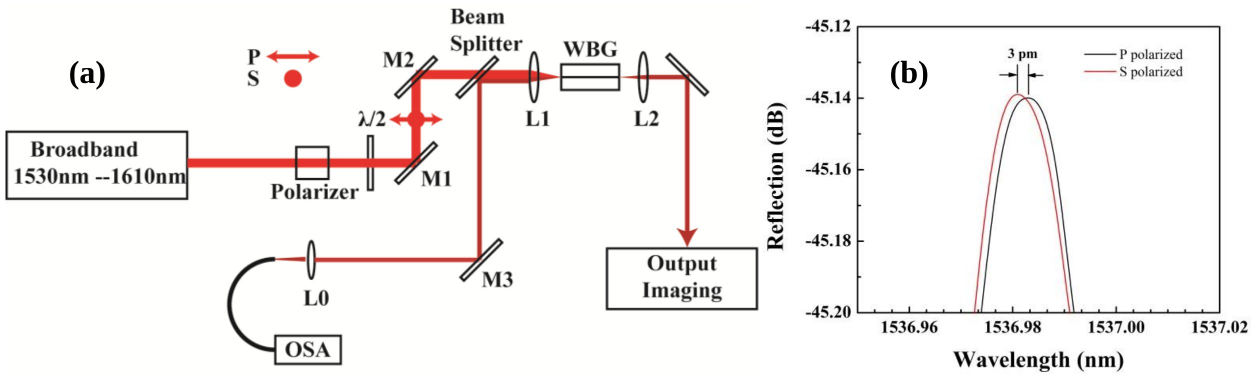


**Figure 3.7.1:** (a) Schematic of experimental setup for BGW birefringence measurement. (b) Bragg grating reflection spectra for two perpendicular polarized light.

# 4.0 ULTRAFAST-LASER FABRICATION OF LIGHTWAVE CIRCUITS AND BOARD-LEVEL OPTICAL INTERCONNECT ON GLASS

In this section, the Ultrafast laser fabrication approach is enhanced to form a versatile fabrication platform and then is optimized as a potential candidate for telecommunication applications. Three building-block components were monolithically fabricated. We report ultrafast laser fabrication of waveguide circuits and 45° vertical coupling micromirrors in fused silica for optical interconnect applications. Excellent micromirror surface quality was obtained and 0.24-dB per reflection at 632nm was demonstrated. Furthermore, we demonstrated ultrafast laser fabrication of waveguide circuits in optical fibers with rectangular cross-section and large flat surface area designed for on/in fiber integration. Low-loss coupler and wavelength division multiplexing (WDM) devices are directly integrated in fibers. Finally, a 3-D integrated waveguide coupler for cladding-pumped rare-earth-doped multicore fiber amplifier was designed, fabricated and characterized.

## 4.1 INTRODUCTION OT OPTICAL INTERCONNECT AND FIBER BASED TELECOMMUNICATION

Optical waveguide interconnect has been considered as a key enabling technology to address bandwidth bottleneck limited by electrical wire at board levels [42]. Most of waveguide components for board-level optical interconnects were realized based on polymer substrates. The board-level optical interconnect involves both waveguide technology and micro-optic elements to couple light to and from vertically mounted opto-electronic components such as laser sources, photo-detectors, and modulators. Various approaches have been proposed to realize vertical interconnects, including the grating couplers [43], curved waveguides [44], and the 45° micromirrors. As a structure that is insensitive to wavelength selection, the 45° micromirror becomes a superior candidate for board level and chip level vertical interconnects. Several technologies have been applied to fabricating out-of-plane 45° micromirrors, such as molding [45], diamond blade micromachining [46], Deep Proton Writing (DPW) [47], and also in-plane 45° ultrafast-laser-assisted wet etching on photosensitive glass [48].

As mentioned in section I, data rate is exploding in short-haul communication systems in modern days, the optical power required to support high data bandwidth in optical waveguides also needs to increase dramatically. The poor thermal stability of polymer is becoming a limitation of the usability of polymer photonic devices for high bandwidth applications. There is strong interest in exploring optical interconnect technology based on glass materials.

On the other hand, for the long-haul high volume data transmission, ever since its invention in the 1960s, silica optical fiber has played key roles in revolutionizing many aspects of modern technology. As optical waveguides, high-quality optical fibers can be massively produced through a preform-to-fiber manufacturing scheme at very low-cost. Commercially off-the-shelf optical fiber has optical loss <0.2 dB/km at telecom wavelengths [49], which is ~10,000 times less than waveguides fabricated on flat wafers. Since its inception, functionalities of optical fibers have been largely limited as one-dimensional devices for optical signal and power transmission. Recently various efforts have been invested by researchers to improve functionalities of optical fiber through on-fiber integration of functionality materials and in-fiber sculpturing of opto-mechanic structures [50]. However, these efforts are severely limited by lack of surface areas and bulk volumes for device integration. The on-fiber integration is also strained by the cylindrical shape of the optical fibers, which pose significant challenge for current fabrication techniques.

Over the years, spatial division multiplexing (SDM) has been pushing the transmission bandwidth limit of optical communication. Using multicore and multimode optical fibers, an increase is accomplished in the capacity of a single fiber, and the cost per transmission bit is reduced. To cope with emerging SDM applications, multicore and multimode fiber amplifiers have been employed to amplify all spatial channels [51-55]. There are two pump coupling schemes for coupling of both pump light and the signal light into different spatial channels. In core pump, pump light propagates in each core [52]. In cladding pump, a single pump beam propagates in a common inner cladding which pumps all spatial channels

## 4.2 ULTRAFAST LASER FABRICATION OF 3-D PHOTONICS CIRCUITS AND MICROMIRRORS ON BULK GLASS

In this part of the work, a Coherent RegA laser system producing 250-fs pulses (FWHM) at 800-nm is used to perform both the laser waveguides writing and the V-mirrors fabrication. The repetition rate of laser is set at 250 kHz. Before entering the focusing objective, the ultrafast laser beam is spatially shaped by a pair of cylindrical lenses to adjust the size and shape of the focal volume in order to induce symmetric index change profiles for waveguides [56]. The laser is then focused into glass samples using an 80× aberration-corrected objective (NA=0.75). Fused silica glass samples are mounted on a three-axis motion stage (Aerotech ABL2002) and translate in the desired direction to form waveguide circuits and to expose volume for subsequent HF etching process. Figure 4.2.1 illustrates one typical moment during the laser fabrication process.

The schematic sketch of the optical interconnect devices is shown in Figure 4.2.2(a). At one of the V-shape volume, when the light is vertically incident onto the 45° glass/air interface from the flat (un-etched) glass surface, TIR condition will be satisfied, and the light will be redirected in-plane to couple into the waveguides. The 45° angle is defined as the angle between the slope of the V-shape and the surface of the fused silica glass chip. With bulk index $n_0$=1.457 for fused silica, 45° is more than the minimum angle for TIR, as calculated in (1). Therefore at the 45° glass/air interface, the light will be totally reflected to ensure low loss performance. At the same time, its direction changes 90°, leading to a vertical bending of the light:

$$\alpha = \arcsin(\frac{1}{n_0}) = 43.8^{\circ} < 45^{\circ} \qquad (4.2.1)$$

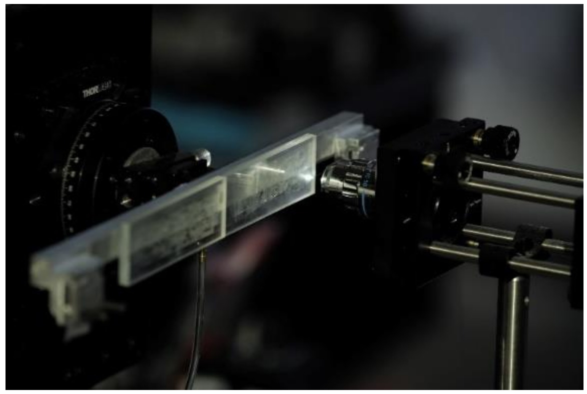

**Figure 4.2.1.** Optical fiber fabrication platform: ultrafast laser direct writing setup

The laser fabricated optical interconnect devices mainly consist of two procedures:

The first procedure is called the laser writing procedure. In this procedure, the focused laser beam was scanned line-by-line along 90° V-shaped path to expose two V-shaped volumes with two 45° slope surfaces to be used as TIR micromirrors. The laser scanning step size was 15 μm per line. At this stage, the laser pulse energy was 1600 nJ and a writing speed of 1.6 mm/s was used. The second laser writing stage formed a 1×2 waveguide splitter as illustrated in Figure 4.2.2(a). Embedded waveguide was written by pulse energy of 880 nJ with a writing speed of 1.0 mm/s. The change in pulse energy and writing speed was set up automatically by the program that controls the laser beam delivery system and the 3-axis motion stage.

In the second procedure, the entire glass chip was etched by a 12.5% (volume ratio) HF solution after the laser writing procedure was completed. This etching process selectively removed the V-shaped volume exposed to the laser focal volume due to the formation of nanograting caused by high intensity ultrafast laser radiation [57]. The embedded waveguides formed during the first procedure were inside the bulk of the glass chip and remained intact during the etching process.

The etch rate for the exposed area in the glass chip is estimated as 5 μm/min. In comparison, the etch rate is 0.02 μm/min (aspect ratio of etch rate is ~250) for the unexposed area on the same glass sample. During the first procedure, the direction of the writing laser beam polarization is set to be perpendicular to the direction of the sample translation in order to maximize the fabrication speed [57]. Furthermore, the 90° V-shaped scanning path is optimized in such a way that it is only cutting through the sides of the V-shaped volumes, instead of scanning through the whole V-shaped volume. After the wet etching procedure, the V-shaped volume was simply cut out as a whole. This simple technique shortened the laser scanning time by one order of magnitude.

Interrogation and a demonstration of the micromirror waveguide structures is done by vertically coupling a single-mode fiber onto the glass sample. As shown in Figure 4.2.2(b), the single-mode fiber was first aligned and then vertically glued to couple light into the input side of the 1×2 waveguide splitter. Figure 4.2.2(e) shows the optical microscope cross-section image of a waveguide. Using the spatially shaped ultrafast laser beam, the focal volume was optimized to yield symmetrical waveguide, as shown in the cross-section image. To characterize the performance of this optical interconnect structures, a 632 nm laser source was butt-coupled to the waveguide under test via a single-mode fiber (SMF-28®) mounted on a 3-axis translation stage. The output from the in-plane waveguide or from the 45° micromirror was imaged by a CCD camera, or sent to an integrating sphere to measure transmitted optical power.

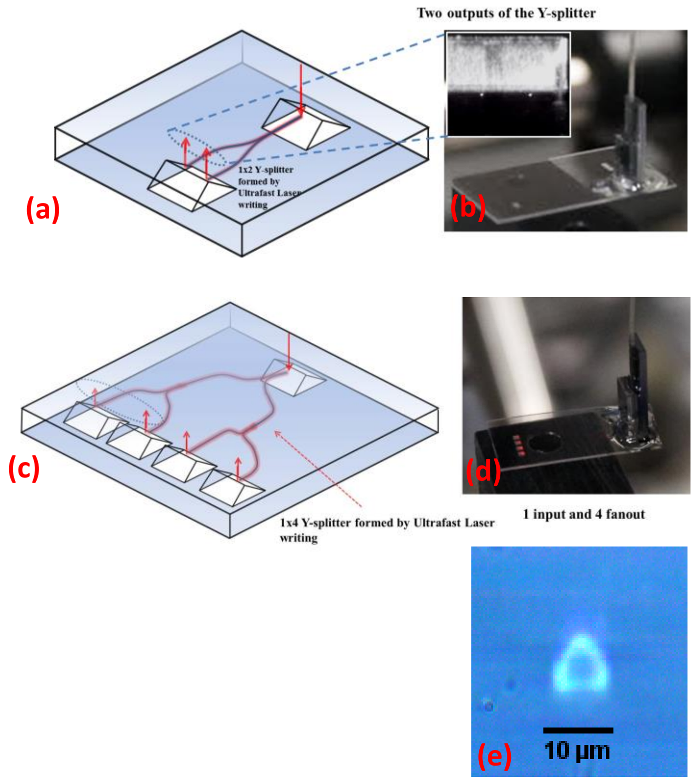


**Figure 4.2.2**: (a) Embedded 1x2 splitter sketch; (b) measurement photograph; (c) embedded 1x4 splitter sketch; (d) measurement photograph; (e) optical cross-section of a single waveguide.

As shown in Figure 4.2.3(a), the Scanning Electron Microscope (SEM) image reveals a rough surface with periodic textures, indicating a low surface quality. A magnified SEM zoom-in view at the V-mirror slope surface shown in the inset of Figure 4.2.3(a) reveals the period of the surface texture is 15 μm. The rough texture is expected to appear and its period is consistent with the above-mentioned laser scanning patterns. However, with such a low quality reflection surface, when light incident on the glass/air interface, the incident angle can be calculated as a set of all possible values due to the scattering. For most of these incident light, the TIR condition will not be satisfied, resulting in a huge reflection loss.

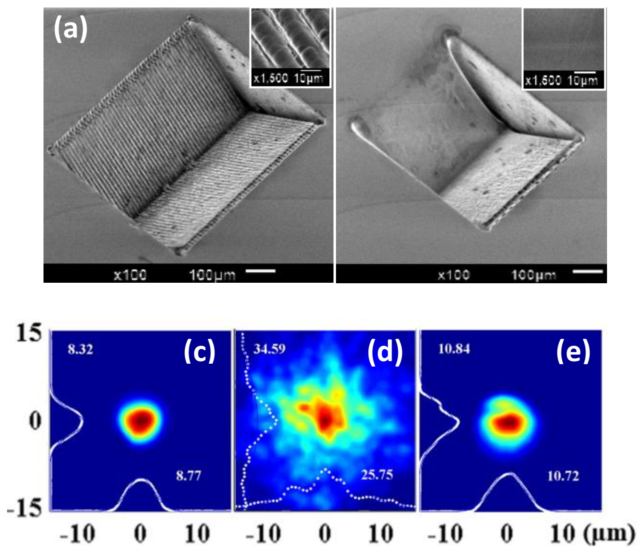


**Figure 4.2.3**: (a) SEM view of micromirror before thermal reflow, inset: zoom-in view; (b) SEM view of micromirror after thermal reflow; (c) guided-mode image of the waveguide without V-mirror; (d) guided-mode image after the reflection from a mirror surface without CO2 laser reflow; (e) guided-mode image after the reflection from a mirror surface with CO2 laser reflow

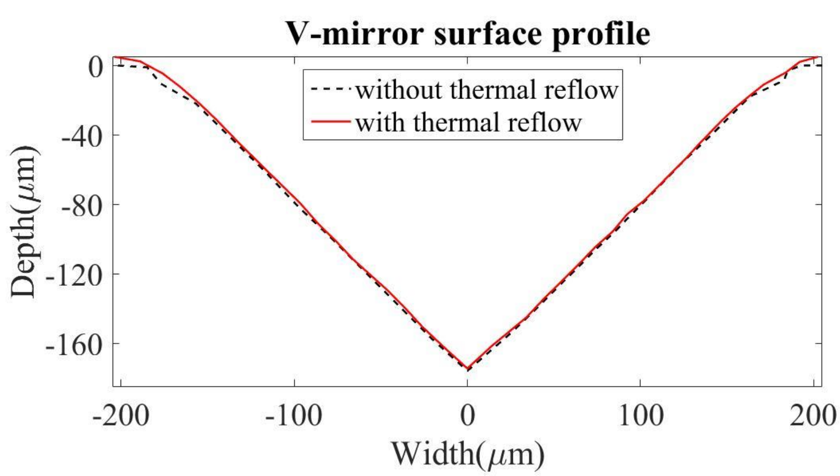


**Figure 4.2.4:** Surface profile of the V-mirror before and after CO2 laser processing.

In an effort to improve the surface quality of the micromirrors, an additional procedure is introduced. We reflowed the surface of the micromirror using an unfocused CO2 laser beam. The CO2 laser beam waist versus the distance away from the perfect focusing beam spot was also calibrated. This calibration result was then used to control the reflowed area size to cover the whole V-mirror area, with no detrimental effect on adjacent area. As a result, the CO2 laser beam (~1000 μm in beam size) was applied only to the V-shaped micromirror region. Moreover, the laser power and exposure time were carefully adjusted to optimize the surface quality of the micromirrors.

The resulted SEM image in Figure 4.2.3(b) and its zoom-in view in the inset show a much smoother 45° surface after the CO2 laser reflow process. The rough periodic texture surface features were completely eliminated. Judging only from the SEM image, the CO2 laser reflow process might appear to also have introduced a small curvature to the mirror surface. However, as shown in Figure 4.2.4, the surface profiler measurement indicate a very reasonable geometrical deviation (< 2 μm shift as a whole) with and without CO2 laser reflowing.

Moreover, the enhanced surface quality of the V-mirror leads to a huge improvement on both mode profiles and transmission loss. Figure 4.2.3(d)-(e) showcase the difference in guided mode images at 632 nm reflected from micromirrors, without (Figure 4.2.3(d)) and with the CO2 laser treatment (Figure 4.2.3(e)). Each of them is compared with the original guided fundamental mode profile at 632 nm directly from a waveguide (not reflected from micromirrors) in the waveguide, as shown in Figure 4.2.3(c). It is clear in this comparison that the rough glass/air interface without the thermal reflow results in heavy scattering of light at the micromirror as shown in Figure 28(d). Although the mode in Figure 4.2.3(d) is still confined, its mode field diameter (MFD) is three times larger than that of the original. In contrast, Figure 4.2.3(e) presents a mode profile reflected from the CO2 laser reflowed micromirror. A huge improvement on mode confinement is observed, with the heavy scattering complete gone. We further noticed that the mode profile is slightly asymmetric with the intensity concentrated towards the bottom, consistent with the predicted result from the simulation in [58]. By comparing the power transmission measurement of mode profiles in Figure 4.2.3(c)-(e), we found that the net loss caused purely by the micromirror is 3.36 dB for a micromirror without thermal reflow process and only 0.24 dB for a reflowed micromirror.

Figure 4.2.2(c) is also a demonstration device of an integrated photonic circuit with 3 vertical optical interconnecting points. The light from the glued fiber end is coupled into the waveguide by TIR of the first micromirror. The guided light is then split equally between the two fanout waveguides, and finally coupled out by the second micromirror. After two 90° bending, the light propagation therefore made a complete reverse of direction. In Figure 4.2.2(c) and (d), we extended the fanout to a total of 4 by cascading two levels of the 2-fanout Y-splitter.

## 4.3 FABRICATION OF LIGHTWAVE CIRCUITS ON FLAT FIBERS: SYSTEM-IN-FIBER

Shown in Figure 4.3.2(a), the optical fiber has rectangular cross-section with two flat side surfaces amendable for on-fiber device fabrication and integration using both laser and lithography-based microfabrication schemes. Multiple fiber cores with different dopants and numerical apertures (NA) are fabricated in the fiber. Using the ultrafast laser direct writing, waveguide devices with length from several mm to several meters can be readily fabricated in-fibers, which turn an optical fiber from a 1-D optical channel to 3-D integrated systems. This part of the work explores this possibility. Using the ultrafast laser direct writing scheme, we demonstrates the fabrication of low-loss couplers and WDM components, two key components for fiber lasers, to interact lights between two fiber cores.

The fabrication of the rectangular fiber is a collaborative work with Corning Inc. The process utilized Outside Vapor Deposition (OVD) to produce a rectangular fiber preform made from fused silica. After repeated thermal annealing to relieve stress induced during the sintering process, the fiber preform is drawn into optical fibers. The cross-sectional view (Figure 4.3.2(a)) shows that the dimension of the rectangular profile is 120 μm thick and 300 μm wide, with two flat surfaces for device fabrication and integration. This fiber also consists of five fiber cores including two identical cores with the same index profiles and core composition as Corning's standard telecommunication fiber SMF-28. All fiber cores are located roughly 60-μm below the surface. The configuration and relative position of the fiber cores are slightly distorted by the preform consolidation process. In this part of the work, only the two SMF-28 cores are being utilized.

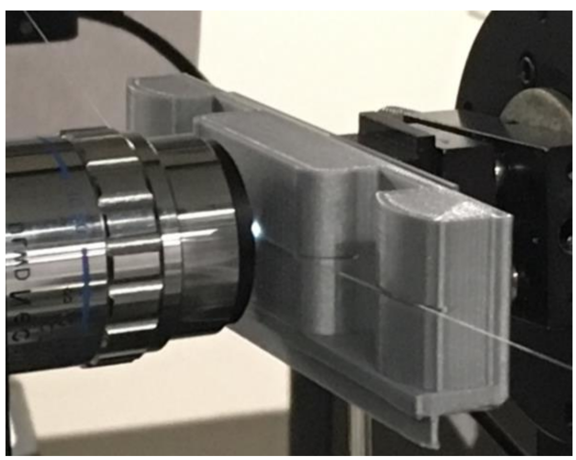

**Figure 4.3.1:** Roll-to-roll laser processing fiber setup.

The same Coherent RegA laser system at 800 nm is used to in this part of the work. To properly secure the fiber during the writing process, a specially made fiber mount was designed and 3-D printed, as shown in Figure 4.3.1. The mount includes 4 contact points that keep the tension along the fiber while the fiber is moving. During the laser writing, the fiber is sliding within fiber mount's grooves to minimize any vibration caused by movement from the two far ends of the fiber. There, the fiber was wrapped around in two rotating wheels (diameter ~25cm). One of the two wheels is controlled by a rotational stage programmed by computer. The 3-D printed fiber mount and the two rotating wheel enables a roll-to-roll process. Thanks to this roll-to-roll process, the laser fabrication platform can potentially handle unlimited length of fibers.

One problem with interacting with standard fiber with laser written waveguide is low coupling efficiency. This is largely due to the mismatch propagation constants ($\beta$) between these two kinds of waveguides. Consider a directional coupler consists of two waveguides as in [56]. The power splitting ratios for couplers can be investigated as a function of interaction length $L$, and separation distance $d$ (center to center of waveguides). The power coupling ratio can be defined as:

$$r = \frac{P_2}{P_1 + P_2} = \frac{\kappa^2}{\delta^2}\sin^2(\delta L) \tag{4.3.1}$$

Where $\delta = \sqrt{(\beta_1 - \beta_2)^2 + \kappa^2}$. $\beta_{1,2}$ are the propagation constants of the two waveguides. $\kappa$ is the coupling coefficient, which increases exponentially with separation $d$.

To determine the coupling constant in waveguides, the calculated near-field output patterns can be fitted to the experiment data with the coupling constant as a varying parameter. However, because the coupling power ratio is determined by only two data points for a directional coupler, i.e., two output waveguide intensities, the accuracy is limited. This problem is solved by introducing not just two, but eleven or even more identical ultrafast laser written waveguides with a set of known laser processing parameters, one example is shown in Figure 4.3.2(c). To incorporate the coupling effects of the next nearest adjacent waveguides, BPM_Rsoft was used to calculate the near-field mode patterns (Figure 4.3.2(c)), which are subsequently fitted to the experiment output pattern (Figure 4.3.2(b)). The same data fitting process is repeated across a range of interaction length *L* and separation distance *d*. This further minimizes the margin of error for the propagation constant retrieved by this approach. It is worth noting that although it is possible to analytical solve the 11 coupled modes equation, it is very difficult to get an analytical solution if the coupling with the next nearest neighbors cannot be ignored. We utilized BPM numerical calculation due to accuracy because it also includes the coupling effect of all neighbor sites not just the nearest neighbor. Within a limited range, we mapped out the index contrast versus the writing laser beam parameters, as shown in Figure 4.3.5.

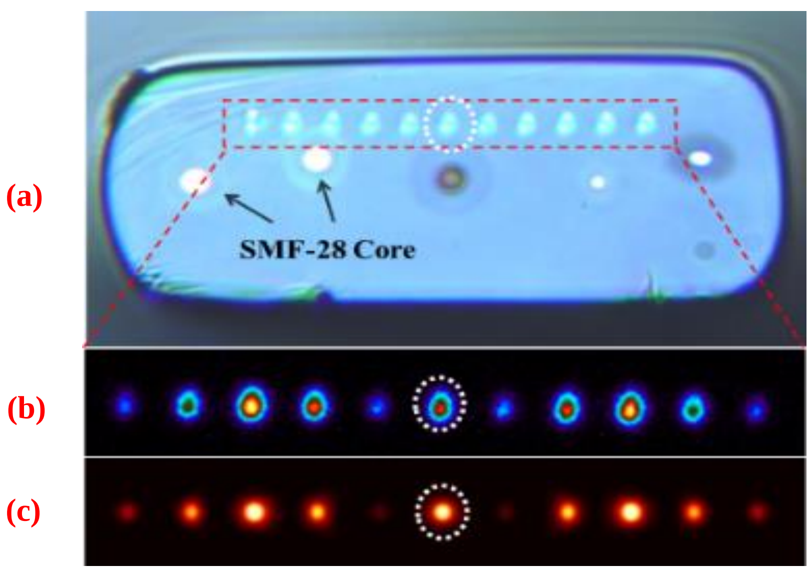


**Figure 4.3.2:** (a) Cross-section image of rectangular fiber with 11 ultrafast laser inscribed waveguides; (b) output mode pattern with 1550nm light input from the center waveguide, circled in white; (c) output mode pattern simulated using BPM_Rsoft.

As mentioned above, to fabricate waveguides that can effectively interact with as-fabricated fiber cores through evanescence coupling, the mode profiles and propagation constants of the ultrafast laser written waveguides needs to be carefully controlled and calibrated. Any mismatch between the propagation constants ($\beta$) will severely limit the coupling efficiency. Thanks to the flat geometry and large fiber cross-section, we were able to accurately calibrate and optimize the propagation constant $\beta_{wg}$ of the laser-fabricated waveguides. This was achieved by direct writing of 11 coupled waveguides in flat fiber at desired depth (Figure 4.3.2(a)). Light is injected into the center of waveguide array and the intensity distribution of near-field patterns at the output side is measured (Figure 4.3.2(b)). The calculated near-field output patterns (e.g. Figure 4.3.2(c)) are fitted to the measured data with the coupling constant as a varying parameter. As a result, we will be able to accurately determine the waveguide propagation constant $\beta_{wg}$ and correlate it with laser fabrication conditions. This will ensure precise match of waveguide propagation constant $\beta_{wg}$ and that of fiber core $\beta_{core}$.

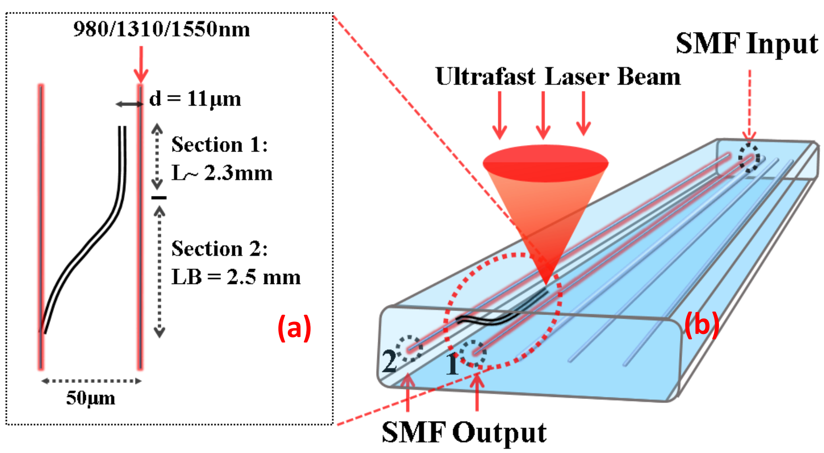


**Figure 4.3.3**. (a) Close-up top view of the design with two sections; (b) schematic sketch of integrated wavelength demultiplexer inside the rectangular fiber.

The schematic sketch of the couplers and WDM components to connected Core 1 and 2 (both are fiber cores) is shown in Figure 4.3.3(b) and its close-up view is shown in Figure 4.3.3(a). It can be divided into two sections. Section 1 is a directional coupler between the input SMF-28 core (core 1) and the fabricated waveguide (shown as a black double line). The separation between the center of the waveguide and that of the fiber core is *d*. The length of the coupling section L is tailored to suit various coupling ratios for both directional coupling and WDM applications. Section 2 is a waveguide combiner that delivers guided light directly into core 2.

In this part of the work, the desired index profile of the fabricated waveguide is fitted as $\Delta n \sim 0.00765$ (step index), with an elliptical shape ~ 4.9 μm × 6.2 μm (horizontal width × vertical width). This corresponds to on target laser pulse energy ~800 nJ, and 1 mm/s writing speed. The index profile of the two SMF-28 core is known as $\Delta n \sim 0.00524$ (step index), with a circular shape ~ 8.2 μm × 8.2 μm. Even though the waveguide and the SMF-28 core have different index contrast ($\Delta n$), the effective index is close (less than 0.0001 from Rsoft calculation) due to a smaller index profile area.

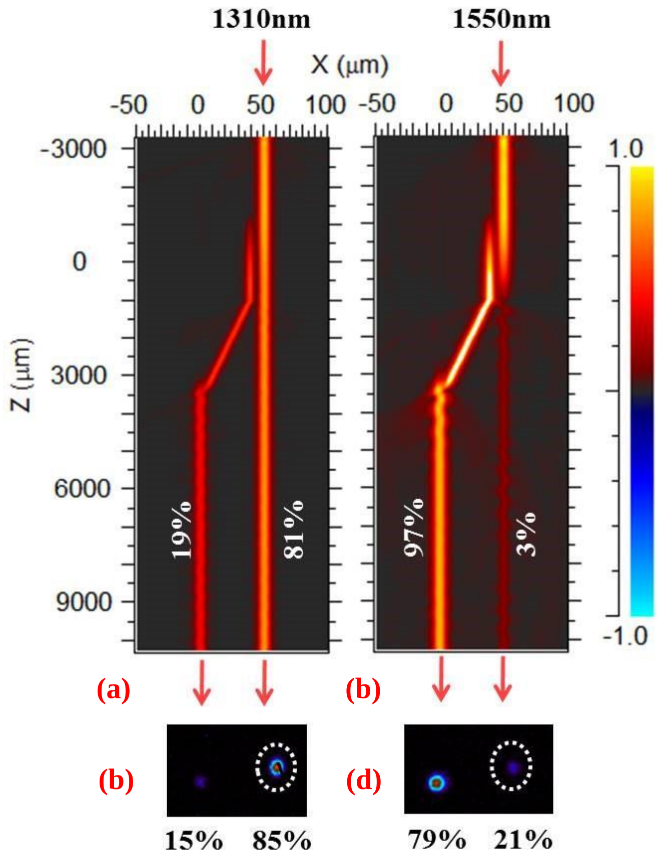


**Figure 4.3.4.** (a) and (b): Top view of the WDM by Rsoft_BPM simulation at 1310 nm and 1550 nm, injected cores circled in white; (c) and (d) output mode pattern.

Figure 4.3.4 shows both calculated and experimental results of a 1310/1550 nm WDM coupler that can separate 1310 nm and 1550 nm light into two fiber cores. For section 1, with L ~ 2.3 mm, *d* = 11 μm, BPM_Rsoft result predicts that these index profiles will result in 95% coupling at 1550nm, but only 14% for 1310nm. These are verified on the fiber separately before going to fabricating the whole section (section1 + section2). The 1310/1550 nm cross-talk can be further improved by increasing core-to-core separation *d*. with L needing to increase exponentially.

To characterize the performance of this WDM, two laser sources (1310 nm and 1550nm) were butt-coupled to core 1. The mode field patterns at the output ports were imaged by an GaInAs IR camera (ICI). The insertion loss caused by the directional coupler, which was obtained by summing the intensities of two outputs from both fiber cores, was measured as ~ 0.5 dB. Part of the insertion loss is due to the propagation loss of laser written waveguides in fused silica, which is ~ 0.2 - 0.4 dB/cm [59]. The performance of the WDM device for 1310 nm and 1550 nm wavelength splits is shown in Figure 4.3.4(c) and (d). Using the device, BPM simulations (shown in Figure 4.3.4(a) and (b)) yield 81% to 19% splitting of 1310 nm and 3% and 97% splitting of 1550 nm light into Core 1 and Core 2 respectively. This is consistent with the experimental results (Figure 4.3.4(c) and (d)).

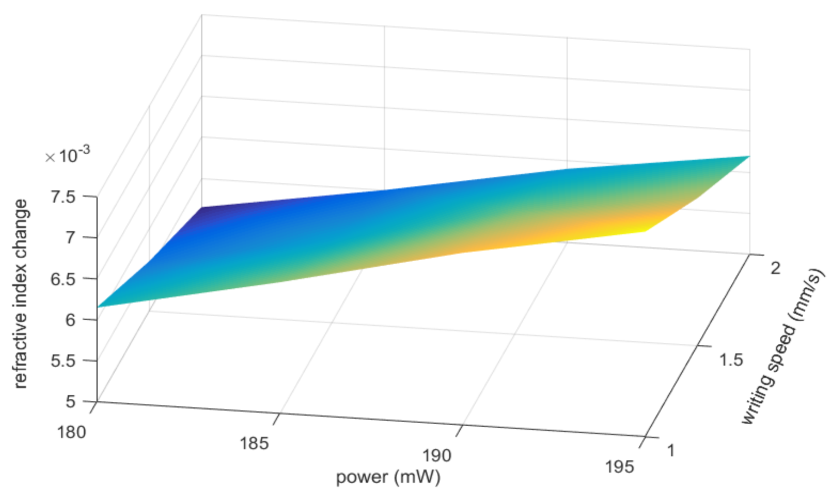


**Figure 4.3.5.** Index contrast versus the writing laser beam parameters.

## 4.4 3-D INTERGRATED WAVEGUIDE COUPLER FOR CLADDING-PUMPED RARE EARTH-DIOED MULTICORE FIBER AMPLIFIER

A cladding-pumping fiber applies a double-cladding geometry, where all cores are embedded in a common inner cladding, then into polymer coating. Two schemes have been used for pump light coupling in cladding-pumping fiber. In end-pumping, both pump light and signal light are coupled from the end facet of the fiber. In comparison, side-pumping injects light into inner cladding through sides of the fiber, an advantage of which is the core signal uninterrupted [55]. Side-pumping has been accomplished by V-grooves [60], embedded mirrors [61], downsized capillaries [62], down-tapered coreless fibers [55]. However, for higher pump efficiency, an unsymmetrical shape of the pump region is preferred, where the overlap integral of the mode field of the signal and pump light is maximized [63]. Moreover, the distribution of the fiber cores should be designed as compact as possible, it is hard for the above-mentioned coupling schemes to accommodate for the changes in spatial channel geometry.

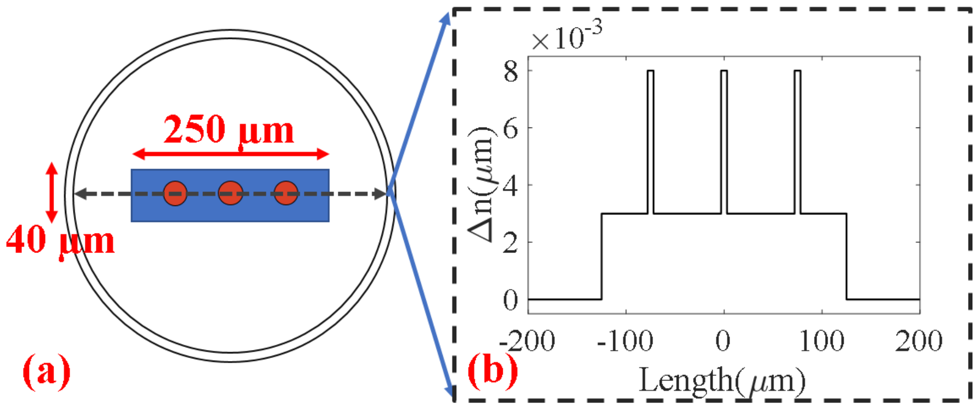


**Figure 4.4.1.** (a) Schematic of a proposed cladding-pump fiber amplifier; (b) Desired index profile

Laser induced 3-D waveguide has been used to fabricate compact spatial multiplexer, known as photonic lantern, for few mode fiber SDM with low loss [64]. The ultrafast laser writing technique has demonstrated flexibility of modifying the shape of the impacted region and adjusting the index change in transparent bulk material. In this section, we demonstrate a novel integrated cladding-pump fiber amplifier coupler fabricated in bulk fused silica, using ultrafast laser direct writing, for a designed cladding-pump fiber shown in Figure 4.4.1. The waveguide allows simultaneously coupling of signal light into three coupled multicores, and transmission of light from a multimode laser diode.

The schematic sketch for the integrated coupler is shown in Figure 4.4.2(c). Fused silica with the length of 25 mm and thickness of 1 mm is used. Two sections were written on the bulk fused silica. One is a rectangular region with lower index of $\Delta n = 3 \times 10^{-3}$ compared to the bulk fused silica for the insertion of pump light from a laser diode pump. And the other section includes three waveguides with a higher index of $\Delta n = 8 \times 10^{-3}$ for the delivery of signal light to the multicores EDFA. The curves of these waveguides were designed with simulation so that no extra loss will be induced due to bending curvature in 3-D space. The parameters for generating both index changes on fused silica were found from the calibration process discussed in part B.

First, the pumping waveguide region is written with 760 nJ per pulse. The size of the single spot beam was measured so that a layer-to-layer transversal scanning scheme is used. The speed of the motion stage is set to be 10 mm/s. Afterwards, three waveguides for each core are written on top of the rectangular shaped pumping waveguide, with 810 nJ per pulse, 1 mm/s speed.

Figure 4.4.2(a) and (b) show the end surface of both sides images under the microscope. Center of the waveguide is 100 μm below the surface of the glass. Spacing between the three signal waveguides at the input side are set to 75 μm. At the input side, the waveguides for signal light delivery are 100 μm below the pump waveguide region, and then merge into the pump waveguide along a designed trace.

To measure the light transmission of bulk coupler, the pump region was measured with a laser diode. The result is shown in Figure 4.4.2(e). The signal waveguides were measured with both 1550 nm and 1310 nm light sources, using butt-coupling with three single-mode fibers simultaneously. Three different signals with different intensities were used to test the transmission. The mode pattern of 1550 nm light at the end surface is shown in Figure 4.4.2(d). Single-mode propagation behavior was observed the waveguide.

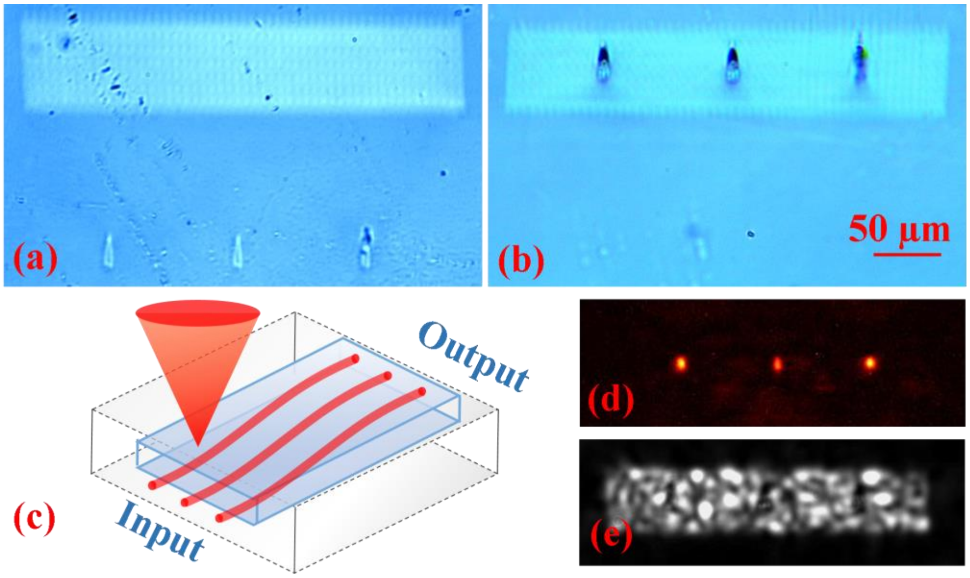


**Figure 4.4.2.** (a) Microsopic image of the input facet of the fused silica coupler; (b) output facet of the coupler; (c) schematic sketch of the coupler; (d) output mode pattern of 1550 nm light; (e) output mode pattern of 650 nm laser diode light.

3-D waveguide coupler has demonstrated the feasibility of simultaneous coupling of the pump light and signal light into a customized designed cladding-pump fiber. The geometric flexibility of ultrafast laser writing allows easy separation between the different distribution of the transmission fiber cores and the cladding-pump EDFA cores, as well as the shape of the multimode diode pump and the inner cladding region. This provides more degrees of freedom in the cladding-pump EDFA geometric design, for both arranging the core position and the inner cladding shape. Since an optimized cladding-pump EDFA does not have necessarily have symmetrical cross-sections, for higher efficiency in pump coupling, our method can accomplish higher power efficiency than ordinary methods of side pumping. Also, calibration of the ultrafast laser writing induced index change allows better index matching for multicore and inner cladding, and thus contribute to minimal insertion loss.

# 5.0 ULTRAFAST-LASER FABRICATION OF PHOTONIC GRAPHENE AND CROSS-TALK MANAGEMENT APPLICATIONS

So far in this dissertation, we have demonstrated optical interconnect applications based on our Ultrafast laser fabrication platform. In this following section, we show that the very same Ultrafast laser fabrication platform is also a very powerful tool to study fundamental physics. In particular, we focus on fully utilizing the refractive index engineering capability discussed in section 4, in an effort to construct a graphene lattice-like structure in optics. What used to be photonic circuits formed by only a few waveguides have now been expanded into 3-D evanescently coupled waveguide arrays in a much larger scale. It turns out that this unique photonic graphene structure gives us a great opportunity to study complex graphene physics phenomenon. The work in this section is in collaboration with Mikael Retchsman's group from Department of Physics, Penn State University. Later on, we will discuss the reasons of using photonic graphene as a probe to observe various graphene physics phenomenon, versus observing on a traditional carbon atomic graphene. Finally, the study of photonic graphene leads to our development of a cross-talk management solution for optical interconnect, which will be covered at last in this section.

## 5.1 INTRODUTION TO COUPLED WAVEGUIDE ARRAYS AND PHOTONIC GRAPHENE

Much like what is discussed in section 4, where we emphasized on the importance of fine-tuning the effective refractive index profile of each laser-written waveguide, here we apply the same idea to a much more complex 3-D evanescently coupled waveguide array structure. Figure 5.1.1 shows an example of how one single waveguide is expanded to form a linear array, and then the subsequent linear array is expanded again to form a 3-D coupled waveguide array.

So what is photonic graphene? By definition, photonic graphene is an array of evanescently coupled waveguides. These waveguides are arranged in a honeycomb-lattice configuration, the same configuration as a typical graphene, as shown in Figure 5.1.2(a)-(b) [65]. The difference in photonic graphene is that the wave-function is actually also described by a Schrödinger equation, but the z axis now acts as the 'time'. This is evident by the envelop approximation for electric field, and paraxial Schrödinger equation, as shown in Eq. (5.1.1-5.1.3). The waveguides act like potential wells, similarly to nuclei of atoms in solids.

$$\mathbf{E}(x,y,z) = \hat{x}\psi(x,y,z)e^{i(k_0 z - \omega t)} \tag{5.1.1}$$

$$|\partial_z^2 \psi| \ll 2k|\partial_z \psi| \tag{5.1.2}$$

$$i\partial_z \psi = -\frac{1}{2k}\nabla^2\psi - \frac{k}{n_0}\Delta n(x,y,\mathbf{z})\psi \tag{5.1.3}$$

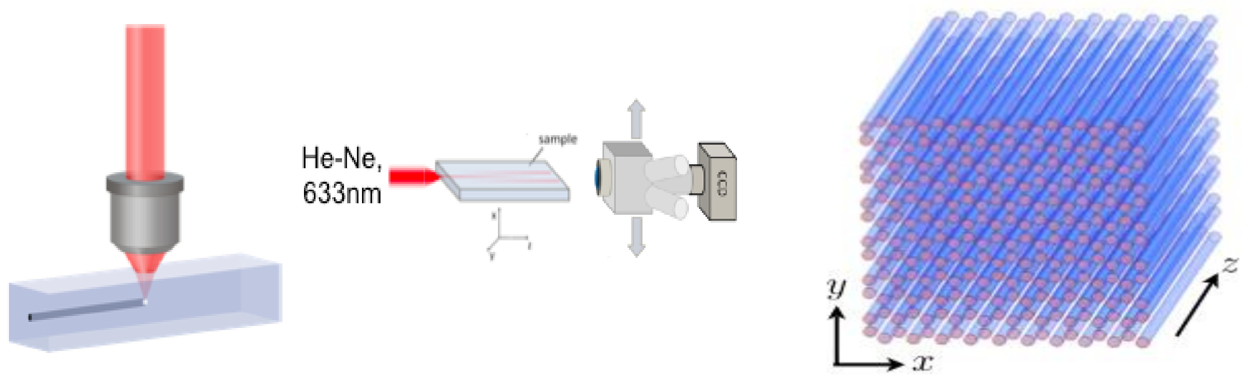


**Figure 5.1.1** A demonstration of how a single waveguide can be expanded to form a honeycomb waveguide lattice: Photonic Graphene

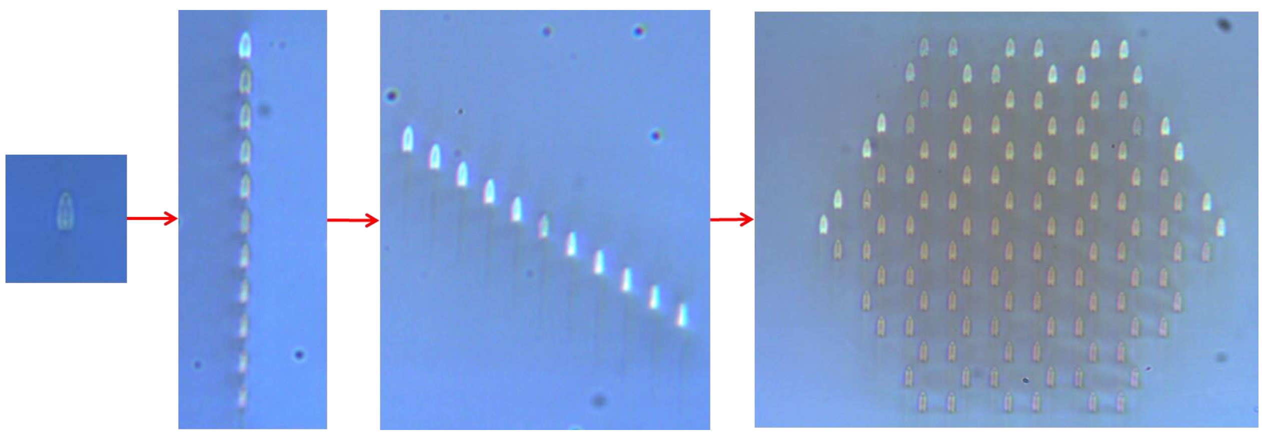

**Figure 5.1.2** An illustration of a honeycomb waveguide lattice: Photonic Graphene

As shown in the animation sequence from Figure 5.1.3, the propagation of light is actually equivalent to the temporal evolution of an electron inside a 2-D atomic lattice. With the help of proper band structure design, many other physical quantities of the system can be extracted from final output image patterns. It is therefore a very useful structure to study graphene physics.

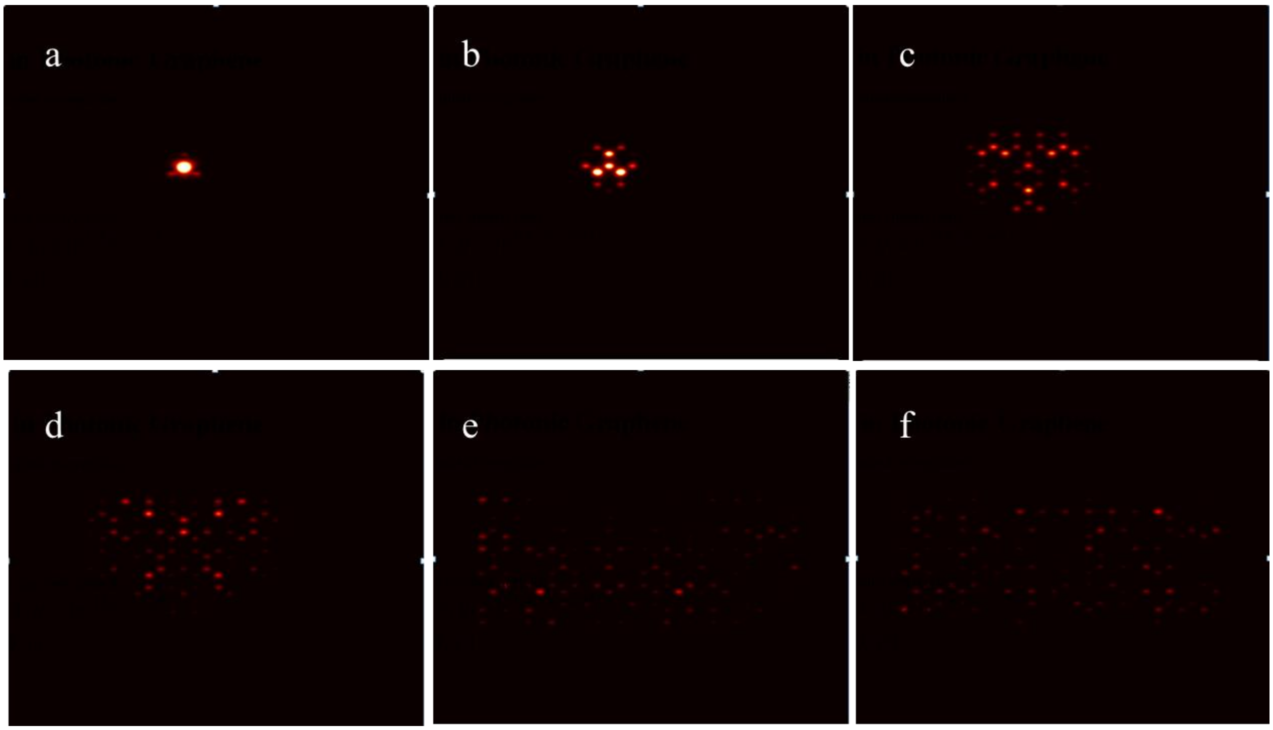


**Figure 5.1.3** A BPM animation of the temporal evolution of an ‘electron’ inside a 2-D atomic lattice, at time (a) t = 0. (b) t = 0.024T. (c) t = 0.056T. (d) t = 0.10T. (e) t = 0.32T. (f) t = 0.96T.

For all the following photonic graphene structures mentioned in sections 5.1 through 5.4, the waveguides are written in Corning Eagle XG borosilicate glass, refractive index $n_o$ = 1.473. We employed the same Titanium:Sapphire laser and amplifier system (Coherent:RegA 9000) with pulse duration 270 fs, repetition rate 250 kHz, and pulse energy 950 nJ. The laser writing beam was again sent through a beam-shaping cylindrical telescope to control the shape and size of the focal volume. The beam was then focused inside the glass chip using a ×80 or ×50, aberration-corrected microscope objective (NA = 0.75, 0.55, respectively). The same high-precision three-axis Aerotech motion stage (model ABL20020) is used to translate the sample during fabrication.

Of course, as each individual waveguide acts as potential well for ‘electrons’, it is very important to carefully control the effective refractive index of each waveguide in the array. In the last part of section 6 conclusion and future works, we will introduce a refractive index profile calibration process, which is still an ongoing effort. This process involves a combination of numerical simulation and a large experimental data set. Depending on the dimension of the 3-D waveguide array, it is often necessary to introduce a depth index profile correction. This is because the aberration of the laser focal point becomes more severe at larger depth into the glass material, leading to a refractive index chirp [66].

Using the calibration and correction method, it is determined that the index profiles in all of the photonic graphene mentioned in this section can be best described in Eq. (5.1.4) as:

$$\Delta n(x,y) = \delta n \exp(-x^2/\sigma_x{}^2 - y^2/\sigma_y{}^2) \tag{5.1.4}$$

Where $\delta n = 2.8 \times 10^{-3}$, $\sigma_x = 3.50$ μm and $\sigma_y = 5.35$ μm. $\sigma_x$ and $\sigma_y$ are half diameter along horizontal and vertical direction, respectively

## 5.2 CONICAL DIFFRACTION: EXPERIMENTAL OBSERVATION OF OPTICAL WEYL POINTS AND FERMI ARC-LIKE SURFACE STATES

Recently, there has been tremendous theoretical and experimental effort towards the realization of Weyl points both in electronic band structures in condensed matter and in photonic band structures in complex three-dimensional dielectric structures. In our very first photonic graphene project, the goal is to find the Weyl point in the band structure. In order to find it, we need to start by adding a helical path into our system, as shown in Figure 5.2.1(a) [67]. It shows a schematic diagram of the 3-D waveguide lattice written by the Ultrafast laser platform. Blue and green indicates each sub-lattice, lattice A and lattice B, respectively. Each waveguide in both sub-lattice shares a same set of parameters: Z, the helix period, fixed at 10000 μm; a is the lattice constant, varying from 25 μm to 29 μm; R is the radius of the helical path, fixed at 4 μm. Notice that although it looks like the two sub-lattices A and B are rotating towards different directions, in fact they only differ in phase (PI phase shift) and they have the same chirality. The addition of helix is equivalent to adding a synthetic gauge field into the whole system. This is only possible due to the freedom we have on each individual waveguide of a whole 3-D waveguide array lattice, as previously emphasized on section 4.

Therefore, by engineering the waveguide lattice at will, we can do two most important modifications to the photonic lattice. The first one is that we can engineer the band structure and the band gap. The second one is that we can control the energy of the modes injected into the system. This is also called controlling the initial condition or controlling the initial source. In our waveguide array lattice, this is simply achieved by extending a single waveguide leading to the target waveguide/waveguides (the initial condition). It is worth noting that unlike what is shown in the animation sequence in Figure 5.1.3, the initial condition (shown in Figure 5.1.3(a)) need not be only a single waveguide (a single mode). It is entirely possible to have multiple waveguides (multi-mode) injected into the same system at the same time (see section 5.4), or with a carefully designed time delay. If that is the case, a carefully tested waveguide splitter will be used, where the initial light would first be guided in the single waveguide, and then adiabatically split into multiple waveguides at a certain ratio by design.

Figure 5.2.2(a) shows a microscope image of a cross-sectional cut of the waveguide array structure we made.  Figure 5.2.2(b) and (c) is its corresponding phase diagram, and the band structure, respectively. All results in Figure 5.2.2(b)–(f) are calculated numerically, using experimental parameters, as obtained by the method described in end of section 5.1.

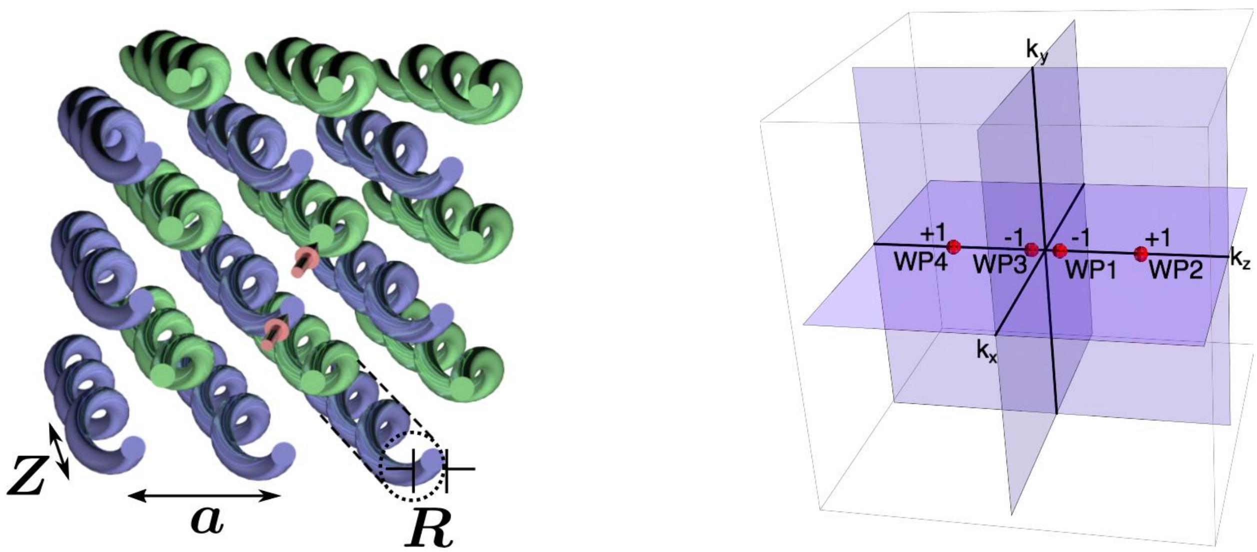


**Figure 5.2.1:** (a) Schematic diagram of the waveguide array structure, composed of two interpenetrating square lattices of helical waveguides, with the two sub-lattices out of phase from one another by a half-cycle. (b) Position of the four type-II Weyl points in the 3-D cubic Brillouin zone (represented by the enclosing box)

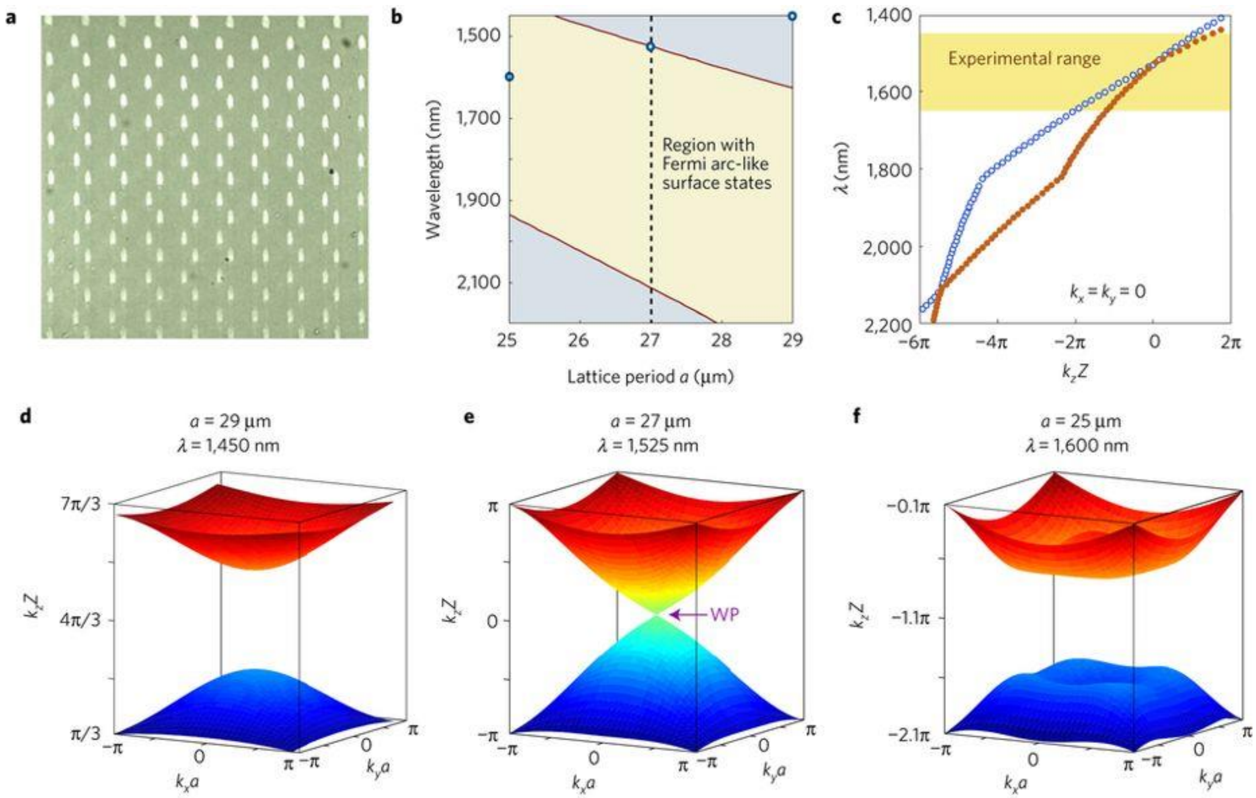


**Figure 5.2.2:** Theoretical and numerical demonstration of topological phase transition associated with type-II Weyl points: **a**, Microscope image of the output facet of structure, representing a two-dimensional cut of the waveguide array for fixed z. **b**, Numerically determined phase diagram of the structure, as a function of lattice constant a and wavelength λ. Type-II Weyl points reside along the red curves, and Fermi arc-like surface states exist between these two curves (yellow region). **c**, Bulk band structure for the two relevant bands plotted as a function of kz (in the kx = ky = 0–plane, using the extended-zone scheme). Type-II Weyl points arise at their intersection. **d**–**f**, Isofrequency surfaces for the topologically trivial case (no Fermi arc-like states), at the Weyl point (WP), and the topological (with Fermi arc-like states) case, at a = 29,27 and 25 μm, at wavelengths 1,450 nm, 1,525 nm and 1,600 nm, respectively. The open circles in the phase diagram shown in **b** correspond to the band structures in **d**–**f**. All results in **b–f** are calculated numerically, using experimental parameters.

According to the theoretical prediction [67], in our experiment, the first evidence of Weyl point can be found by setting the initial condition for the input to be at the center of the array, as indicated in Figure 5.2.2(a). We will then need to find the corresponding conical diffraction pattern at this input.

The detail of the measurement setup is very similar to the one used in section 3 and section 4. The measurements at the output are performed by butt-coupling a single-mode optical fiber to waveguides at the input facet of the chip, which subsequently couples to the waveguide array. The input light is supplied by a tunable mid-infrared diode laser (Agilent 8164B), which can be tuned through the 1,450 – 1,650 nm wavelength range. After a total propagation distance of 4 cm within the array, the light output from the waveguide array is observed using a 0.2 NA microscope objective lens and a near-infrared InGaAs camera (ICI systems).

We perform the conical diffraction experiment by injecting light into a single waveguide at the input facet, which then couples through a waveguide splitter to a pair of neighbouring waveguides (within one unit cell at the centre of the lattice) with equal intensity and phase. The in-coupling region occupies the first 1 cm of the chip. The resulting diffraction patterns, imaged at the end of the chip, are shown in Figure 5.2.3(b)–(d). For lattice constants a = 29 μm (at wavelength 1,450 nm, Figure 5.2.3(b)) and a = 25 μm (at wavelength 1,600 nm, Figure 5.2.3(d)), we observe a filled-in disc-like diffraction pattern, which is characteristic of parabolic dispersion. When the lattice constant is tuned to a = 27 μm, we observe a clear ring-like conical diffraction pattern at $\lambda$ = 1,525 nm, shown in Figure 5.2.3(c). Thus, the presence of conical diffraction clearly establishes the presence of the Weyl point.

To quantify the observation of conical diffraction, we define a dimensionless parameter that measures the degree to which the diffraction pattern is conical:

$$C = \frac{\int \mathrm{d}\mathbf{r}\, r^2 \, |\psi(\mathbf{r})|^2}{\left(\int \mathrm{d}\mathbf{r}\, r \, |\psi(\mathbf{r})|^2\right)^2} \tag{5.2.1}$$

where $\mathbf{r} = (x, y)$ and $r = (x^2 + y^2)^{1/2}$ is the distance from the origin (the origin is defined to be the centre point between the two excited waveguides). The quantity C measures how 'ring-like' a wavefunction is, and is reminiscent of the inertial moment of a rotating body in a mechanical system (but is dimensionless in this case). It takes the value 1 for an infinitely thin ring, and is larger than 1 for all other patterns. The monotonic behaviour of Figure 5.2.3(h) and (j) shows that for lattice constants a = 29 μm and 25 μm the Weyl point does not occur within the wavelength range of the tunable laser (1,450–1,650 nm), or is very near the boundary. That said, the Weyl points do exist within the spectrum for each value of a described here. The minimum in C observed in Figure 5.2.3(i) corresponds to conical diffraction (see Figure 5.2.3(c) and (f) for experimental and numerically computed conical diffraction patterns). The conical diffraction associated with the isofrequency surface provides direct evidence of the existence of the type-II Weyl point [67].

From an optical engineer's point of view, we can see that after incorporating waveguide index profile calibration and correction method, the experimental results are almost identical with simulation results, as evident by Figure 5.2.3(b)-(g), where Figure 5.2.3(e)–(g) shows full-wave beam-propagation simulations, which agree strongly with the experimental results of Figure 5.2.3(b)–(d).

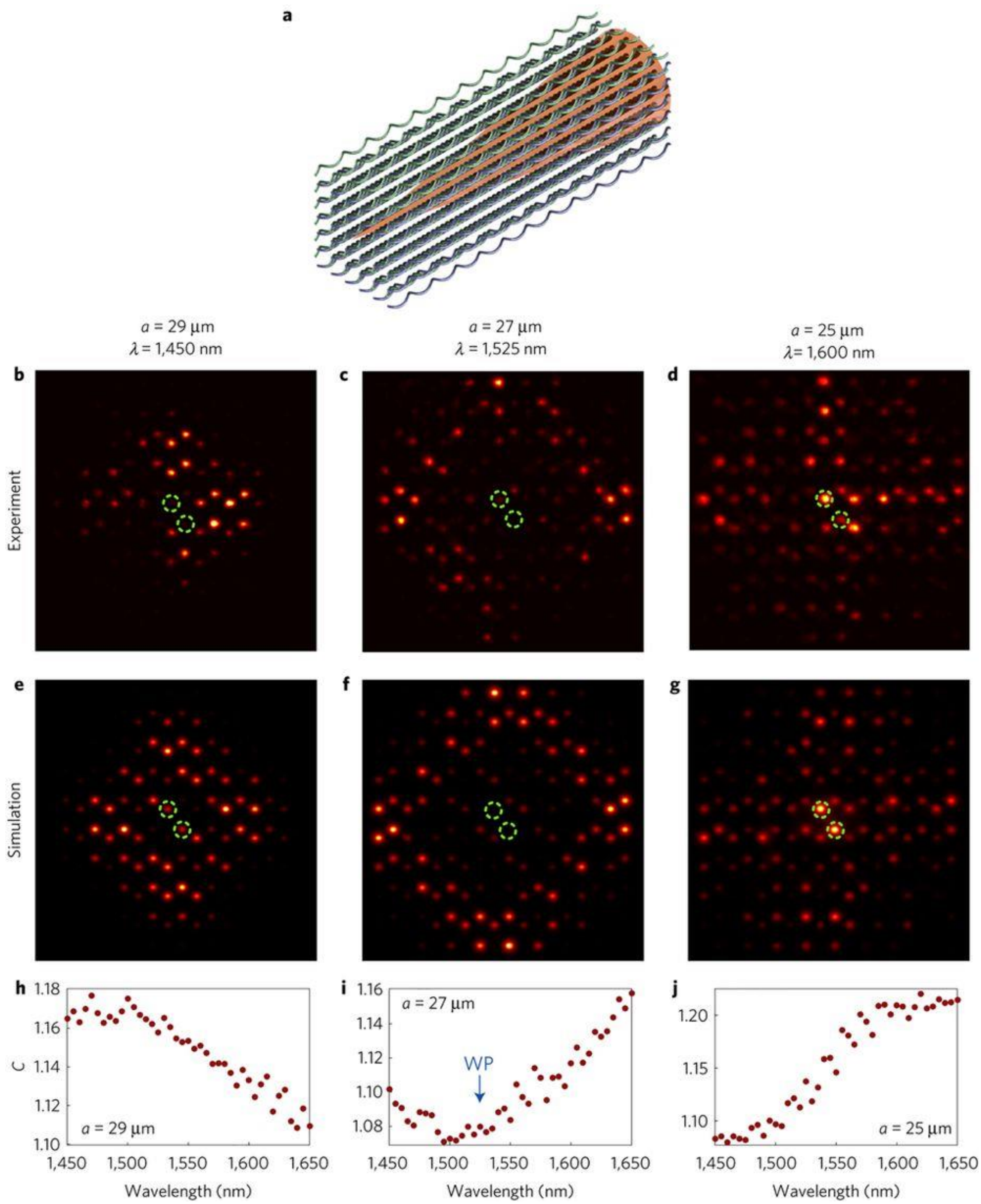


**Figure 5.2.3: Conical diffraction as a signature of the existence of type-II Weyl points : a**, Schematic diagram of conical diffraction occurring in the waveguide array at a type-II Weyl point. **b**–**d**, Intensity plots at the output facet, as we sweep through the Weyl point, at $a$ = 29,27 and 25 μm, and wavelengths 1,450 nm, 1,525 nm and 1,600 nm, respectively. The green circles indicate the position of the input waveguides. Clear conical diffraction is observed in **c**, at the Weyl point. **e**–**g**, Full-wave simulations corresponding to the parameters of **b**–**d**. **h**–**j**, Plot of the quantity $C$, obtained from experimental data, as a function of $\lambda$, which quantifies how ring-like the wavefunction for $a$ = 29,27,25 μm, as a function of wavelength from 1,450–1,650 nm. In **h** and **j**, there is no clear minimum, indicating the lack of a Weyl point within this wavelength range. However, **i** shows a clear minimum, at the wavelength where the Weyl point lies. This minimum corresponds to the wavefunction shown in **c** and **f**.

Next, we aim to find the second evidence of the Weyl point, that is, to demonstrate the existence of the Fermi arc-like surface states. To probe for surface states, we simply change the beam excitation location, thereby changing the initial condition of the wavepacket. In the experiment, we inject light via a single waveguide at the top of the lattice and observe the output facet. If a surface state is present, light should stay confined to the surface (see schematic depiction in Figure 5.2.4(a)); otherwise it should diffract into the bulk of the structure.

Figure 5.2.4(d)–(h) shows the output wavepacket at wavelength 1,550 nm, with decreasing lattice constant from left to right. Changing the lattice constant a simply shifts the wavelength at which the Weyl point occurs (larger a means it occurs at longer wavelength $\lambda$, or smaller frequency). Figure 5.2.4(d), e shows that deep in the $\delta\omega > 0$ regime (a = 29,28 μm), the input light spreads into the bulk, indicating the absence of surface states. By contrast, Figure 5.2.4(g), (h) shows that deep in the $\delta\omega < 0$ regime (a = 26,25 μm), most of the light stays confined to the top and proceeds in a clockwise sense; this indicates the existence of surface states. Of course, some of the light is still coupled to bulk modes, which are present at every frequency; but the deeper we go into the $\delta\omega < 0$ regime, the stronger the surface state overlap, as shown in Figure 5.2.4(h). Full-wave beam-propagation simulations that correspond to the cases shown in Figure 5.2.4(d)–(h) are shown in Figure 5.2.4i–m. Corresponding isofrequency surfaces are shown in Figure 5.2.4(n)–(r); these clearly show that states confined to opposite surfaces, top and bottom (marked in red and blue), emerge for $\delta\omega < 0$, exactly as expected for the type-II Weyl points.

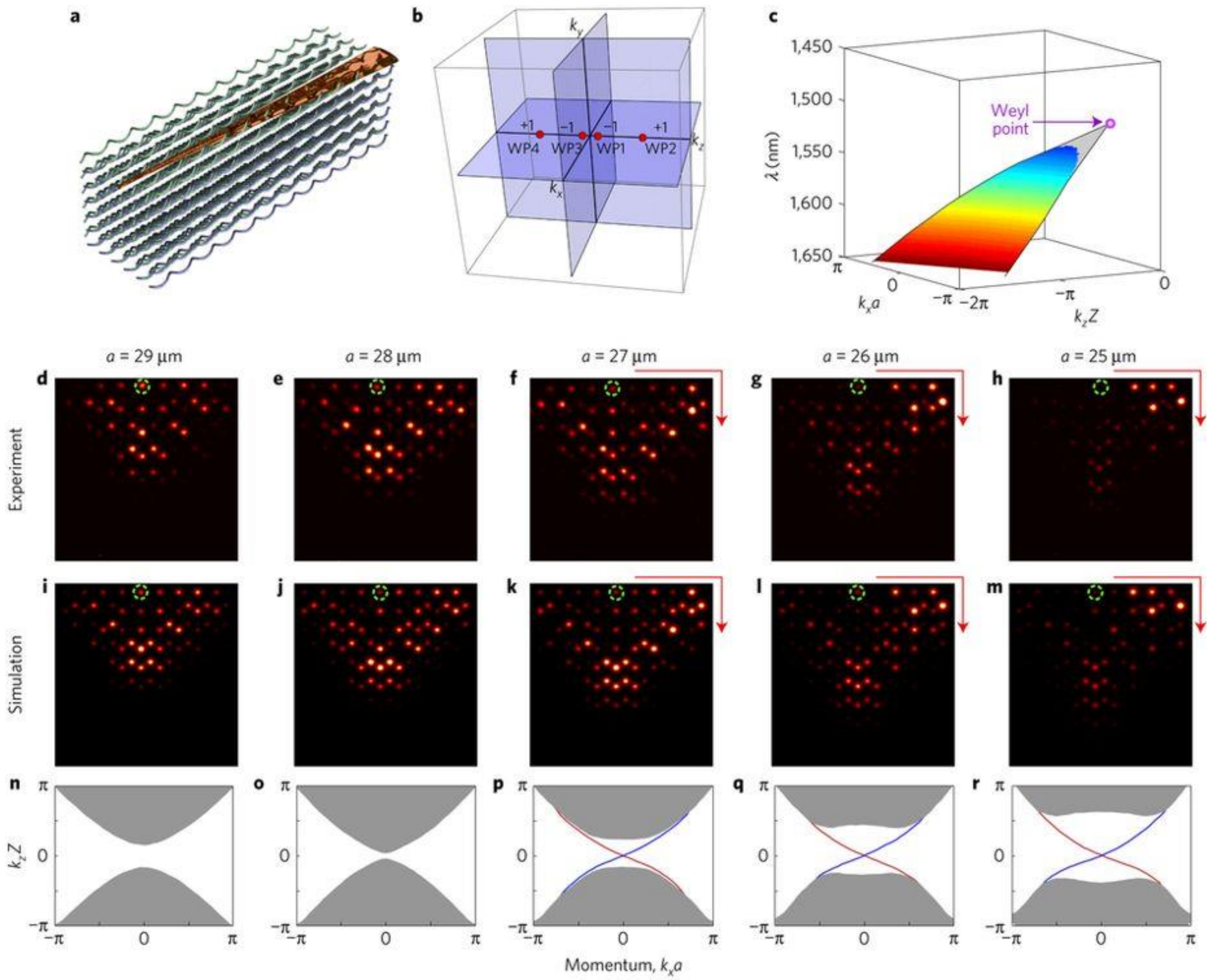


**Figure 5.2.4 : Direct observation of Fermi arc-like surface states**: **a**, Schematic diagram of light confinement to the surface as a result of a Fermi arc-like surface state. **b**, Position of the four type-II Weyl points in the 3-D cubic Brillouin zone (represented by the enclosing box), with their topological charges indicated. WP1 and WP2 are partner Weyl points, and WP3 and WP4 are their time-reversed equivalents (exact values of **k** in text). **c**, Plot of the Fermi arc-like dispersion relation in the surface Brillouin zone, within the range of experimentally accessible wavelengths, as a function of kx and kz (the surface is terminated in the y-direction). This is calculated using the method of ref. 28. **d–h**, Output intensity plots, when light is input at the centre of the top surface of the structure (indicated by green circles) at wavelength 1,550 nm, for decreasing a = 29,28,27,26,25 μm. For decreasing lattice constant a, increased confinement to the surface indicates the formation and presence of Fermi arc-like surface states. **i–m**, Corresponding full-wave beam propagations, showing strong agreement with experimental results. **n–r**, Numerically calculated isofrequency contours, showing the presence of surface states forming at a = 27 μm as the Weyl point is crossed. The red and blue curves indicate surface states on the top and bottom of the sample, respectively. The trajectories of the surface state wavepackets are indicated by red arrows.

The aforementioned two observations (conical diffraction and Fermi arc-like surface states) are direct indications of Weyl points at optical frequencies. The observation of Weyl points in optics is not only a very interesting discovery in graphene physics, but can also lead to a range of novel phenomena arising from the interplay of the Weyl dispersion and nonlinear, non-Hermitian, and quantum optics [68-71].

Here we need to emphasize that even though our design of the waveguide lattice structure is very complex, having two sets of helical sub-lattices with a PI phase shift, the simulation and experimental result is again a very close match. This is another demonstration of the high quality of the waveguides we fabricated using our Ultrafast Laser processing platform. In addition, we are able to sweep through the Weyl point either by changing the wavelength of the input beam or by changing the lattice constant of the structure. But more importantly, the point of this part of the work is to show that this particular lattice design is just one of the many examples. By designing different exotic configurations at our will, we can observe and study additional physics aspects. This would greatly help us in better understanding the carbon atomic graphene physics. As mentioned earlier, lots of these physics would be otherwise impossible or very hard to observe.

## 5.3 EXPERIMENTAL REALIZATION OF A WEYL EXCEPTIONAL RING AND PHOTONIC TOPOLOGICAL BOUNDARY PUMPING

As an extension of the work (Weyl point) described in section 5.2, the work presented here is another perfect example of why Ultrafast Laser processing platform is a very power tool to study exotic graphene physics. In the first part of this section (section 5.3), we notice that unlike electronic systems, an important feature of photonic systems is their ability to break Hermiticity through material gain or absorption, as well as radiative outcoupling. This enables photonic systems to realize phenomena exclusive to non-Hermitian systems, such as exceptional points. Here we experimentally observe a WER (Weyl Exceptional Ring) in a 3-D photonic lattice consisting of evanescently coupled single-mode helical waveguides, with only a small modification from the work in section 5.2: to remove the Hermiticity of that system, we insert breaks into half of the helical waveguides (only sub-lattice B), by periodically skipping the writing of a specified length of these waveguides, as shown in Figs.5.3.1(a)-(c). Within these breaks the confining potential for the light is removed, resulting in strong coupling to radiating modes and yielding a tunable mechanism for adding loss by increasing the length of these breaks.

Here, we use $\tau$ to characterize the strength of the loss added to sub-lattices B. In the Hermitian limit, $\tau = 0$, this helical waveguide array possesses a type-II Weyl point, as same in section 5.2. The distinctive conical band structure of this system at the Weyl point, $\delta\omega = 0$, is shown in Figs. 5.3.1(d)-(e). However, as loss is added to one sub-lattice (sub-lattice B) in the bi-partite waveguide array by increasing the break lengths, $|\tau| > 0$, the two bands begin to merge together starting at the Weyl point, and proceeding radially outward in the transverse direction, as shown in Figure 5.3.1(f).

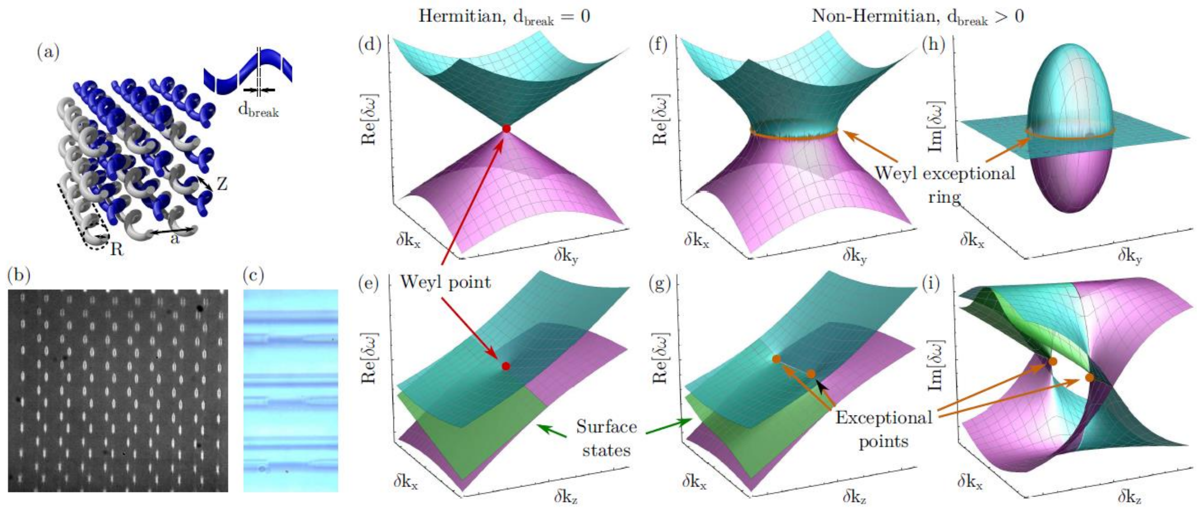


**Figure. 5.3.1. Helical waveguide array and corresponding band structure supporting a Weyl exceptional ring.** (a) Schematic of the bipartite helical waveguide array in which the rotations of the two sublattices are out of phase by a half-cycle and breaks have been added to one of the sublattices. (b) Grayscale microscope image of the output facet of one of the helical waveguide arrays. (c) Microscope image showing breaks added to the top layer of a helical waveguide array. Within the breaks, out of focus waveguides deeper in the array can be seen. (d)-(e) Band structures in the δkxδky and δkxδkz planes with δky = 0 and δkz = 0, respectively, for a Hermitian waveguide array, $\tau = 0$, showing a Type-II Weyl point. (f)-(g) Similar to (d)-(e), except with breaks added to the waveguides, $\tau = 0.2$, so that the band structure possesses a Weyl exceptional ring in the δkxδky plane which is intersected twice by the δkxδkz plane, exhibiting two exceptional points. (h)-(i) Imaginary portion of the band structure for the same systems considered in (d)-(e). Surface states are shown schematically in (e), (g), and (i) for the states localized to the surface with unbroken waveguides.

For the specific design of this new modified system, it is very much like the one used in section 5.2. As shown in Figure5.3.1(b), a microscope image of a cross-sectional cut of the waveguide array at the output facet shows an identical waveguide lattice structure. What is new is that 16 evenly-distributed breaks with length $d_{break}$ are added to only one of the two waveguides per unit cell, dramatically increasing its coupling to radiating modes, and resulting in an effective on-site loss in those waveguides, see Figure 5.3.4. The waveguide breaks are formed by turning off the laser writing beam using AOM (acoustic optical modulator, to ensure fast on/off operation) while the motion stage continues to move, and then turning the beam back on after the desired distance is reached. A microscope image (top view) of an array of isolated waveguides possessing breaks of different lengths is shown in Figure 5.3.1(c).

Using different choices of inputs, we are able to observe three distinct behaviors associated with a WER. First, we demonstrate that our system exhibits a topological transition by observing the appearance of Fermi arc states for increasing $d_{break}$. Second, we note that as $d_{break}$ is increased, a signal injected into the center of the waveguide array at the topological transition experiences progressively more localization, as evident by Figure 5.3.2 and Figure 5.3.3. For detail analysis in the perspective of physics, please see [72].

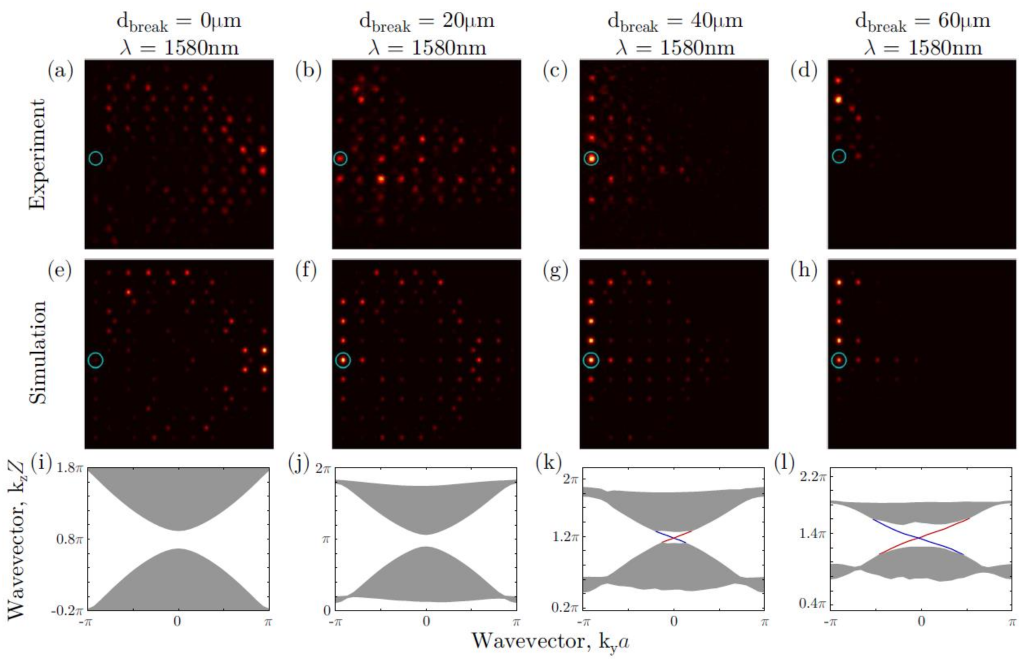


**Figure 5.3.2. Direct observation of a topological transition through the emergence of Fermi arc surface states**. (a)-(d) Output intensity plots when light is injected in to a single waveguide at the bottom of the lattice, indicated by cyan circle, with a total system length of L = 8cm, at λ = 1580nm, for four different break lengths, dbreak = 0,20,40,60μm. This drives the system through a topological transition, and a Fermi arc state is seen in (d). (e)-(h) Corresponding full-wave simulation results calculated using the beam propagation method, showing good agreement with the experimental results. (i)-(l) Isofrequency contours of a semi-infinite helical waveguide array calculated using full wave simulations and a diagonalization procedure [68]. Blue and red curves indicate surface states traveling on the top and bottom of the device, respectively, while gray indicates the regions of the bulk bands.

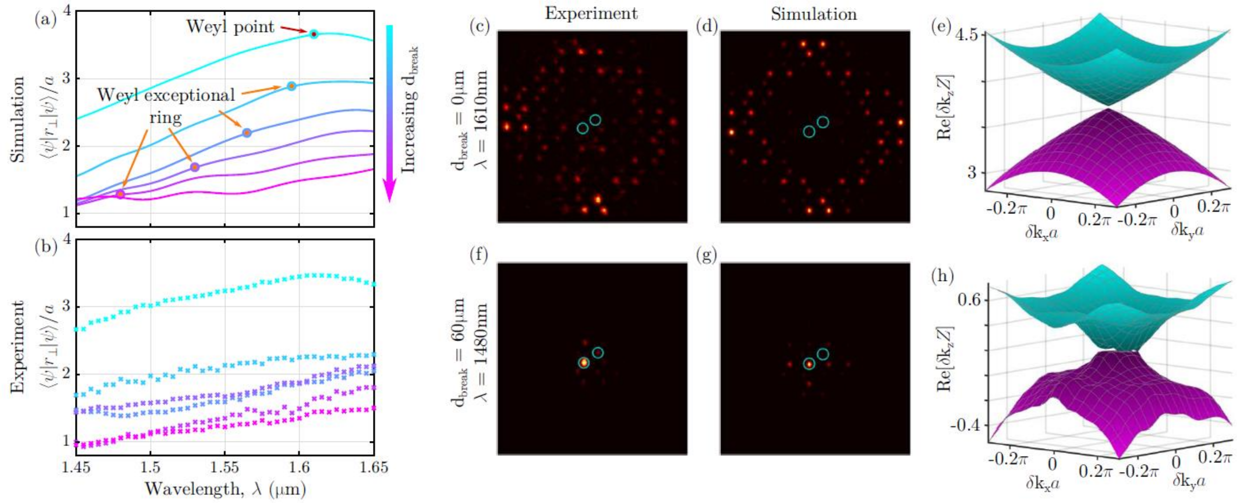


**Figure. 5.3.3. Distinguishing a WER from a Weyl point by observing the transverse radial propagation.** (a)-(b) Simulations and experimental observations of the transverse radial propagation, hψ|r⊥|ψi/a, for light injected into the center of the helical waveguide array as a function of the injected wavelength for six different break lengths $d_{break}$ = 0,20,40,50,60,70μm. The Hermitian system is shown in cyan, and redder colors indicate longer break lengths. Wavelengths where simulations predict either a Weyl point or WER are indicated in red and orange respectively. (For $d_{break}$ = 70μm the transition occurs near λ = 1400nm.) (c)-(d) Output intensity plots for light injected into the center of the system at the two indicated waveguides for the Hermitian system at the topological transition, λ = 1609nm, with a system length of L = 4cm. (e) Isofrequency surface for the Hermitian system at the topological transition calculated using full wave simulations and the cut and project method. (f)-(h) Similar to (c)-(e), except for the non-Hermitian system with $d_{break}$ = 60μm at λ = 1480nm. Note, the roughness seen in the non-Hermitian band structure simulations in (h) is a numerical artifact in the diagonalization procedure stemming from the large radiative background when $d_{break} > 0$.

To demonstrate that these simulation parameters (mainly the newly added gaps embedded along the waveguide) yield results which agree with experiment, we compare the total transmission as a function of break length for isolated, straight waveguides. As shown in Figure 5.3.4, from $d_{break}$ = 0, 10, 20, 30, 40, 50, 60, 70, to $d_{break}$ = 80μm, the chosen simulation parameters faithfully reproduce the experimental results. Here, the normalized experiment transmission loss is measured using a pre-calibrated attenuator working at 1,550nm. The break length $d_{break}$ is determined by the motion of the stage, and is also measured directly using a calibrated microscope.

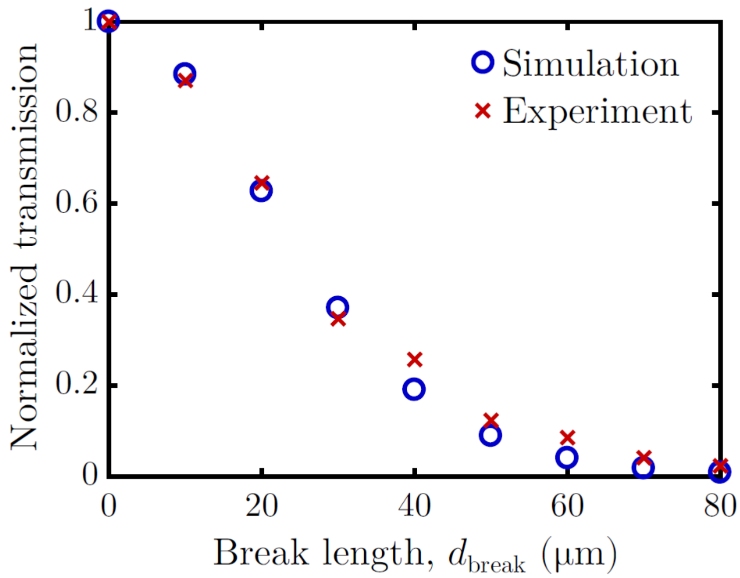


**Figure 5.3.4. Transmission as a function of break length for isolated, straight waveguides.** Experimental results are shown as red crosses, and simulation results are shown a blue circles. The total length of the system is L = 4.9 cm. For the purposes of break placement, the straight waveguides are assumed to have a fictitious helix pitch of Z = 1 cm, and 16 breaks are placed per helix pitch, each with length $d_{break}$.

In the second part of this sub-section (section 5.3), we present another work to demonstrate the power of photonic graphene as a tool in understanding exotic physics. In this waveguide array design, instead of following along a helical path, each individual waveguide has its unique pathway. Also please note that no one single waveguide has an identical pathway as any other waveguide in the array. The final experimental results [73] provide a platform for probing higher dimensional topological physics - a probe of 4-D quantum Hall physics.

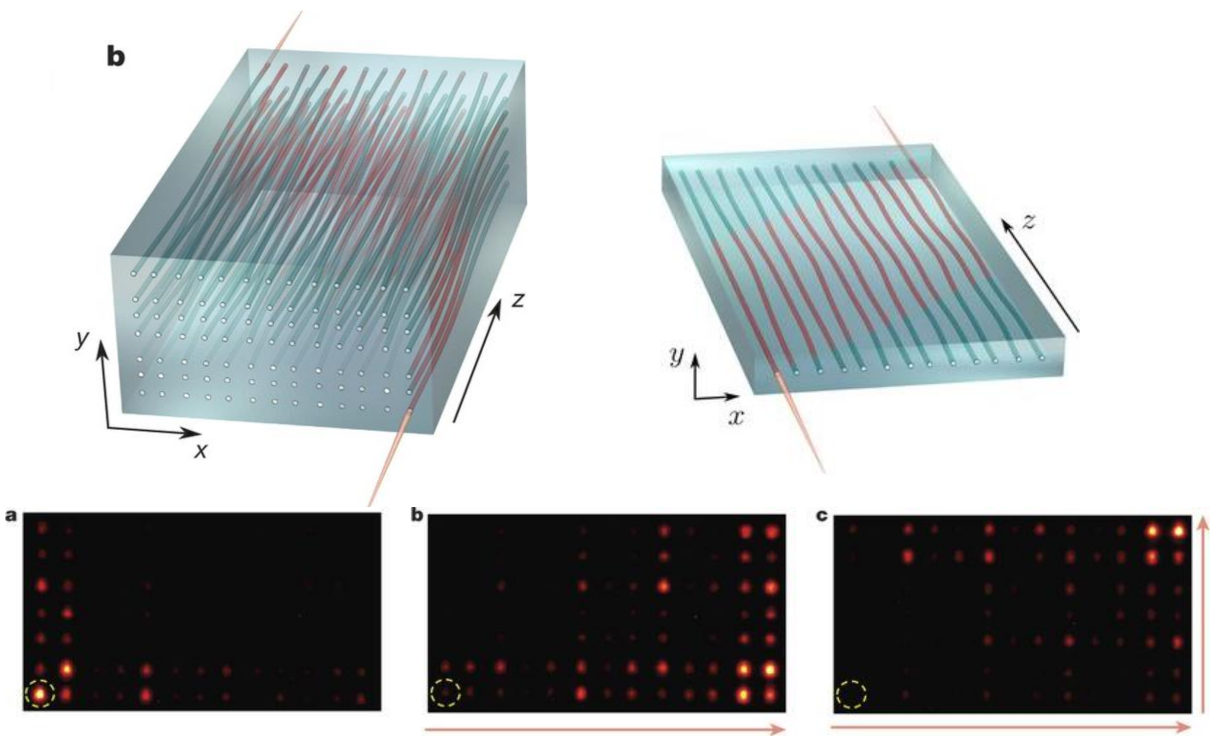


**Figure 5.3.5. Photonic topological boundary pumping as a probe of 4D quantum Hall physics.** Top row is the schematic of the waveguide lattice design. Notice every waveguide has its unique path. Bottom row are the results from the output end.

## 5.4 CROSS-TALK REDUCTION IN OPTICAL INTERCONNECT APPLICATIONS

For high density optical interconnect network, due to the close spacing between fiber cores within the fiber bundle or fiber ribbon, managing cross-talk has always been a challenge. As illustrated in Figure 5.4.1 [74-76], where we consider imaging an object through a certain length of fiber bundle, the image resolution is severely limited by the cross-talk introduced by the coupling between the cores (waveguides) of the bundle. Similarly, if instead, one considers each fiber core (each waveguide) as one data transmission carrier, cross-talk will also skew the signal at receiver's end. In this section, we show how the study of photonic graphene for fundamental physics also leads to a solution for cross-talk management for optical interconnect applications. Specifically, we focus on achieving cross-talk reduction for optical interconnect and telecommunication.

Our solution relies heavily on our waveguide lattice engineering capability. This capability was already explained in detail in sections 5.1- 5.3. The key of this solution is to make entire waveguide lattice helical with a relatively large radius (R is now on the order of 120μm, instead of ~ 4 - 7μm in sections 5.1-5.3), as shown in the very right column in Figure 5.4.2. A tight binding simulation result is present in the center column in Figure 5.4.2. It is worth noting that each pixel of the photo is actually carried by each single waveguide in the array. From the simulation, one can see that after light traveled through a long distance, for the same center to center spacing a, the output image from the 'fiber bundle' that has helical paths shows a much higher resolution than the one with straight and unmodified paths.

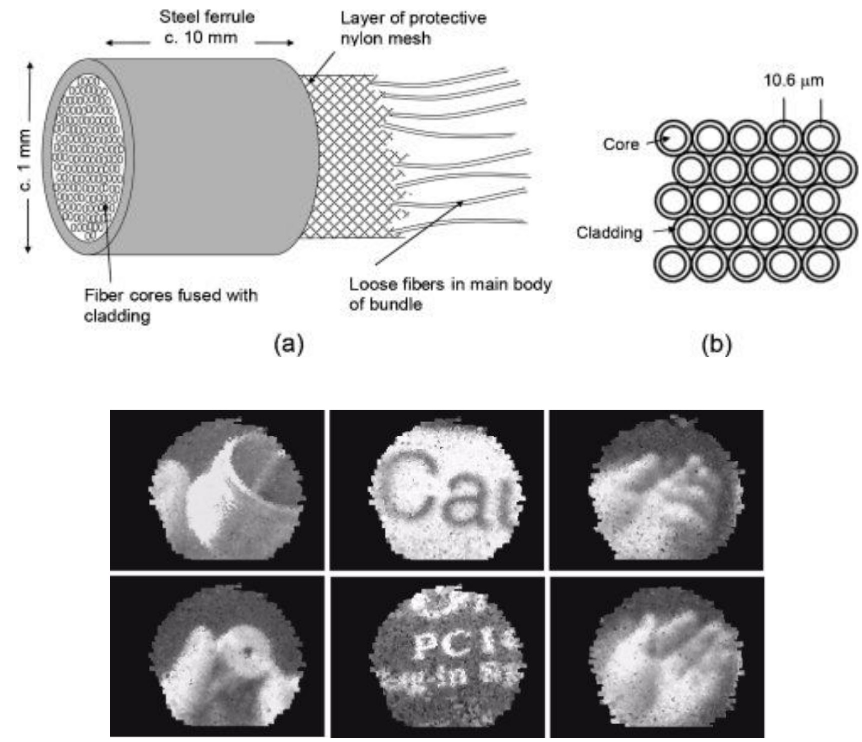


**Figure 5.4.1. Imaging objectives through a fiber bundle.** (a) illustration of a closely packed fiber bundle with a diameter of 1mm. (b) the cross-sectional view of the same fiber bundle, center to center spacing is 10.6μm.

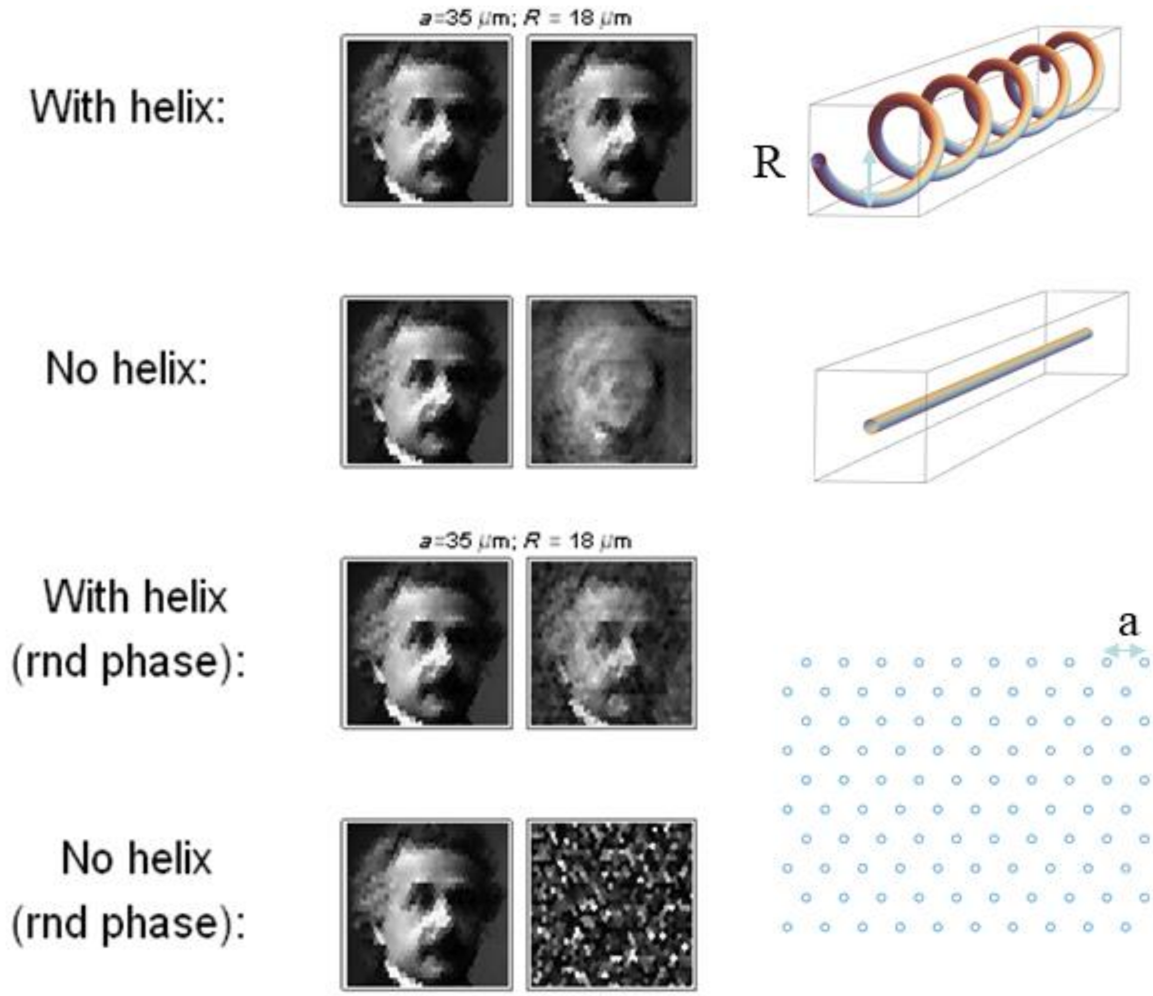


**Figure 5.4.2. A tight binding simulation result of an object imaged through a 'fiber bundle' (waveguide array).** Each pixel of the photo is actually carried by each single waveguide in the array.

To better understand and utilize this effect, various full wave simulations are used to predict the final output from the waveguide lattices fabricated using our Ultrafast Laser processing platform. Firstly, for the simplest case, we have only one single waveguide at the center of the array as the initial input, as shown in both top left and bottom left of Figure 5.4.3. It is therefore equivalent to imaging an objective with only one pixel. From the full wave simulation, the output from the straight, unmodified waveguide array shows a scrambled image. Indeed, judging from the first few frames of the propagation animation, the 'one pixel' quickly start to scramble and form multiple 'pixels' even before it reaches the final output end, where the input channel eventually interferes with the entire array, as shown in top right of Figure 5.4.3. In comparison, in the helical array, the 'one pixel' remains inside the same waveguide/channel throughout the propagation distance ~ 15cm, as shown in bottom right of Figure 5.4.3.

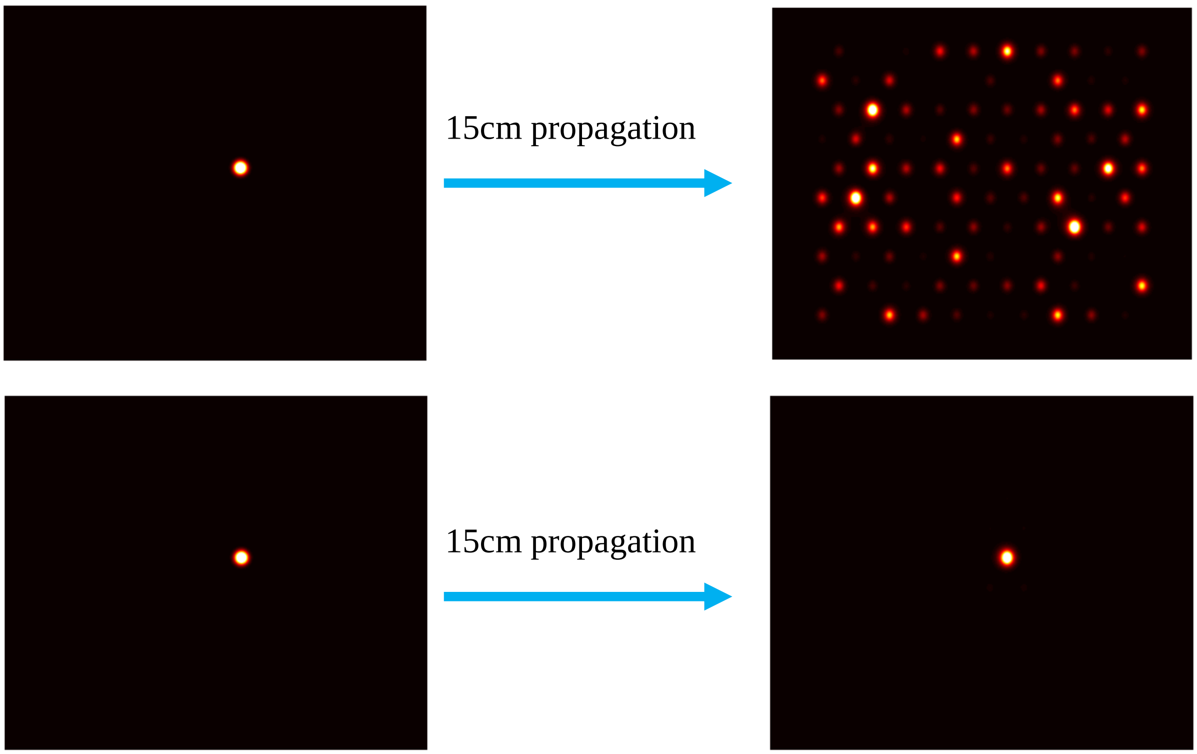


**Figure 5.4.3. A full wave simulation result of one single 'pixel' imaged through a 'fiber bundle' (waveguide array).** Each pixel of the photo is actually carried by each single waveguide in the array. (a) Top row: straight waveguide array. (b) Bottom row: helical waveguide arrays, with Z = 1.5cm, R = 32um.

Secondly, we consider a more complex case: instead of just one, now we have 4 waveguides close to the center of the array as the initial input (4 pixels), as shown in the left column in Figure 5.4.4. The 4 red dots in each lattice cross-sectional schematic indicate the initial input locations. It is important to understand that because the cross-talk increases exponentially vs the waveguide center to center spacing a, in general, the smaller the spacing a is, the stronger cross-talk the waveguide array will have. As shown in Figure 5.4.4, in the straight, unmodified array, apparent cross-talk is observed starting from a = 45µm. The cross-talk became even more severe for a < 45µm. On the other hand, in the arrays with helix-optimization, the center to center spacing a can go down to 30µm without us observing any cross-talk. A further optimization can be realized by modifying the helix path to form a helix-like path. This helix-like optimization is based on a perturbation of the helical path, predicted using our tight-binding model. With the help of helix-like optimization, the spacing a can go down one more step to 20µm with minimum cross-talk, as shown in the bottom row of Figure 5.4.4.

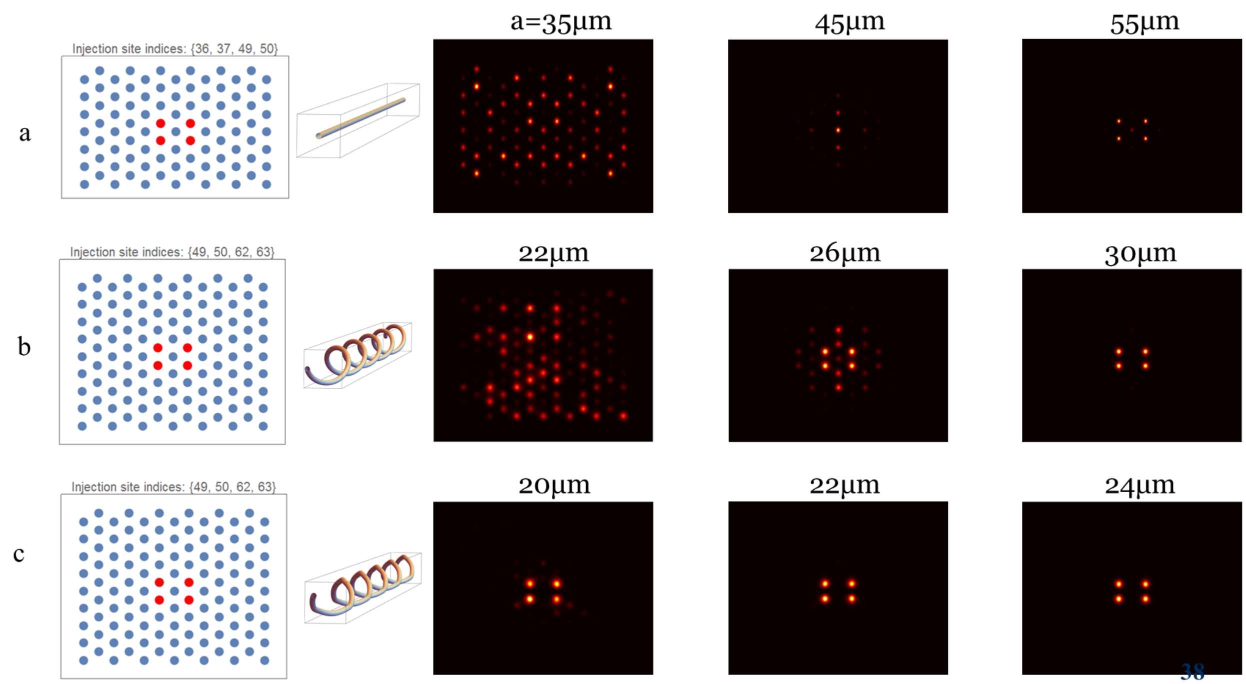


**Figure 5.4.4. A full wave simulation result of 4 'pixels' imaged through a 'fiber bundle' (waveguide array).** Each pixel of the photo is actually carried by each single waveguide in the array. The red dots indicate the initial 4 'pixels' input. (a) Top row: straight waveguide array with center to center spacing a = 35, 45, 55µm. (b) Middle row: helical waveguide arrays with center to center spacing a = 22, 26, 32µm. (c) Bottom row: helix-like waveguide arrays with center to center spacing a = 20, 22, 24µm.

Notice that in Figure 5.4.4 row(a), (b), and (c) have different levels of difficulties in restoring the input signal, because they do not share the same set of center to center spacing a. Obviously, the number 20μm is just the minimum we can achieve for our index profile (Gaussian profile, peak index contrast value ~ 2.8E-3), at 1,550nm. For example, if we have fiber cores with higher index contrast and working at shorter wavelength, then with the same principle, we can certainly achieve much smaller spacing than the number 20μm.

Our experimental demonstration of the cross-talk management solution is shown in Figure 5.4.5. The results are very similar to the results from the full-wave simulation. The input image is again the ‘4 pixels’, with the distances between the pixels equal to spacing a. This ‘4 pixels’ input signal is achieved by adiabatically splitting a single waveguide into 4 waveguides evenly at the same location. This is proven in top row rightmost result, where a = 55μm and the waveguides in the array are complete straight. The fiber bundle undergoes no observable cross-talk in this trivia case, as the spacing a is too large to introduce any cross-talk when the signal propagates 15cm. At a = 24μm, however, one can notice how the 4 input ‘pixels’ eventually light up the entire ‘fiber bundle’ at the output end, indicating strong interference with other channels within the same array. Next, after applying the helix optimization, the energy distributes mostly among the 6 ‘pixels’ right at the output, showing a closer resemblance of the input image. Finally, on the bottom row, the ‘fiber bundle’ with the helix-like optimization fully restores the 4 ‘pixels’ input image. Note that the only difference between Figure 5.4.5 (experimental result) and Figure 5.4.4 (full wave simulation result) is the set of spacing a used in different arrays, with the purpose now being shifted to comparing the results of the helix optimization versus that of the helix-like optimization. The consistent cross-talk reduction results from both the simulation (shown in Figure 5.4.4) and experimental data (shown in Figure 5.4.5) again validate the potential of using Ultrafast laser fabrication platform for research and development in optical interconnect applications.

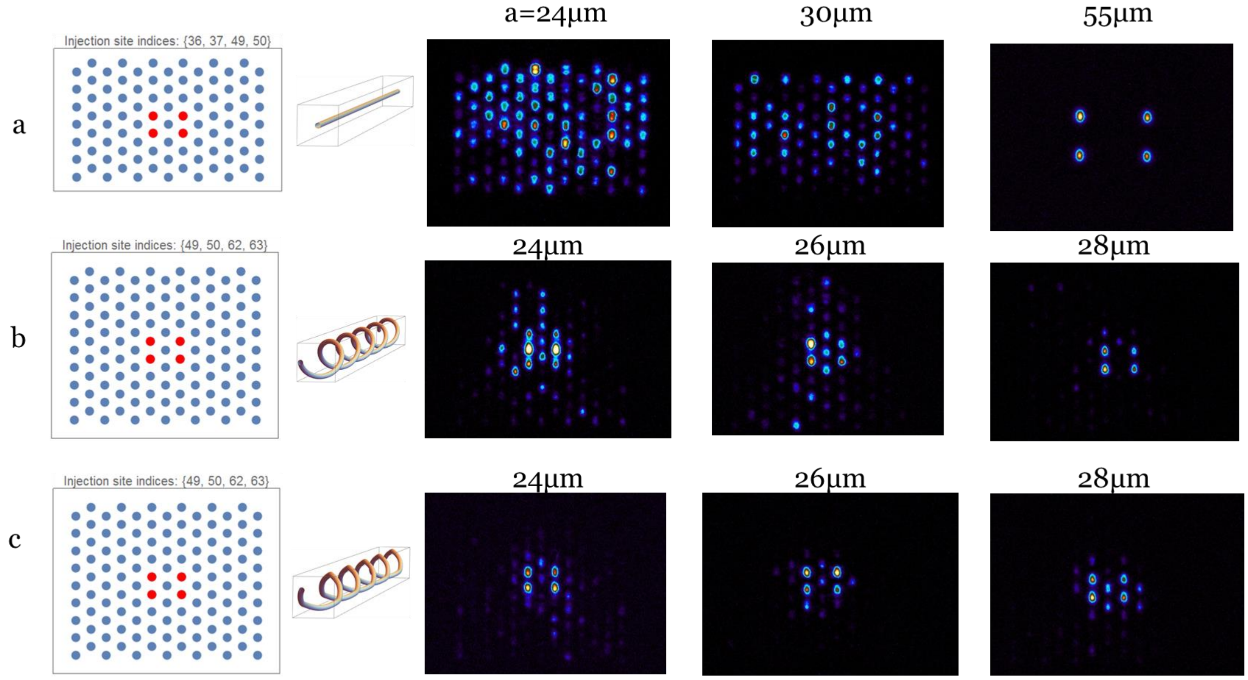


**Figure 5.4.5. An experimental result of 4 'pixels' imaged through a 'fiber bundle' (waveguide array).** Each pixel of the photo is actually carried by each single waveguide in the array (split from a single waveguide in experiment). The red dots on the leftmost column indicate the initial 4 'pixels' input. (a) Top row: straight waveguide array with center to center spacing a = 24, 30, 55µm. (b) Middle row: helical waveguide arrays with center to center spacing a = 24, 26, 28µm. (c) Bottom row: helix-like waveguide arrays with center to center spacing a = 24, 26, 28µm.

As an illustration of how large a typical waveguide array is, Figure 5.4.6 demonstrates the scale of the 3-D waveguide arrays and their end facets. With our platform, one can fabricate dozens of densely packed waveguide arrays on a single glass chip. Each waveguide array is on the order of ~ 200μm in width/depth, and tens of cm in length.

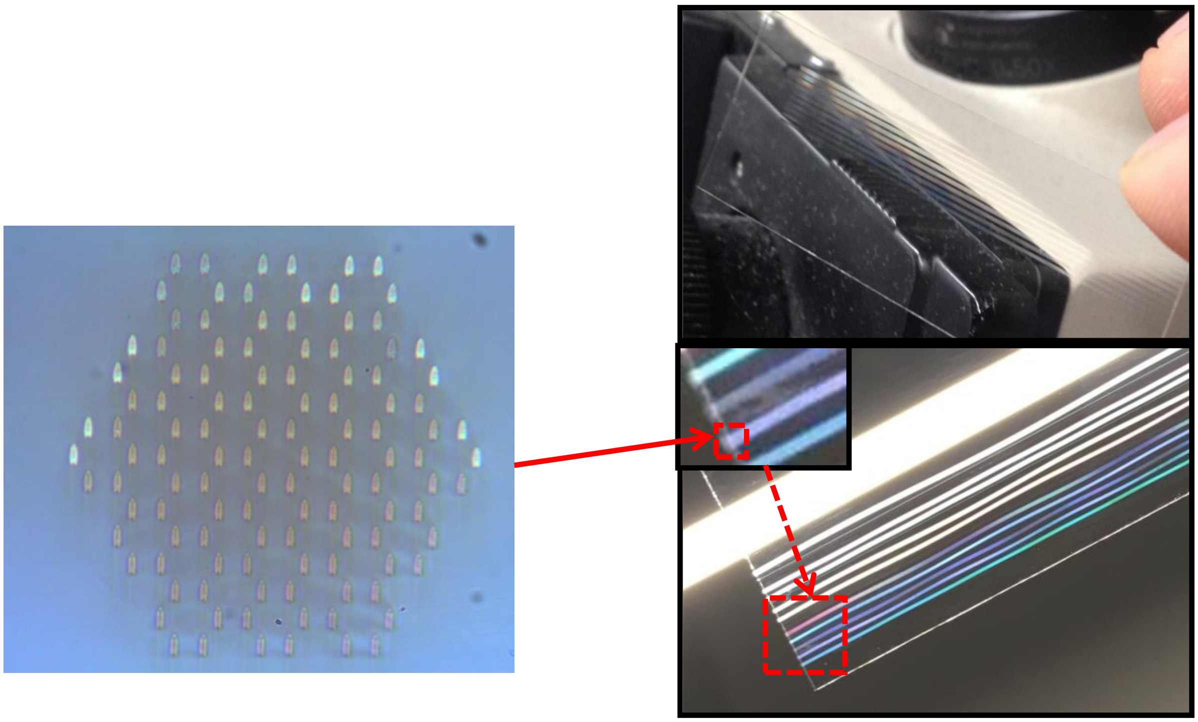

**Figure 5.4.6. Illustration of the scales of our fabricated 3-D waveguide arrays.** Each white/color 'line' represents one waveguide array (one waveguide array consists of hundreds of waveguides). The colorful pattern is due to the room light (white) being diffracted by the waveguide arrays, similar to when white light is diffracted by an optical diffraction grating.

## CONCLUSIONS AND FUTURE WORK

Section 1-3 of this dissertation presents recent results on waveguide photonic devices based on flexible glass and its use in photonic integrated circuits. Flexible glass and multifunctional fiber represent new classes of flexible optical substrates for waveguide photonic applications. At the end of the dissertation, it is worthwhile compare mechanical, thermal, and optical properties of both polymer optical substrates and flexible glass substrates. Considering optical waveguides inscribed in flexible glass by the ultrafast laser direct writing technique, Table 2 presents a useful comparison.

**Table 2**: Comparison between Polymer flexible photonics and glass flexible photonics technology

| Technical Specification | Flexible Photonics in Polymer | Flexible Photonics in Glass |
|---|---|---|
| 3-D Architecture | Limited (layer-by-layer) | **Yes and highly flexible** |
| Durability/Lifetime | Poor | **Excellent** |
| Waveguide Loss | 0.3-1.3 dB/cm | **<0.25 dB/cm** |
| Material/Substrate Cost | **Low** | **Low** |
| Active lasing device | **Yes** | **Yes** |
| Substrate Flexibility | **Bending radius ~ 1cm** | Bending radius ~ 3cm |
| $\Delta n$ | **Up to 0.05** | Up to 0.01 |
| 2$^{nd}$ Order Nonlinearity $\chi_2$ | **Could be high (e.g. $\chi_2$=745 pm/V)** | Possible, but less than 5 pm/V |

As discussed in this dissertation, waveguides fabricated in flexible glass substrates *with proven optical qualities* possess superior device performance in terms of durability, lifetime, and optical loss than those made in polymer materials. Further, both flexible glasses and polymer materials can be effective media useful for laser and active photonic devices. The former are enabled by long history of active glass material developments using rare-earth dopants (i.e. Er, Yr, Tm, Pm-, and etc). The latter is facilitated by wide selections of active light-emitting polymer materials.

The advent of flexible glass could present a transformative alternative for flexible photonics in some applications. Use of the ultrafast laser waveguide writing technique, replaces material challenges incurred in polymer-based flexible photonic devices with laser manufacturing technology innovations by fabricating flexible photonics components in highly stable flexible glasses using femtosecond ultrafast lasers. The further research and development in this field could open a completely new avenue to produce low-cost and high-quality flexible photonics components with superior performance.

Section 4 of this dissertation demonstrates that, through active laser beam shaping, and refractive index profile modeling, our laser-written waveguide can effectively interact with themselves and/or with other pre-fabricated photonic components.

Finally, in section 5, we explained in detail how our refractive index engineering capability was achieved. With the help of index engineering, we fabricated several photonic graphene designs. We further show that not only it is a powerful tool for discovering fundamental physics (section 5.1-5.3), but it also shows a great potential to be a solution for real world cross-talk management for telecommunication applications (section 5.4).

The work covered in this dissertation mainly focuses on linear glass materials. However, ultrafast laser writing technique can also be applied onto nonlinear glass materials. One type of nonlinear optical material called Chalcogenide glass is among the most promising nonlinear optical materials. With its large nonlinear refractive index (~1000 times that of conventional linear glass material), Chalcogenide glass can lower switching times of photonic integrated circuit down to femtoseconds scale. This can potentially increase the bandwidth of optical network by another level. On the other hand, the large nonlinearity of Chalcogenide glass can also be beneficial to the exploration of the nonlinear properties of photonic graphene. Since photonic graphene now would have a fundamentally new dispersion, a novel understanding of nonlinear optics in photonic graphene is bound to yield both new scientific knowledge and device applications. However, as indicated from our initial work on nonlinear material, Ultrafast laser fabrication on Chalcogenide glass substrate remains a very challenging task. In particular when fabricating 3D structures, the relatively poor thermal stability makes controlling the performance of the laser written waveguide very difficult. One ongoing effort is to extend the complexity of our refractive index profile calibration process. This process is described in section 4, and it involves a combination of numerical simulation and a large experimental data set. Our future work will aim at expanding the experimental data set even further, and utilizing machine learning to link the simulation and experimental data set.

# APPENDIX A: PUBLICATIONS

## A.1 PATENTS

**<u>Sheng Huang</u>**, Ming-Jun Li, and Kevin P. Chen, "Optical Interconnections Using Glass Substrates," Patent SN: 62/160,816.

**<u>Sheng Huang</u>,** A. Yan, S. Li, R. Chen, P. Ohodnicki, M. Buric, K.P. Chen, "Method to enhance Rayleigh scattering and their high temperature stability in optical fiber for distributed temperature measurements, " Patent pending, Ref: 04137. (2017).

## A.2 EDITED BOOKS AND CHAPTERS

**<u>Sheng Huang</u>,** M. Li, and Kevin P. Chen, "Guided-Wave Photonics in Flexible Glass," Chapter in ***Flexible Glass***, Sean M Garner (Ed.), Corning Inc., ISBN 978-1-118-94636-7 (2017).

## A.3 PEER REVIEWED JOURNALS

* Co-First Author, authors contributed equally to the work.

**Sheng Huang,** M. Wang, R. Chen, R. Zou, R. Cao, S. Li, A. Yan, and Kevin P.Chen, " Ultrafast Laser Fabrication Platform: Lightwave Circuits and Interconnect on Glass," *IEEE Journal of Lightwave Technology*, Manuscript submitted for publication.

**Sheng Huang**, M. Li, S. Garner, M. Li, and K. Chen, "Flexible photonic components in glass substrates," *Opt. Express* 23, 22532-22543 (2015).

O. Zilberberg, **Sheng Huang**, J. Guglielmon, Mohan Wang, Kevin P. Chen, Yaacov E. Kraus and Mikael C. Rechtsman, " Photonic topological boundary pumping as a probe of 4D quantum Hall physics," *Nature*. 553. 59-62 (2018).

J. Noh* / **Sheng Huang*** / D. Leykam*, Y. D. Chong, Kevin P. Chen, and Mikael C. Rechtsman, "Experimental observation of optical Weyl points and Fermi arc-like surface states," *Nature Phys.* 13, 611–617 (2017).

J. Noh* / W. Benalcazar* / **Sheng Huang***, M. J Collins, Kevin P. Chen, Taylor L Hughes , and Mikael C. Rechtsman, " Topological protection of photonic mid-gap defect modes," *Nature Photonics*, 1 (2018).

J. Noh, **Sheng Huang**, D. Leykam, YD Chong, Kevin P. Chen, and Mikael C Rechtsman. "Observation of Weyl points in Optics," *Optics and Photonics News*, Special Issue on "Optics in 2017" (2017).

J. Noh* / **Sheng Huang***, Kevin P. Chen, and Mikael C. Rechtsman, "Observation of Photonic Topological Valley-Hall Edge States," *Physical Review Letters (PRL)*, 120, 063902 (2018).

A. Yan* / **Sheng Huang***, S. Li, R. Chen, P. Ohodnicki, M. Buric, S. Lee, Ming-Jun Li, and Kevin Chen, "Distributed Optical Fiber Sensors with Ultrafast Laser Enhanced Rayleigh Backscattering Profiles for Real-Time Monitoring of Solid Oxide Fuel Cell Operations," *Scientific Reports*, 7:9360 (2017).

J. Guglielmon, **Sheng Huang**, Kevin P. Chen, and Mikael C. Rechtsman, “Photonic realization of a transition to a strongly driven Floquet topological phase," *Phys. Rev. A* 97, 031801(R) (2018).

S. Li, L. Liu, A. Yan, **Sheng Huang**, X. Huang, R. Chen, Y. Lu, and Kevin Chen, "A compact field-portable double-pulse laser system to enhance laser induced breakdown spectroscopy," *Review of Scientific Instruments* 88, 023109 (2017).

Shaymaa Riyadh Tahhan, R. Chen, **Sheng Huang**, Khalil I. Hajim, and Kevin P. Chen, "Fabrication of Fiber Bragg Grating Coating with TiO2 Nanostructured Metal Oxide for Refractive Index Sensor," *Journal of Nanotechnology*, vol. 2017, Article ID 2791282, doi:10.1155/2017/2791282. (2017).

M. Li, **Sheng Huang**, Q. Wang, H. Petek, and K. Chen, "Nonlinear lightwave circuits in chalcogenide glasses fabricated by ultrafast laser," *Opt. Lett.* 39, 693-696 (2014).

M. Li, **Sheng Huang**, Q. Wang and H. Petek, K. P. Chen, "Nonlinear optical localization in embedded chalcogenide waveguide arrays," *AIP Advances*, 4, 057120 (2014).

B. McMillen, M. Li, **Sheng Huang**, B. Zhang, and K. Chen, "Ultrafast laser fabrication of Bragg waveguides in chalcogenide glass," *Opt. Lett.* 39, 3579-3582 (2014).

## A.4 CONFERENCE PAPERS AND INVITED TALKS

**Sheng Huang**, M. Wang, Y. Huang, R. Cao, S. Li, R. Zou, A. Yan, M.-J. Li, and K. P.Chen, "Fabrication of Lightwave Circuits on Flat Fibers: System-in-Fiber," in *Conference on Lasers and Electro-Optics* (CLEO), paper JW2A.137, San Jose, CA, 2017

(Invited) **Sheng Huang**, Y. Huang, R. Cao, M.-J. Li, and K. P. Chen , " Multilayer optical interconnects using ultrafast laser direct written 3-D waveguides and ion exchange surface waveguides ," Proc. SPIE Photonics West, Conference on Optics Interconnect , paper 9753-15, San Francisco, California ,February 13-18 (2016).

(Invited) **Sheng Huang**, M. -J. Li, and K. P. Chen, "Fiber for system-on-fiber applications," *Asia Communication and Photonics Conference*, paper AM1D.2, Hong Kong, November 23 (2015).

**Sheng Huang**, M. J. Li and K. P. Chen, "Board-level optical interconnect using glass," 2015 Conference on Lasers and Electro-Optics (CLEO), paper SW1K.5, San Jose, CA, 2015.

**Sheng Huang**, M. Li, K. Chen, S. Garner, and M. Li, "Ultrafast Laser Fabrication of 3-D Photonic Components in Flexible Glasses," in *Optical Fiber Communication Conference*, OSA Technical Digest (online) (Optical Society of America, 2014)

(Invited) **Sheng Huang**, S. Garner, and K. P. Chen, "Ultrafast laser fabrication of 3-D photonic components in flexible glasses," ICALEO 2013, Miami, Florida, United States, October 6-10, 2013

**Sheng Huang**, M. Li, K. Chen, S. Garner, and M. Li, "Ultrafast Laser Fabrication of 3-D Photonic Components in Flexible Glasses," in Optical Fiber Communication Conference (OFC), OSA Technical Digest (online) (Optical Society of America, 2014), Optical Fiber Communication Conference, San Francisco, California, United States, March 9-13, 2014

M. Wang, MASB Zaghloul, **Sheng Huang**, A. Yan, S. Li, R. Zou, P. Ohodnicki, M. BUric, M.-J. Li, D. Carpenter, J. Daw and K. P.Chen, "Ultrafast Laser Enhanced Rayleigh Backscattering on Silica Fiber for Distributed Sensing under Harsh Environment," in *Conference on Lasers and Electro-Optics* (CLEO), paper ATh3P. 4, San Jose, CA, 2018

A. Cerjan, **Sheng Huang**, K. P Chen, Y. Chong, Mikael Rechtsman, " Weyl exceptional ring in a helical waveguide array," in *Conference on Lasers and Electro-Optics* (CLEO), paper FM3Q. 2, San Jose, CA, 2018

(Invited) J. Noh* / **Sheng Huang*** / D. Leykam*, Y. D. Chong, K.Chen, and M.C. Rechtsman, "Experimental observation of optical Weyl points and Fermi arcs," in *Conference on Lasers and Electro-Optics* (CLEO), paper FM3G.3, San Jose, CA, 2017

J. Noh, **Sheng Huang**, K. Chen, and Mikael C. Rechtsman, "Observation of Photonic Topological Valley Transport," in *Conference on Lasers and Electro-Optics* (CLEO), paper FTh1D.2, San Jose, CA, 2017

J. Guglielmon, **Sheng Huang**, K. Chen, and Mikael C. Rechtsman, "Prediction and Realization of a Photonic Topological Phase Transition," in *Conference on Lasers and Electro-Optics* (CLEO), paper FM2G. 6, San Jose, CA, 2017

M. Burica, B. Liu, **Sheng Huang**, M. Wang, K.P. Chen, Lua,P. Ohodnickia, "Modified single crystal fibers for distributed sensing applications,". Proc. SPIE 10208, Fiber Optic Sensors and Applications XIV, 102080C (27 April 2017); doi: 10.1117/12.2262992

A. Yan, **Sheng Huang**, S. Li, P. Ohodnicki, and K. Chen, "Fiber Optical Methane Sensors Using Functional Metal Oxide Nanomaterials," *in Asia Pacific Optical Sensors Conference*, OSA Technial Digest (online), paper W4A.12. Shanghai China, 11–14 October (2016),

M. Buric, P. Ohodnicki, A. Yan, **Sheng Huang**, K. P. Chen, "Distributed fiber-optic sensing in a high-temperature solid-oxide fuel cell, " *Proc. SPIE 9977, Remote Sensing System Engineering VI*, 997708 (September 19, 2016)

R. Zou, S. Wang, M. Wang, S. Li, **Sheng Huang**, Y. Lin, K.P. Chen, "Adaptive laser beam forming for laser shock micro-forming for 3-D MEMS devices fabrication," *Proc. SPIE 9983, Pacific Rim Laser Damage 2016: Optical Materials for High-Power Lasers*, 99830U, July 22, (2016).

(Invited) M. Zaghloul, A. Yan, R. Chen, **Sheng Huang**, M. -J. Li, and K. P. Chen , " Multi-functional fiber sensors for radiation environments ," *SPIE Conference on Security and Sensing*, Baltimore, MD, April 21-26 (2016).

M. Li, **Sheng Huang**, Q. Wang, and K. Chen, "Optical Switching by Nonlinear Lightwave Circuits Inscribed in Chalcogenide Glass by Ultrafast Laser," in Advanced Photonics, OSA Technical Digest (online) (Optical Society of America, 2014), Bragg Gratings, Photosensitivity, and Poling in Glass Waveguides, Barcelona Spain July 27-31, 2014

# BIBLIOGRAPHY


1. Se Hyun Ahn and L. Jay Guo, "High-Speed Roll-to-Roll Nanoimprint Lithography on Flexible Plastic Substrates," Adv. Mater. 20, 2044-2049 (2008).

2. Jong G. Ok, Hong Seok Youn, Moon Kyu Kwak, Kyu-Tae Lee, Young Jae Shin, L. Jay Guo, Anton Greenwald, and Yisi Liu, "Continuous and scalable fabrication of flexible metamaterial films via roll-to-roll nanoimprint process for broadband plasmonic infrared filters," Appl. Phys. Lett. 101, - (2012).

3. Makoto Hikita, Ryoko Yoshimura, Mitsuo Usui, Satoru Tomaru, and Saburo Imamura, "Polymeric optical waveguides for optical interconnections," Thin Solid Films 331, 303-308 (1998).

4. Seiji Toyoda, Naoki Ooba, Makoto Hikita, Takashi Kurihara, and Saburo Imamura, "Propagation loss and birefringence properties around 1.55 μm of polymeric optical waveguides fabricated with cross-linked silicone," Thin Solid Films 370, 311-314 (2000).

5. Ming Zhou, "Low-loss polymeric materials for passive waveguide components in fiber optical telecommunication," OPTICE 41, 1631-1643 (2002).

6. L. Eldada and L. W. Shacklette, "Advances in polymer integrated optics," IEEE J. Sel. Topics Quantum Electron 6, 54-68 (2000).

7. H. Ma, A. K. Y. Jen, and L. R. Dalton, "Polymer-Based Optical Waveguides: Materials, Processing, and Devices," Adv. Mater. 14, 1339-1365 (2002).

8. R. Dangel, C. Berger, R. Beyeler, L. Dellmann, M. Gmur, R. Hamelin, F. Horst, T. Lamprecht, T. Morf, S. Oggioni, M. Spreafico, and B. J. Offrein, "Polymer-Waveguide-Based Board-Level Optical Interconnect Technology for Datacom Applications," Advanced Packaging, IEEE Transactions on 31, 759-767 (2008).

9. R. Dangel, F. Horst, D. Jubin, N. Meier, J. Weiss, B. J. Offrein, B. W. Swatowski, C. M. Amb, D. J. DeShazer, and W. K. Weidner, "Development of Versatile Polymer Waveguide Flex Technology for Use in Optical Interconnects," J. Lightwave Technol. 31, 3915-3926 (2013).

10. Brandon W. Swatowski, Chad M. Amb, Sarah K. Breed, David J. Deshazer, W. Ken Weidner, Roger F. Dangel, Norbert Meier, and Bert J. Offrein, "Flexible, stable, and easily processable optical silicones for low loss polymer waveguides," in Proceedings of SPIE, 2013), 862205-862205-862211.

11. Han Zhou, Jung-Hun Seo, Deborah M. Paskiewicz, Ye Zhu, George K. Celler, Paul M. Voyles, Weidong Zhou, Max G. Lagally, and Zhenqiang Ma, "Fast flexible electronics with strained silicon nanomembranes," Sci. Rep. 3(2013).

12. Lan Li, Hongtao Lin, Shutao Qiao, Yi Zou, Sylvain Danto, Kathleen Richardson, J. David Musgraves, Nanshu Lu, and Juejun Hu, "Integrated flexible chalcogenide glass photonic devices," Nat. Photon. 8, 643-649 (2014).

13. A. Scott Shelley and G. Lagally Max, "Elastically strain-sharing nanomembranes: flexible and transferable strained silicon and silicon–germanium alloys," Journal of Physics D: Applied Physics 40, R75 (2007).

14. Chun L. Yu, Hyunwoo Kim, Nathalie de Leon, Ian W. Frank, Jacob T. Robinson, Murray McCutcheon, Mingzhao Liu, Mikhail D. Lukin, Marko Loncar, and Hongkun Park, "Stretchable Photonic Crystal Cavity with Wide Frequency Tunability," Nano Letters 13, 248-252 (2012).

15. Yu Chen, Huan Li, and Mo Li, "Flexible and tunable silicon photonic circuits on plastic substrates," Sci. Rep. 2(2012).

16. E. Bosman, G. Van Steenberge, B. Van Hoe, J. Missinne, J. Vanfleteren, and P. van Daele, "Highly Reliable Flexible Active Optical Links," Photonics Technology Letters, IEEE 22, 287-289 (2010).

17. Weiquan Yang, Hongjun Yang, Guoxuan Qin, Zhenqiang Ma, Jesper Berggren, Mattias Hammar, Richard Soref, and Weidong Zhou, "Large-area InP-based crystalline nanomembrane flexible photodetectors," Appl. Phys. Lett. 96, - (2010).

18. Li Fan, Leo T. Varghese, Yi Xuan, Jian Wang, Ben Niu, and Minghao Qi, "Direct fabrication of silicon photonic devices on a flexible platform and its application for strain sensing," Opt. Express 20, 20564-20575 (2012).

19. Chen Janglin and C. T. Liu, "Technology Advances in Flexible Displays and Substrates," Access, IEEE 1, 150-158 (2013).

20. Sean Garner, Scott Glaesemann, and Xinghua Li, "Ultra-slim flexible glass for roll-to-roll electronic device fabrication," Appl. Phys. A 116, 403-407 (2014).

21. K. M. Davis, K. Miura, N. Sugimoto, and K. Hirao, "Writing waveguides in glass with a femtosecond laser," Opt. Lett. 21, 1729-1731 (1996).

22. Jiaren Liu, Zhiyi Zhang, Shoude Chang, Costel Flueraru, and Chander P. Grover, "Directly writing of 1-to-N optical waveguide power splitters in fused silica glass using a femtosecond laser," Opt. Commun. 253, 315-319 (2005).

23. Graham D. Marshall, Martin Ams, and Michael J. Withford, "Direct laser written waveguide-Bragg gratings in bulk fused silica," Opt. Lett. 31, 2690-2691 (2006).

24. N. D. Psaila, R. R. Thomson, H. T. Bookey, A. K. Kar, N. Chiodo, R. Osellame, G. Cerullo, A. Jha, and S. Shen, "Er:Yb-doped oxyfluoride silicate glass waveguide amplifier fabricated using femtosecond laser inscription," Appl. Phys. Lett. 90, 131102-131102-131103 (2007).

25. W. J. Chen, S. M. Eaton, H. B. Zhang, and P. R. Herman, "Broadband directional couplers fabricated in bulk glass with high repetition rate femtosecond laser pulses," Opt. Express 16, 11470-11480 (2008).

26. F. M. Bain, A. A. Lagatsky, R. R. Thomson, N. D. Psaila, N. V. Kuleshov, A. K. Kar, W. Sibbett, and C. T. A. Brown, "Ultrafast laser inscribed Yb:KGd(WO4)2 and Yb:KY(WO4)2 channel waveguide lasers," Opt. Express 17, 22417-22422 (2009).

27. R. R. Thomson, T. A. Birks, S. G. Leon-Saval, A. K. Kar, and J. Bland-Hawthorn, "Ultrafast laser inscription of an integrated photonic lantern," Opt. Express 19, 5698-5705 (2011).

28. Chao Zhang, Ningning Dong, Jin Yang, Feng Chen, Javier R. Vázquez de Aldana, and Qingming Lu, "Channel waveguide lasers in Nd:GGG crystals fabricated by femtosecond laser inscription," Opt. Express 19, 12503-12508 (2011).

29. J. C. Ng, C. B. Li, P. R. Herman, and L. Qian, "Femtosecond laser writing of a flat-top interleaver via cascaded Mach-Zehnder interferometers," Opt. Express 20, 17894-17903 (2012).

30. R. R. Gattass and E. Mazur, "Femtosecond laser micromachining in transparent materials," Nat. Photon. 2, 219-225 (2008).

31. Limin Tong, Rafael R. Gattass, Iva Maxwell, Jonathan B. Ashcom, and Eric Mazur, "Optical loss measurements in femtosecond laser written waveguides in glass," Opt. Commun. 259, 626-630 (2006).

32. S. M. Eaton, W. Chen, L. Zhang, H. Zhang, R. Iyer, J. S. Aitchison, and P. R. Herman, "Telecom-band directional coupler written with femtosecond fiber laser," IEEE Photonics Technol. Lett. 18, 2174-2176 (2006).

33. Graeme Brown, Robert R. Thomson, Ajoy K. Kar, Nicholas D. Psaila, and Henry T. Bookey, "Ultrafast laser inscription of Bragg-grating waveguides using the multiscan technique," Opt. Lett. 37, 491-493 (2012).

34. R. Osellame, S. Taccheo, M. Marangoni, R. Ramponi, P. Laporta, D. Polli, S. De Silvestri, and G. Cerullo, "Femtosecond writing of active optical waveguides with astigmatically shaped beams," J. Opt. Soc. Am. B **20**, 1559-1567 (2003).

35. S. M. Eaton, H. Zhang, M. L. Ng, J. Li, W.-J. Chen, S. Ho, and P. R. Herman, "Transition from thermal diffusion to heat accumulation in high repetition rate femtosecond laser writing of buried optical waveguides," Opt. Express **16**, 9443-9458 (2008).

36. S. Eaton, H. Zhang, P. Herman, F. Yoshino, L. Shah, J. Bovatsek, and A. Arai, "Heat accumulation effects in femtosecond laser-written waveguides with variable repetition rate," Opt. Express **13**, 4708-4716 (2005).

37. H. Zhang, S. Eaton, and P. Herman, "Single-step writing of Bragg grating waveguides in fused silica with an externally modulated femtosecond fiber laser," Opt. Lett. **32**, 2559-2561 (2007).

38. B. McMillen, M. Li, S. Huang, B. Zhang, and K.P. Chen, "Ultrafast laser fabrication of Bragg waveguides in chalcogenide glass," Opt. Lett. **39**, 3579-3582 (2014).

39. H. JERRARD, "Optical compensators for measurement of elliptical polarization," J. Opt. Soc. Am. **38,** 35-57 (1948).

40. R. Plumb, "Analysis of elliptically polarized light," J. Opt. Soc. Am. **50**, 892- (1960).

41. B. Grunstra and H. Perkins, "A method for the measurement of optical retardation angles near 90 degrees," Appl. Opt. **5**, 585-587 (1966).

42. R. T. Chen, L. Lin, C. Choi, Y. J. Liu, B. Bihari, L. Wu, S. Tang et al, "Fully embedded board-level guided-wave optoelectronic interconnects," in Proc. of the IEEE, vol. 88, no. 6, pp. 780-793, Jun. 2000.

43. D. Taillaert, W. Bogaerts, P. Bienstman, T. F. Krauss, P. V. Daele, I. Moerman, S. Verstuyft, K. D. Mesel, and R. Baets, "An out-of-plane grating coupler for efficient butt-coupling between compact planar waveguides and single-mode fibers," IEEE J. Quantum Electron., vol. 38, no. 7, pp. 949-955, Jul. 2002.

44. S. Uhlig, and M. Robertsson, "Limitations to and solutions for optical loss in optical backplanes," J. Lightw. Technol., vol. 24, no. 4, pp. 1710-1724, Apr. 2006.

45. X. Dou, X. Wang, H. Huang, X. Lin, D. Ding, D. Z. Pan, and R. T. Chen, "Polymeric waveguides with embedded micro-mirrors formed by Metallic Hard Mold," Opt. Exp., vol. 18, no. 1, pp. 378-385, Jan. 2010.

46. C. Choi, L. Lin, Y. Liu, J. Choi, L. Wang, D. Haas, J. Magera, and R. T. Chen, "Flexible optical waveguide film fabrications and optoelectronic devices integration for fully embedded board-level optical interconnects," J. Lightw. Technol., vol. 22, no. 9, pp. 2168-2176, Sep. 2004.

47. V. J. Erps, N. Hendrickx, C. Debaes, P. V. Daele, and H. Thienpont, "Discrete out-of-plane coupling components for printed circuit board-level optical interconnections," IEEE Photonics Tech. L., vol. 19, no. 21, pp. 1753-1755, Nov. 2007.

48. Y. Cheng, K. Sugioka, K. Midorikawa, M. Masuda, K. Toyoda, M. Kawachi, and K. Shihoyama, "Three-dimensional micro-optical components embedded in photosensitive glass by a femtosecond laser," Opt. Lett., vol. 28, no. 13, pp. 1144-1146, Jul. 2003.

49. "Corning SMF-28 ULL optical fiber," April 9, 2014.

50. M. Haque, K. K. Lee, S. Ho, L. A. Fernandes, and P. R. Herman, "Chemical-assisted femtosecond laser writing of lab-in-fibers," Lab Chip, vol. 14, no. 19, pp. 3817-3829, 2014.

51. L. Yuan, J. Huang, X. Lan, H. Wang, L. Jiang, and H. Xiao, "All-in-fiber optofluidic sensor fabricated by femtosecond laser assisted chemical etching," Opt. Lett., vol. 39, no. 8, pp. 2358-2361, Apr. 2014.

52. Y. Jung, S. Alam, Z. Li, A. Dhar, D. Giles, I. P. Giles, J. K. Sahu, F. Poletti, L. Grüner-Nielsen, and D. J. Richardson, "First demonstration and detailed characterization of a multimode amplifier for space division multiplexed transmission systems," Opt. Exp., vol. 19, no. 26, pp. B952-B957, Dec. 2011.

53. K. S. Abedin, J. M. Fini, T. F. Thierry, V. R. Supradeepa, B. Zhu, M. F. Yan, L. Bansal, E. M. Monberg, and D. J. DiGiovanni, "Multicore erbium doped fiber amplifiers for space division multiplexing systems," J. Lightw. Technol., vol. 32, no. 16, pp. 2800-2808, Aug. 2014.

54. C. Jin, B. Huang, K. Shang, H. Chen, R. Ryf, R. J. Essiambre, N. K. Fontaine et al, "Efficient annular cladding amplifier with six, three-mode cores," In Opt. Comm. (ECOC), 2015 European Conf. on, pp. 1-3. IEEE, Sep. 2015.

55. K. Takeshima, T. Tsuritani, Y. Tsuchida, K. Maeda, K. Watanabe, T. Sasa, K. Imamura et al, "51.1-Tbit/s MCF transmission over 2,520 km using cladding pumped 7-core EDFAs," In Opt. Fiber Comm. Conf., pp. W3G-1, Opt. Soc. of America, Mar. 2015.

56. H. Chen, C. Jin, B. Huang, N. K. Fontaine, R. Ryf, K. Shang, N. Grégoire et al, "Integrated cladding-pumped multi-core, few-mode erbium-doped fibre amplifier for space-division multiplexed communications," arXiv preprint arXiv:1703.06475, Mar. 2017.

57. M. Li, S. Huang, Q. Wang, H. Petek, and K. P. Chen, "Nonlinear lightwave circuits in chalcogenide glasses fabricated by ultrafast laser," Opt. Lett., vol. 39, no. 3, pp. 693-696, Feb. 2014.

58. Hnatovsky, C., R. S. Taylor, E. Simova, V. R. Bhardwaj, D. M. Rayner, and P. B. Corkum, "Polarization-selective etching in femtosecond laser-assisted microfluidic channel fabrication in fused silica," Opt. Lett., vol. 30, no. 14, pp. 1867-1869, Jul. 2005.

59. H. Zhang, S. M. Eaton, and P. R. Herman, "Low-loss Type II waveguide writing in fused silica with single picosecond laser pulses," Opt. Exp., vol. 14, no. 11, pp. 4826-4834, May 2006.

60. D. J. Ripin, and L. Goldberg, "High efficiency side-coupling of light into optical fibres using imbedded v-grooves," Electron. Lett., vol. 31, no. 25, pp. 2204-2205, Dec. 1995.

61. J. P. Koplow, S. W. Moore, and D. A. Kliner, "A new method for side pumping of double-clad fiber sources," IEEE J. Quantum Electron., vol. 39, no. 4, pp. 529-540, Apr. 2003.

62. C. Jauregui, S. Böhme, G. Wenetiadis, J. Limpert, and A. Tünnermann, "Side-pump combiner for all-fiber monolithic fiber lasers and amplifiers," JOSA B, vol. 27, no. 5, pp. 1011-1015, May 2010.

63. D. Kouznetsov, and V. M. Jerome, "Efficiency of pump absorption in double-clad fiber amplifiers. II. Broken circular symmetry," JOSA B, vol. 19, no. 6, pp. 1259-1263, Jun. 2002.

64. H. Chen, N. K. Fontaine, R. Ryf, B. Guan, S. B. Yoo, and T. A. Koonen, "Design constraints of photonic-lantern spatial multiplexer based on laser-inscribed 3-D waveguide technology," J. Lightw. Technol., vol. 33, no. 6, pp. 1147-1154, Mar. 2015.

65. Peleg, Or and Bartal, Guy and Freedman, Barak and Manela, Ofer and Segev, Mordechai and Christodoulides, Demetrios N, "Conical Diffraction and Gap Solitons in Honeycomb Photonic Lattices," Phys. Rev. Lett. 98, 103901, Mar. 2017.

66. Weijia Yang, Costantino Corbari, Peter G. Kazansky, Koichi Sakaguchi, and Isabel C.S. Carvalho, "Low loss photonic components in high index bismuth borate glass by femtosecond laser direct writing, " Opt. Express 16, 16215-16226 (2008)

67. Jiho Noh, Sheng Huang, Daniel Leykam, Yi Dong Chong, Kevin P Chen, Mikael C Rechtsman, "Experimental observation of optical Weyl points and Fermi arc-like surface states," Nature Physics 13, 611–617 (2017).

68. Leykam, D. & Chong, Y. D., "Edge solitons in nonlinear-photonic topological insulators," Phys. Rev. Lett. 117, 143901 (2016).

69. Zhen, B. et al., "Spawning rings of exceptional points out of Dirac cones," Nature 525, 354–358 (2015).

70. Peruzzo, A. et al., "Quantum walks of correlated photons," Science 329, 1500–1503 (2010).

71. Rechtsman, M. C. et al., "Topological protection of photonic path entanglement," Optica 3, 925–930 (2016).

72. Alexander Cerjan, Sheng Huang, Kevin P. Chen, Yidong Chong, Mikael C. Rechtsman, "Experimental realization of a Weyl exceptional ring," arXiv preprint arXiv:1808.09541, Aug. 2018.

73. Oded Zilberberg, Sheng Huang, Jonathan Guglielmon, Mohan Wang, Kevin P Chen, Yaacov E Kraus, Mikael C Rechtsman, "Photonic topological boundary pumping as a probe of 4D quantum Hall physics," Nature 553, 59-62 (2018).

74. H. H. HOPKINS and N. S. KAPANY, "A Flexible Fibrescope, using Static Scanning," Nature 173, 39-41 (1954).

75. D. J. Richardson, J. M. Fini and L. E. Nelson, "Space-division multiplexing in optical fibres," Nature Photonics 7, 354-362 (2013).

76. P. J. Winzer, " Spatial Multiplexing in Fiber Optics: The 10X Scaling of Metro/Core Capacities," Bell Labs Technical Journal 19, 22 (2014).